Study of Fission Reactions Involving Weakly Bound Projectiles

By

Asim Pal

(PHYS01201504013)

Bhabha Atomic Research Centre, Mumbai

A thesis submitted to the

Board of Studies in Physical Sciences

In partial fulfillment of requirements

for the Degree of

DOCTOR OF PHILOSOPHY

of

HOMI BHABHA NATIONAL INSTITUTE

September, 2018

Homi Bhabha National Institute

Recommendations of the Viva Voce Committee

As members of the Viva Voce Committee, we certify that we have read the dissertation prepared by Mr. Asim Pal entitled **"Study of fission reactions involving weakly bound projectiles"** and recommend that it may be accepted as fulfilling the thesis requirement for the award of Degree of Doctor of Philosophy.

Chairman – Prof. B. K. Nayak	BKNayak	**Date:** 23/03/2019
Guide / Convener – Prof. S. Santra	SSantra	**Date:** 23/03/2019
Co-guide - Dr. K. Mahata	KMahata	**Date:** 23/03/2019
Examiner – Prof. B. R. Behera	B. R. Behera	**Date:** 23/03/2019
Member 1- Prof. R. Palit	RPalit	**Date:** 24/03/2019
Member 2- Dr. R. Tripathi	Rahul	**Date:** 23/03/2019

Final approval and acceptance of this thesis is contingent upon the candidate's submission of the final copies of the thesis to HBNI.

I/We hereby certify that I/we have read this thesis prepared under my/our direction and recommend that it may be accepted as fulfilling the thesis requirement.

Date: 23/03/2019

Place: TSH Conference Hall

KMahata
Co-guide

SSantra
Guide

STATEMENT BY AUTHOR

This dissertation has been submitted in partial fulfillment of requirements for an advanced degree at Homi Bhabha National Institute (HBNI) and is deposited in the Library to be made available to borrowers under rules of the HBNI.

Brief quotations from this dissertation are allowable without special permission, provided that accurate acknowledgement of source is made. Requests for permission for extended quotation from or reproduction of this manuscript in whole or in part may be granted by the Competent Authority of HBNI when in his or her judgment the proposed use of the material is in the interests of scholarship. In all other instances, however, permission must be obtained from the author.

Asim Pal

Asim Pal

DECLARATION

I, hereby declare that the investigation presented in the thesis has been carried out by me. The work is original and has not been submitted earlier as a whole or in part for a degree / diploma at this or any other Institution / University.

Asim Pal

Asim Pal

List of Publications arising from the thesis

Journals

1. "Determination of ^{238}Pu(n,f) and ^{236}Np(n,f) cross-sections using Surrogate reactions" ; **A. Pal**, S.Santra, B. K. Nayak, K. Mahata, V. V. Desai, D. Chattopadhyay and R. Tripathi; *Phys. Rev. C* , **2015**, *91* , 054618

2. "Projectile breakup induced fission fragments angular distributions in ^{6}Li+^{232}Th reaction " ; **A. Pal** , S. Santra, D. Chattopadhyay, A. Kundu, K. Ramachandran, R. Tripathi, B. J. Roy, T. N. Nag, Y. Sawant, D. Sarkar, B. K. Nayak, A. Saxena, and S. Kailas; *Phys. Rev. C* , **2017**, *96* , 024603

3. "Mass distributions of fission fragments from nuclei populated by multi-nucleon transfer or incomplete fusion channels in ^{6,7}Li+^{238}U reactions " ; **A. Pal**, S.Santra, D. Chattopadhyay, A. Kundu, A. Jhingan, P. Sugathan, N. Saneesh, Mohit Kumar, N.L.Singh, A. Yadav, C. Yadav, R. Dubey, K. Kapoor, Kavita Rani, Honey Arora, Visakh A.C., Devinder Kaur, B. K. Nayak, A. Saxena, S. Kailas and K. -H. Schmidt ; *Phys. Rev. C* , **2018**, *98 , 031601(Rapid Communications)*

4. "Measurement of incomplete fusion cross-sections in ^{6,7}Li+^{238}U reactions " ; **A. Pal**, S.Santra, D. Chattopadhyay, A. Kundu, A. Jhingan, P. Sugathan, B. K. Nayak, A. Saxena and S. Kailas ; *Phys. Rev. C* , **2019**, *99* , 024620

Conferences

1. "Measurement of ^{236}Np(n,f) cross-sections using surrogate reactions" ; **A. Pal**, S.Santra, B. K. Nayak, K. Mahata, V. V. Desai, D. Chattopadhyay and R. Tripathi; *Proceedings of the Symposium on 75years of Nuclear fission* , **2014**

2. "Determination of ^{236}Np(n,f) and. ^{238}Pu(n,f) cross-sections using surrogate reactions" ; **A. Pal**,S. Santra, B.K. Nayak, K. Mahata, R. Tripathi, A. Parihari, V.V. Desai, D. Chattopadhyay and S. Kailas; *Proceedings of the DAE-BRNS Symp. on Nucl. Phys.* , **2014**, *59* , 342

3. "Mass distributions of fission fragments in coincidence with alpha in ^{6,7}Li+^{238}U reactions" ; **A. Pal**, S.Santra, D. Chattopadhyay, A. Kundu, A. Jhingan, P. Sugathan, N. Saneesh, Mohit Kumar, N.L.Singh, A. Yadav, C. Yadav, R. Dubey, K. Kapoor, Kavita Rani, Honey Arora, Visakh A.C., Devinder Kaur, B. K. Nayak, A. Saxena and S. Kailas; *Proceedings of the DAE-BRNS Symp. on Nucl. Phys.* , **2016**, *61* , 376

4. "Fission fragments mass distributions of the nuclei populated by multi-nucleon transfer channels in ^{6,7}Li+^{238}U reactions" ; **A. Pal**, S.Santra, D. Chattopadhyay, A. Kundu, A. Jhingan, P. Sugathan, N. Saneesh, Mohit Kumar, N.L.Singh, A. Yadav, C. Yadav, R. Dubey, K. Kapoor, Kavita Rani, Honey Arora, Visakh A.C., Devinder Kaur, B. K. Nayak, A. Saxena and S. Kailas; *Proceedings of the DAE-BRNS Symp. on Nucl. Phys.* , **2017**, *62* , 368

5. "Development of a compact MWPC detector" ; **A. Pal**, S.Santra, A. Kundu, D. Chattopadhyay, A. Jhingan, B. K. Nayak and A. Saxena; *Proceedings of the DAE-BRNS Symp. on Nucl. Phys.* , **2017**, *62* , 1140

Asim Pal

Asim Pal

Dedicated to

Our Little Star

Rishan Pal

&

My Wife

Dona Ghosh

&

My Parents

Manju Pal and Santosh Pal

ACKNOWLEDGEMENTS

It gives me immense pleasure to express my sincere gratitude to Dr. S. Santra, for guiding me throughout the tenure of my doctoral programme. He for me is a friend, philosopher and guide. Any time I could share my views and thoughts with him not only on nuclear physics but also on any topic of interest. I am happy to have a small group including Dipayan and Ananya, led by Dr. S. Santra, where helping each other, regular discussions and working hard are enjoyable tasks. I would like to take this opportunity to thank Dipayan and Ananya who helped me to learn many things.

It also gives me immense pleasure to express my gratitude to Dr. B. K. Nayak for teaching me some basics of nuclear physics and encouraging for hard works. Discussions with him always give me better chance to improve my understanding on the subject. Encouragement from Dr. S. Kailas is also gratefully acknowledged. Discussions with Dr. A. Saxena and Dr. V. M. Datar helped me to understand the subject better. Thanks are due to Dr. K. Ramachandran from whom I have learnt a lot on the data acquisition systems during our experimental runs. I would like to thank Dr. K. Mahata and Dr. R. Tripathi from whom I have learnt many things on nuclear fission. I would like to thank Dr. B. J. Roy, Dr. V. Jha, Dr. D. Dutta, Dr. A. Mitra, Dr. Z. Ahmed and Dr. S.R. Jain for teaching me some important courses in BARC Training School.

I am thankful to Prof. R. Palit for his valuable suggestions during the doctoral committee meeting. Special thanks are due to Dr. Akhil Jhingan who helped me to develop MWPC detectors. Discussions (via e-mail) with Prof. K.-H.Schmidt who helped me to understand the basics of GEF code, is gratefully acknowledged. I also thank Dr. K. Nishio and Dr. K. Hirose for providing their published mass distribution data for comparing with our data.

I am thankful to Dr. V.V. Parkar, Dr. P.C.Rout, Dr. S.K. Pandit, Dr. S. Mukhopadhyay, Mr. Debashish Sarkar, Ms. Sukanya De, Mr. Raman Gandhi and other colleagues of Nuclear Physics Division. I would like to take this opportunity to acknowledge the help from all of my collaborators and Staff of Pelletron-Linac facility.

Such a long journey could not be completed without the support of my family. I feel emotional to express my love and respect to my parents. What I am today, is only because of their infinite love, support, help and inspiration. Since my childhood, my mother's dream was to see me achieving the highest academic degree. While writing the thesis I feel emotional as being closed to my mother's dream.

During the hard journey (while studying in B.Sc) I met Dona (wife) who kept on inspiring me through her infinite unconditional love and moral supports. Since then she thought my dream as her own dream and we together came across all the barriers. Her suggestions always help to do better in life.

I acknowledge the love from my elder sisters (Surekha, Monika), niece (Sumana, Chutu) and nephew (Subham). I thank parents-in-law for their love and good wishes. I acknowledge the help from Goutam Da throughout my carrier.

Love and inspirations from my school friends, friends at Jadavpur University, IIT Kharagpur and BARC Training School are highly acknowledged. I also thank all the teachers of my life. I would like to take this opportunity to thank Mr. Tarun Dutta, Mr. Manoranjan Patra (Former MLA, Taldangra Block, West Bengal) and members of Bidhannagar Chatrabas Trust for their financial help during my study in B.Sc and M.Sc. Finally I would like to give a big thank to my critics who always indirectly help me to do the best in life.

Asim Pal

Asim Pal

SYNOPSIS

Nuclear fission is a phenomenon where a heavy nucleus splits into two lighter nuclei [1,2]. One can understand the process in the framework of simplified liquid drop model [3] where a charged liquid drop undergoes shape changes resulting in a competition between surface energy and Coulomb energy. With increasing deformation, Coulomb energy decreases and surface energy increases. The resultant change in potential energy gives rise to a barrier (fission barrier), which prevents a nucleus at ground state to undergo fission. However, various experimental observations on fission isomers suggest that the shape of the barrier is double-humped type, which cannot be understood from this simplified model. The shell corrected and pairing energy has been found to be responsible for the double-hump shaped fission barrier. Although the fission process has been discovered about 80 years ago, this simple splitting of a heavy nucleus has been continuing to draw lots of interest and attention among researchers worldwide. In early days, the process was studied using the fission induced by light projectiles like neutron, proton, gamma rays as well as the spontaneous fission of heavy nuclei. With the advent of heavy ion accelerators it has been possible to carry out extensive research on the fission process after formation of a compound nucleus at high excitation energy and high angular momentum in the heavy and super heavy mass region. It is proposed to produce those super heavy nuclei using neutron rich radioactive ion beams (RIB). The reaction mechanism involving RIBs, having very small particle separation energy, can however be simulated by studying the reactions involving weakly bound stable projectiles.

In case of weakly bound stable projectiles, the study of fission process following compound nucleus formation becomes complicated as it gets mixed up with various breakup or transfer induced fission channels which are caused by partial capture of the projectile by the target. Study of breakup or transfer induced fission reactions involving weakly bound stable projectiles like ^{6,7}Li and ^{9}Be bears a lot of interest due to the presence of projectile breakup channels that might affect the fission dynamics in general and fission observables in particular such as (i) fission fragment angular distribution (FFAD), (ii) fission fragment mass distributions (FFMD) and (iii) fission fragment folding angle distributions (FFFAD). The weakly bound projectiles, having low breakup threshold, can accompany breakup fragment induced fission by a significant amount. Contribution of transfer/breakup induced fission has been cited as one of the possible reasons for the increase in angular anisotropy of total fission [4,5]. Interestingly, the enhancement in angular anisotropy has also been observed in reactions with tightly bound projectiles where transfer induced fission has been conjectured as a possible reason [6]. Effect of breakup or transfer induced fission has also been observed in FF folding angle distribution. A kink like structure very closed to the main peak in FFFAD in ^{6,7}Li+^{238}U reactions is observed, due to which the width of the FFFAD increases at below barrier energies, in contrast to the reactions involving tightly bound projectiles where a linear energy dependence is observed [7]. In another interesting observation, the peak to valley (P:V) ratios of FFMD for inclusive fission in ^{6,7}Li+^{238}U and ^{6}Li+^{232}Th reactions are found to be more compared to the ones expected for complete fusion (CF)-fission [7,8]. This enhancement in P:V ratio is again assumed to be due to the presence of ICF-fission. One advantage of the ICF or multi-nucleon transfer reaction followed by fission is that it can be used as a tool for populating a nucleus which cannot be accessed by a reaction involving stable target and projectile combination [9-11]. Therefore, it will be of interest to study these nuclei populated by multi nucleon transfer reactions, involving weakly bound projectiles where breakup/transfer induced fission probabilities are large. Importantly, such reaction may act as a surrogate reaction of some desired reaction for which the cross section is unknown. For example, fast neutron induced fission cross-sections are extremely important for the Generation-IV reactor. But, due to non-availability of target or projectile, it has been difficult to measure the cross section directly. However, it may be possible to populate the same compound nucleus by a transfer or ICF reaction (surrogate reaction) using a stable target-projectile combination and the desired cross-sections can be determined by employing surrogate ratio technique [11,12]. Motivated by all the physics issues discussed above, we carried out several experiments to measure light charged particles in coincidence with fission fragments in reactions involving weakly bound stable projectiles and actinide targets, namely, (1) FFAD measurement in ^{6}Li+^{232}Th reaction, (2) FFFAD and FFMD measurements on ^{6,7}Li+^{238}U systems, (3) FFMD measurements on ^{10,11}B+^{238}U systems and (4) determination of ^{238}Pu(n,f) and ^{236}Np(n,f) cross sections by studying fission reactions on ^{6}Li+^{232}Th,^{235}U systems. The fission fragments have been detected using either silicon strip detectors or surface barrier detectors or gas detectors, whereas light charged particles were detected using silicon strip detectors or surface barrier detectors or CsI(Tl) scintillation detector. Two multi-wire proportional counter (MWPC) gas detectors developed in-house have also been used for some of the fission measurements. The results obtained from the above experiments have been described as follows.

1. FFAD measurements in ^{6}Li+^{232}Th reaction: The measured angular anisotropy for inclusive FFAD agrees well with the value available in the literature [13] but they are slightly more compared to the statistical saddle point model (SSPM) predictions. To investigate the reason for this deviation, angular anisotropy for breakup or transfer induced fission has been obtained exclusively in the rest frame of the recoiling nuclei. The angular anisotropy for the α-gated fission has been found to be less (more) than the ones for inclusive fission for near and above barrier energy (below barrier). Similarly, in the rest frame of recoiling nuclei angular anisotropy for d and p gated fissions are stronger than those for the inclusive fission in center-of-mass frame. To estimate

the overall anisotropy, the angular distributions of transfer induced fission corresponding to each recoil direction have been integrated with proper weight factor P(θ_{PLF}), proportional to the differential cross sections of the outgoing PLF. Finally, the estimated anisotropy of transfer/breakup-induced fission in coincidence with PLF comes out to be less than or equal to the ones observed for the inclusive fission. For d- and p-gated fission, the angular anisotropy values are found to be slightly higher but within the experimental errors of inclusive fission. So it can be concluded that the observed enhancement in the anisotropy for total fission compared to the SSPM predictions at near-barrier energies is not due to the contribution from breakup- or transfer-induced fissions [14]. Hence, the enhancement of angular anisotropy has been described with the help of ECD K-state model.

2. FFFAD and FFMD measurement in ^{6,7}Li+^{238}U reactions: FF folding angle distributions for total fission in laboratory frame for both the reactions show shoulder structure near main peak [7]. The present measurements confirm that the FFFADs in coincidence with different PLFs indeed peak at those angles where kink like structures in inclusive FFFAD were observed. The α-gated fission, being the most dominant transfer or ICF channel, is mainly responsible for the presence of the kinks in inclusive FFFAD at sub-barrier energies. Now, mass distributions for inclusive fission have been obtained for all the projectile energies. As expected [7], the P:V ratio for CF-fission, have been found to be less than the P:V ratio for inclusive fission. The contamination of ICF-fission with CF-fission is believed to be the main reason for creating the above discrepancy. So, to find the contributions from the non-compound fission channels, the mass distributions for individual ICF- or transfer-fission channels have been derived using 3 body kinematics. Interestingly, it has been observed that P:V ratios of FF mass distributions for all the transfer- or ICF-fission channels are found to be higher than the ones for total fission for a particular beam energy. Obviously, any admixture

of ICF fission with CF fission will increase the P:V ratio of the total fission at the excitation energy corresponding to CF fission, thus explaining the difference in the P:V ratios between CF fission and total fission. The measured P:V ratio for each of these transfer induced fissions at proper excitation energy is found to follow the trend of the P:V ratios of mass distributions of fission fragments emitted from similar compound nuclei of nearby masses. It may be emphasized that mass distributions of several nuclei, namely ^{243,244}Pu and ^{241}Np, which cannot be populated by stable target and projectile, have been obtained in this study. These nuclei have been populated by the capture of 5He, 6He and triton respectively by ^{238}U target. For all the fissioning nuclei (^{240,241}Np, ^{241,242,243,244}Pu), the theoretical calculations with modified shell correction parameter for symmetric fission, agree with the experimental data reasonably well. It implies that the value of the shell correction for symmetric fragments plays an important role in FF mass distribution [15]. Here it may be pointed out that, shell correction parameter for symmetric channel being weak compared to the strong shell correction for asymmetric fission, is not so well known. Hence it should be obtained from the measured mass distribution data. In addition, the cross-sections for individual ICF or transfer induced fission channels in ^{6,7}Li+^{238}U reactions have been measured. Interestingly, the fissioning nuclei being in the actinide regions, the fissioning probability after capturing any fragment, is $\sim$ 80-95%. Hence total incomplete fusion cross-sections can be found out from the angle integrated and efficiency corrected total ICF or transfer induced fission cross-sections. Further, recent studies on fusion with weakly bound stable projectiles show that the complete fusion cross-sections are suppressed at energies above the Coulomb barrier and the cross sections for incomplete fusion are found to be similar to the missing complete fusion cross sections [16]. So, measurement of total ICF cross-sections is very important. The ICF cross-sections in the present study have been obtained by calculating (a) the coincidence efficiency between two MWPC detectors using a Monte Carlo simulation, (b) the geometrical efficiency of the MWPC detectors and (c) excitation energy dependent fission probabilities. The relative contribution of ICF fission at the lowest measured energy has been found to be $\sim 70\%$ and it gradually decreases with increasing energy. The ratio has been compared with the ones available in literature on different systems. Interestingly, the ratio at the highest measured energy is nearly same as complete fusion suppression factors for both the projectiles. 3. FFMD measurement in ^{10,11}B+^{238}U reactions: FF mass distributions have also been measured for ^{10,11}B+^{238}U systems using pulsed beam at energies near Coulomb barrier. The projectiles ^{10,11}B can also be considered as weakly bound [17,18] but with higher threshold of breakup (^{10,11}B $\rightarrow$ ^{6,7}Li) compared to ^{6,7}Li ($\rightarrow$ ^{2,3}H). By measuring the velocities of the fission fragments, mass distributions have been derived for both the reactions and compared with the GEF calculations. At the highest measured energy, mass distribution for transfer or breakup induced fission have also been obtained but with very poor statistics.

4. Measurement of ^{238}Pu(n,f) and ^{236}Np(n,f) cross-sections using surrogate reactions: In the surrogate ratio method, cross sections for the desired reaction is determined with respect to a reference reaction whose cross section is known. For example, to determine the cross section of ^{238}Pu(n,f) reaction, the cross section of ^{235}U(n,f) reaction has been used as a reference. Here the fissioning nuclei ^{239}Pu and ^{236}U have been populated using transfer or ICF reactions ^{235}U(^{6}Li,d) and ^{232}Th(^{6}Li,d) respectively at same excitation energy. Now, by measuring deuteron in coincidence with fission and deuteron singles, the ratios of fission decay probabilities for both these nuclei have been obtained at the same excitation energy of the fissioning nuclei. This method also requires the knowledge of the ratio of compound nucleus formation cross sections in the desired channel, which has been obtained using the optical model code EMPIRE-3.1 [19]. Then multiplying the factors of "the known reference reaction cross-section", "ratio of

fission decay probabilities" and "ratio of formation cross-section of compound nuclei in the desired reaction channel" one can determine the reaction cross-sections of interest, corresponding to some equivalent neutron energy. Following the above procedure, the cross sections for the ^{238}Pu(n,f) reaction have been determined in the equivalent neutron energy range of 13.0-22.0 MeV. Similarly, the cross-sections for ^{236}Np(n,f) have been determined with the help of the reference reaction ^{238}Pu(n,f). Here the fissioning nuclei ^{237}Np and ^{239}Pu have been populated using transfer or ICF reaction ^{235}U(^{6}Li,d) and ^{235}U(^{6}Li,α) respectively at same excitation energies in the range of 16.6-28.6 MeV. The cross sections for ^{236}Np(n,f) reactions have been determined for equivalent neutron energy in the range of 9.9-22.0 MeV. The above cross sections have been compared with the evaluations from ENDF/B-VII.1 and EMPIRE calculations [20].

5. Development of MWPC detectors: Two large area position sensitive compact multi-wire proportional counters have been developed and used for the detection of fission fragments in a few measurements of present thesis work. The core of the detector consists of five frames each with an active area 12.5 $\times$ 7.5 cm^2. The arranged wire frames starting from the entrance of the detector are: a cathode, an X-frame, an anode, a Y-frame and a second cathode (shorted with the first cathode). The design is similar to the one developed by Breskin [21]. All wire frames are made from gold plated tungsten wire with 20 μm diameter, stretched on a 1.6 mm thick printed circuit board. All the frames are stacked one after another. The X frame is made from 100 wires whereas the remaining frames have 60 wires each. The separation of two consecutive wires is 1.27 mm. Using commercially available rhombus delay line integrated chips (model TZB12-5) position information from X and Y frames are extracted. The electrode assembly is mounted inside a rectangular metal housing milled out from a solid aluminum block of dimension 21.2 $\times$ 15.6 cm^2. At the entrance of the detector 0.5 μm thick mylar foil has been used to isolate it from the vacuum chamber. The foil is supported by nylon wires.

Voltages of +360 V and -180 V are supplied to anode and cathode respectively and the detector is operated with flowing isobutane gas at 1-4 torr pressure. Typical pulse height of 1-10 V was observed from cathode signal which also shows clear distinction between light and heavy charged particles. Pulse height for anode signal and position signals are $\sim$ 500-1500 mV and 100-300 mV respectively. The resolution of x and y positions have been found to be 1.5 mm and 1.7 mm respectively. A time dispersion of 1.7 ns in the detector plus electronics circuit has been determined. The detectors have been used for in-beam fission experiments on ^{10,11}B,^{19}F + ^{238}U reactions. A good mass resolution of $\sim$ 5-6 u has been achieved.

To conclude, the present thesis contains exclusive coincidence measurements between light charged particles and fission fragments in the reactions involving weakly bound projectiles and actinide targets, in order to find out the effect of transfer/ICF fission channels on inclusive fission. The effect on inclusive fission fragment angular anisotropy is found to be insignificant. But, the effect is quite significant in case of fission fragment folding angle distributions and mass distributions and the unambiguous behaviors are quantitatively explained. By comparing with the theoretical mass distributions, the values of shell correction parameters for symmetric channel for several fissioning nuclei have been determined. Few neutron induced fission cross-sections have been determined employing surrogate ratio method. The present thesis also contains a developmental work on multi-wire proportional counters for the detection of fission fragments. The thesis has been organized as follows. In Chapter 1, a brief introduction with the present status of the field and general motivation is presented. General experimental techniques used for the detection of fission fragments and projectile like fragments are presented in Chapter 2. The developmental work on MWPC detectors is described in Chapter 3. The results on fission fragment angular distribution for inclusive as well as transfer or ICF-fission are presented in Chapter 4. The results from the measurement of mass distributions for inclusive and ICF/transfer fission for 6,7Li+238U systems are described in Chapter 5. Measurements of mass distributions on 10,11B+238U systems are presented in Chapter 6. Determination of neutron induced fission cross sections using surrogate reactions is described in Chapter 7. Finally, the summary of the thesis and future scope of the work are highlighted in Chapter 8.

References:

[1] O. Hahn, F. Strassmann, Naturwiss. 27, 11 (1939)

[2] L. Meitner, O.R. Frisch, Nature 143, 239 (1939)

[3] N. Bohr, J.R. Wheeler, Phys. Rev. 56, 426 (1939)

[4] A. Parihari et al., Phys. Rev. C 90, 014603 (2014)

[5] S. Appannababu et al., Phys. Rev. C 83, 067601 (2011)

[6] H. Zhang et al., Phys. Lett. B 218, 133 (1989)

[7] S. Santra et al., Phys. Rev. C 90, 064620 (2014)

[8] I.M. Itkis et al., Phys. Lett. B 640, 23 (2006)

[9] R.Leguillon et al., Phys. Lett. B 761, 125 (2016)

[10] K. Hirose et al., Phys. Rev. Lett. 119, 222501 (2017)

[11] J. E. Escher et al., Rev. Mod. Phys. 84, 353 (2012)

[12] B. K. Nayak et al., Phys. Rev. C 78, 061602(R) (2008)

[13] H. Freiesleben et al., Phys. Rev.C 12, 42 (1975)

[14] A. Pal et al., Phys. Rev. C 96, 024603 (2017)

[15] A. Pal et al., Phys. Rev. C 98, 031601 (R) (2018)

[16] M. Dasgupta et al., Phys. Rev. C 70, 024606 (2004)

[17] A. Mukherjee et al., Phys. Lett. B 636, 91 (2006)

[18] V. V. Parkar et al., Phys. Rev. C 82, 054601 (2010)

[19] M. Herman et al. Nucl. Data Sheets 108, 2655 (2007)

[20] A. Pal et al., Phys. Rev. C 91, 054618 (2015)

[21] Breskin et al., Nucl. Instrum. Methods Phys. Res. A 221, 363 (1984)

Contents

List of Figures

List of Tables

Chapter 1

Introduction

Nuclear fission is a type of nuclear reaction in which a large nucleus splits into two lighter nuclei [1, 2]. It is a phenomenon where a nucleus, before splitting, turns into a di-nuclear shape from a mononuclear shape through drastic rearrangement of nucleons among itself. One can understand the process in the framework of simplified liquid drop model [3] where a charged liquid drop undergoes shape changes resulting in a competition between surface energy and Coulomb energy. With increasing deformation, Coulomb energy decreases and surface energy increases. The resultant change in potential energy gives rise to a barrier (fission barrier), which prevents a nucleus at ground state to undergo fission. However, various experimental observations on fission isomers suggest that the shape of the barrier is double-humped type, which cannot be understood from this simplified model. The shell corrected and pairing energy has been found to be responsible for the double-hump shaped fission barrier.

Although the fission process has been discovered about 80 years ago, this simple splitting of a heavy nucleus has been continuing to draw lots of interest and attention among researchers worldwide. In early days, the process was studied using the fission induced by light projectiles like neutron, proton, gamma rays as well as the spontaneous fission of heavy nuclei. With the advent of heavy ion accelerators it has been possible to carry out extensive research on the fission process after formation of a compound nucleus at high excitation energy and high angular momentum in the heavy and super heavy mass region. The fission mechanism of a nucleus in spontaneous or heavy ion induced fission, is described using liquid drop model as discussed below.

1.1 Fission mechanism

The most successful model to describe the process of nuclear fission is liquid drop model. The same model has a great story of success in describing the nuclear mass and the relevant formula is known as Bethe-Weizsacker semi-empirical mass equation. There are five terms contributing to it: volume term, surface term, Coulomb term, symmetry term and pairing term. Among these volume term, symmetry term and pairing term are independent of distortion of nuclei. But surface term and Coulomb term play a competitive role while a nucleus undergoing shape changes.

For a small axially symmetric distortions, the radius parameter can be written as

$$R(\theta) = R_0[1 + \alpha_2 P_2(\cos\theta)] \tag{1.1}$$

where θ is the angle of the radius vector, the coefficient α_2 is a parameter describing the amount of quadrupole distortion, and R_0 is the radius of the undistorted sphere. The surface (E_s) and Coulomb energies (E_c) for small distortions are given by (ignoring the higher order terms)

$$E_s = E_{s0}[1 + \frac{2}{5}\alpha_2^2] \tag{1.2}$$

$$E_c = E_{c0}[1 - \frac{1}{5}\alpha_2^2] \tag{1.3}$$

where E_{s0} and E_{c0} are the surface and Coulomb energies of undistorted spheres respectively. The decrease in Coulomb energy ($\Delta E_c = -\frac{1}{5}\alpha_2^2$) must be smaller than the increase in surface energy ($\Delta E_s = \frac{2}{5}\alpha_2^2$) to be stable against the small distortions. The drop will become critically unstable when $\Delta E_s = \Delta E_c$ or when $E_{c0}/2E_{s0}$ =1 or when

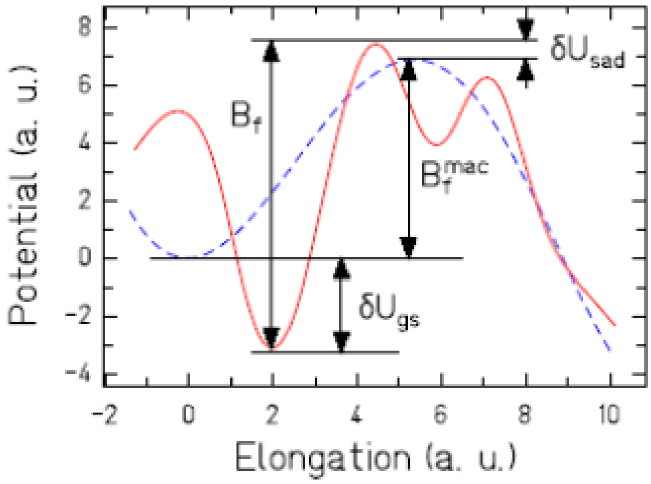

Figure 1.1: The potential obtained from liquid drop model without (blue dashed line) and with (red line) shell corrections as descibed in Ref. [4].

x=1 (x= $E_{c0}/2E_{s0}$ is called fissility parameter).

In order to accurately describe distortion, we must write the radius parameter as

$$R(\theta) = R_0[1 + \sum \alpha_n P_n(\cos\theta)] \tag{1.4}$$

Therefore, if we include all the higher order deformation terms, we get a potential energy curve as a function of deformation, giving rise to a barrier (known as fission barrier) as shown by blue line in Fig. 1.1. So the nucleus has to come across the barrier before dividing into two fragments.

But, liquid drop model fails to explain the asymmetric mass division of a nucleus. It also remains unsuccessful in explaining the nature of double hump fission barrier observed for few nuclei. However, the liquid drop model can reproduce the double humped fission barrier if shell correction (δU) and pairing term (δP) are added to the energy obtained from liquid drop model following Strutinsky's shell correction method [5, 6].

Following the above method the total energy can be written as

$$E = E_{LDM} + \sum (\delta U + \delta P) \tag{1.5}$$

Here, all of the quantities are functions of the deformation. The shell correction term is obtained by taking the difference of total energy of nucleons obtained from shell model and energy of uniformly distributed nucleons.

$$\delta U = U - \bar{U} \tag{1.6}$$

where $U = \sum 2n_\nu \epsilon_\nu$ and $\bar{U} = 2\int_{-\infty}^{\lambda} Eg(E)dE$ (ϵ_ν= energy of nucleon levels, n_ν= occupation number, $g(E)$= uniform distribution of nucleon states and λ = the corresponding chemical potential). In the same way shell correction term for paining energy is obtained. The details of it has been given in Ref. [5].

After incorporating the shell correction and pairing terms, the liquid drop model now leads to double humped behavior of the deformation potential as shown by red line in Fig. 1.1. The first minimum of the deformation potential occurs at known ground state deformation of the nucleus. There is a evidence for the presence of such a second minimum in several nuclei from the known existence of spontaneously fissioning isomers. The second minimum begins to disappear for Cf and heavier nuclei, partly because the liquid drop energy falls off very steeply at a smaller deformation.

1.1.1 Penetration of the barrier

For a single parabolic barrier, the well known Hill-Wheeler transmission co-efficient can be written as

$$T_{HW} = \frac{1}{1 + exp[(2\pi/\hbar\omega)(V - E)]} \tag{1.7}$$

where V and $\hbar\omega$ are the height and curvature of the parabolic barrier respectively. Now, for a double humped barrier the transmission fission calculated in WKB approximation reads

$$T_{double} = \frac{T_1 T_2}{1 + 2A^{1/2}\cos(2\nu_2) + A} \tag{1.8}$$

where $A = (1 - T_1)(1 - T_2)$ and ν_2 represents the momentum integral for the well as given below

$$\nu_2 = \int [2\mu(E - V_2(\beta))/\hbar^2]^{1/2} d\beta \tag{1.9}$$

In case of a double humped barrier, the incoming flux can be transmitted directly through the barrier (coefficient=$T_d(1,2)$) or can be absorbed in the isomeric well. The fraction absorbed in the isomeric well can be either re-emitted in the fission channel (coefficient=T_2) or return back to the primary state (coefficient=R) or undergo γ transition to the isomeric state (coefficient=T_a). Hence in the case of a double humped barrier, the general expression of the fission co-efficient can be written as

$$T_f = T_d(1,2) + RT_aT_2 \tag{1.10}$$

Using the above formulas, generally the fission cross-sections for a reaction are calculated.

So far, we have discussed the mechanism of the fission process of a nucleus undergoing fission from ground state in a simplified way. However, the mechanism of heavy ion induced fission is much more complex as the the process involves formation of a intermediate state (compound nucleus). The detailed mechanism has been discussed below.

1.2 Fission mechanism in heavy ion fusion-fission reaction

In heavy ion induced fusion-fission reaction, understanding of interaction potential between target and projectile is very much important. One dimensional interaction potential between the two heavy ions have been very successful, where the degree of freedom is the separation R between two nuclei. In a static approach the interaction

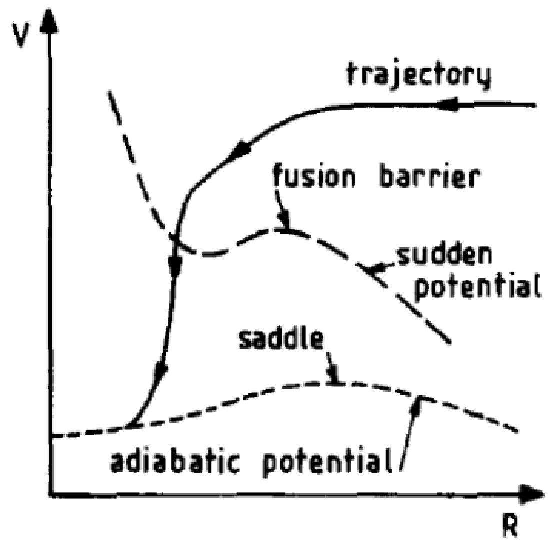

Figure 1.2: The sudden potential and the adiabatic potential have been shown by dashed black lines. The trajectory starting from the entrance channel has been shown by solid black line as described in Ref. [7].

potential between the two ions can be calculated with two extreme assumptions:

(1)The **sudden approximation** assumes that the relative motion of the nuclei is so fast that densities of the two participating nuclei remain constant. When dynamical calculations is performed including shape vibrations, it is observed that, until the two ions reach the closest distance of approach, they just become little oblate. As shown by upper dashed curve in Fig. 1.2, while fusion taking place, the interacting potential is approximated by sudden potential. However, after the minimum distance of approach is reached, strong deformation can come into play and then the dynamics is better described by adiabatic potential.

(2) The **adiabatic approximation** where, at each distance, the potential energy is calculated by minimization with respect to other collective degrees of freedom. It assumes that the relative motion of the two ions is slow enough for the other degrees of freedom to relax to equilibrium. This difficult calculation is particularly relevant in the case of fission and it is possible to calculate the saddle configuration of the fissioning

system as shown by bottom dashed curve in Fig. 1.2.

Therefore, in a heavy ion induced fusion fission reaction, the heavy projectile needs to cross a barrier (fusion barrier) as obtained from sudden approximation and subsequently form a compound system which relaxes in different degrees of freedom (mass,K (Projection of J along nuclear symmetry axis), energy, angular momentum etc.). Now the compound nucleus formed at certain excitation energy starts deforming and develops a potential profile as described by adiabatic approximation before decaying into fission channel. This mechanism is known as compound fission or complete fusion-fission.

Now, if the combined system formed by capture of the projectile by the target, does not equilibrate in all degrees of freedom, it leads to different kinds of fission mechanism as described below.

1.2.1 Non-compound fission mechanism

Other than the complete fusion-fission channels, typically four types of fission processes are observed in heavy ion induced fission.

(a) Fast fission: It is expected to take place for the composite system when the angular-momentum-dependent fission barrier drops below the nuclear temperature and becomes extremely small. Therefore the system can not be kept in the interaction region and escapes by fissioning in two fragments. The reaction time for such process is intermediate to those observed in deep inelastic reactions and compound nucleus formation.

(b) Quasi-fission: When the compound nucleus has a fission barrier but the saddle configuration is too compact to keep the system trapped, the system breaks into two fragments. This kind of mechanism where the two interacting ions re-separate without forming the compound nucleus is expected to take place more for systems involving moderately heavier projectiles (A > 20) but with fission barrier not as small as it was in the case of fast fission. Quasi-fission is expected to occur if the product of atomic numbers of target and projectile exceeds 1600 [8], although there are few exceptions to it [9]. A detailed mechanism of quasifission and fast fission processes have been described in Ref. [7].

(c) Pre-equilibrium fission: In this mode of fission, the fissioning nucleus equilibrates in all degrees of freedom except K-degrees of freedom [10]. The PEQ events occur in a time scale comparable to the characteristic relaxation time of the K-degree of freedom when the fission-barrier height becomes comparable to the temperature of the composite system. In the case of compound nuclear fission the final K distribution at the transition state (saddle point) is broader, whereas in the case of PEQ fission, the final K distribution is expected to be very narrow, almost corresponding to the initial value of the composite system. In this sense the PEQ fission may have memory of the entrance channel. It is expected to occur if the entrance channel mass-asymmetry ($\alpha = \frac{m_{target} - m_{projectile}}{m_{target} + m_{projectile}}$) is higher than the Businaro-Gallone parameter[11].

(d)Breakup or transfer induced fission: There is another type of non-compound fission process known as breakup or transfer induced fission, which is caused by partial capture of the projectile by the target forming a composite system that undergoes fission. It is expected to be dominant if the projectile is loosely bound.

The above non-compound fission processes can severely effect the fission observables [12]. Sometimes it might be difficult to disentangle the effect due to different processes. But in a reaction involving light weakly bound projectiles (^{6,7}Li) and actinide targets, at energies near the Coulomb barrier, the chances of occurring of the first three non-compound fission processes are less, but the fourth process can effect the fission dynamics in a significant way.

1.3 Fission studies with weakly bound projectiles

With the advent of heavy ion accelerators extensive research on the fission process after formation of a compound nucleus have been carried out at high excitation energy and high angular momentum in the heavy and super heavy mass region. In the mean time, it is proposed to produce those super heavy nuclei using neutron rich radioactive ion beams (RIB). The reaction mechanism involving RIBs, having very small particle separation energy, can however be simulated by studying the reactions involving weakly bound stable projectiles.

In case of weakly bound stable projectiles, the study of fission process following compound nucleus formation becomes complicated as it gets mixed up with various breakup or transfer induced fission channels which are caused by partial capture of the projectile by the target. Study of breakup or transfer induced fission reactions involving weakly bound stable projectiles like ^{6,7}Li and ^{9}Be bears a lot of interest due to the presence of projectile breakup channels that might affect the fission dynamics in general and fission observables in particular such as (i) fission fragment angular distribution (FFAD), (ii) fission fragment mass distributions (FFMD) and (iii) fission fragment folding angle distributions (FFFAD). The weakly bound projectiles, having low breakup threshold, can accompany breakup fragment induced fission by a significant amount. In literature, there are several studies involving weakly bound projectiles which shows the effect on different fission observables mentioned above. There are also few interesting features associated with the weakly bound projectiles as discussed below.

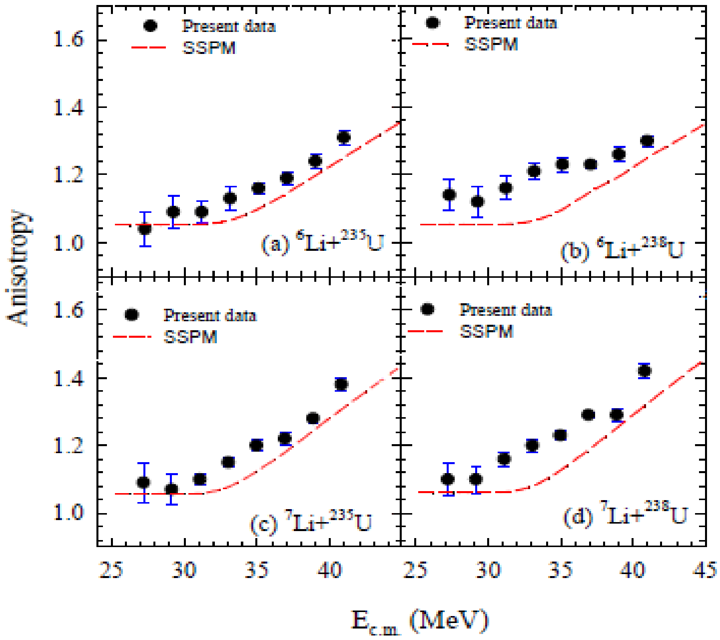

Figure 1.3: Comparison of FF angular anisotropy data (filled circles) with statistical model calculations (dashed lines) in ^{6,7}Li+^{235,238}U reactions [13].

1.3.1 Possible effect on FFAD

FF angular anisotropy has been observed to increase compared to the ones obtained from statistical saddle point model (SSPM) prediction in reactions involving weakly bound projectiles [13, 14] as shown in Fig. 1.3 for ^{6,7}Li+^{235,238}U reactions. The two possible reasons:(i) breakup or transfer induced fission and (ii) entrance channel dependent pre equilibrium fission have been cited for causing the above discrepancy. In a breakup or transfer induced fission reaction, the composite system is formed with temperature and angular momentum different from the compound nucleus formed in complete fusion. On the other hand, because of partial equilibration in K degrees of freedom, the width of the K distribution gets reduced, causing the anomalous behavior in FF angular anisotropy. The disentanglement of the above two reasons is still due in the literature.

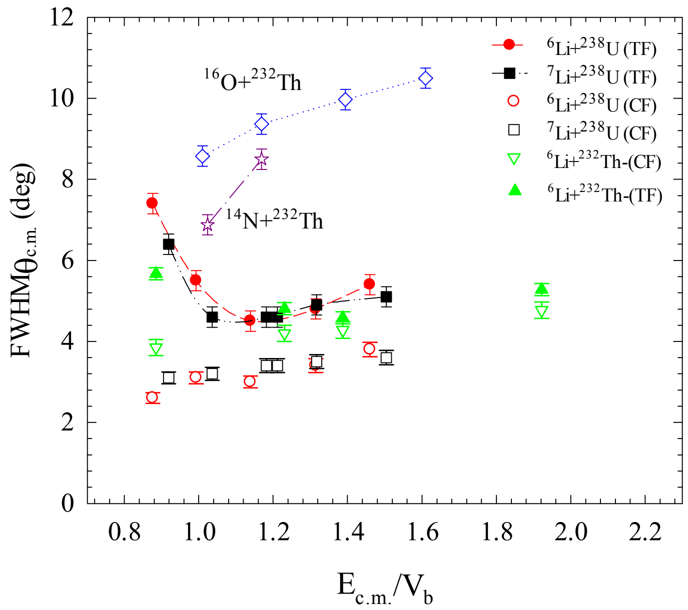

Figure 1.4: Width of the folding angle distributions as a function of E_{cm}/V_b for different systems [15, 16].

1.3.2 Possible effect on FFFAD

Effect of breakup or transfer induced fission has also been observed in inclusive FF folding angle distribution. A kink like structure very closed to the main peak in inclusive FFFAD in ^{6,7}Li+^{238}U and ^{6}Li+^{232}Th reactions is observed, due to which the width of the FFFAD increases at below barrier energies [filled symbols in Fig. 1.4], in contrast to the complete fusion reaction with the same projectile or the reactions involving tightly bound projectiles [hollow symbols in Fig. 1.4] where a linear energy dependence is observed [15, 16]. Linear momentum transfer to the target nuclei in the process of ICF-fission is believed to be the primary reason. For beam energies above the Coulomb barrier with grazing angle $\theta_{gr} < 90°$, ICF is accompanied by partial linear momentum transfer to the target nuclei leading to a larger folding angle of the fission fragments, whereas, at below barrier energies, $\theta_{gr} > 90°$, the FF folding angle decreases due to higher linear momentum transfer compared to CF fission.

1.3.3 Possible effect on FFMD

In another interesting observation, the peak to valley (P:V) ratios of FFMD for inclusive fission in ^{6,7}Li+^{238}U and ^{6}Li+^{232}Th reactions are found to be more compared to the ones expected for complete fusion (CF)-fission [15, 16]. As shown in Fig. 1.5, in ^{6}Li+^{238}U reaction, P:V ratio for inclusive fission (filled square) is more than the ones for CF-fission (hollow square) which is more closer to the theoretical prediction (dotted line). The contamination of transfer induced or ICF fission channels in the complete fusion (CF) fission have been again conjectured as a possible reason for the above enhancement. For the fission events following transfer or incomplete fusion (ICF), partial energy gets transferred to the composite nuclei leading to smaller excitation energy which in turn introduces larger P:V ratio in the mass distributions. Therefore, the presence of projectile breakup and/or particle transfer is believed to be responsible for populating the composite nuclei with different temperature and recoil momentum compared to that of a compound nucleus (CN), resulting in such unusual features in fission observables.

1.3.4 Complete-fusion suppression

Suppression of complete fusion cross-sections is an interesting observation [17, 18, 19, 20, 21, 22, 23, 24] in reactions involving weakly bound projectiles. As shown in Fig. 1.6, the normalized complete fusion cross-section in ^{6}Li+^{144}Sm reaction (hollow circle) is suppressed as compared to coupled channel calculation (red dotted line) and/or the normalized complete-fusion cross-sections for forming the similar compound nucleus in reactions involving tightly bound projectiles ^{12}C and ^{20}Ne [25, 26]. One can see that the measured cross-sections is 0.68 times the calculated cross-sections (solid black line). Here incomplete fusion caused by the partial capture of the weakly bound pro-

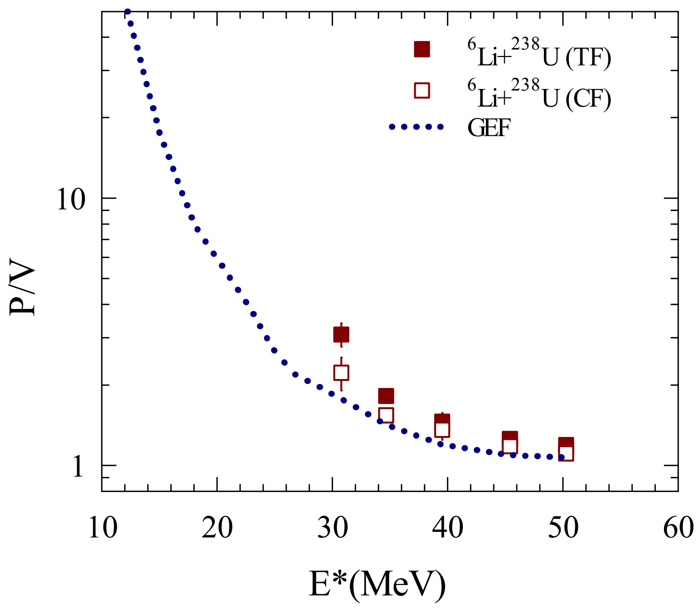

Figure 1.5: P:V ratio of mass distributions for inclusive (filled square) and CF-fission (hollow square) in ^{6}Li+^{238}U reaction [16]. Dotted line represents the theoritical prediction of P:V ratio for CF-fission in the same reaction.

jectile is believed to be the primary reason for the discrepancy between observed and theoretical cross-sections. In literature, there are some cases where the cross sections for incomplete fusion are found to be similar to the missing complete fusion cross sections [27, 28]. Therefore incomplete fusion is mainly responsible for the suppression of complete fusion cross-sections in reactions involving weakly bound projectiles. Now a days particle-gamma coincidence technique or characteristic particle decay technique are widely used for the measurement of ICF cross-sections. Importantly fission followed by multinucleon transfer or incomplete fusion can also be used as a powerful tool to measure ICF cross-sections [29].

1.3.5 Surrogate reaction

One advantage of the ICF or multi-nucleon transfer reaction followed by fission is that it can be used as a tool for populating a nucleus which cannot be accessed by a reaction involving stable target and projectile combination [30, 31, 32]. Therefore, it will be of

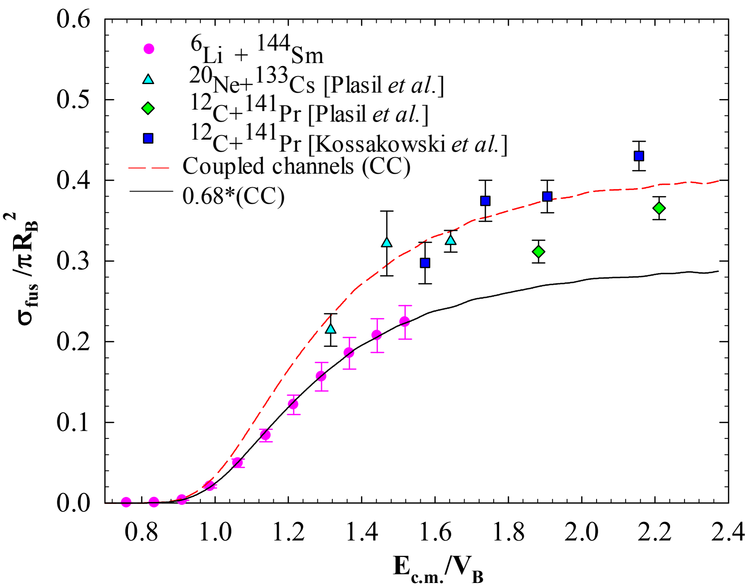

Figure 1.6: Comparison of complete fusion cross-sections for ^{6}Li+^{144}Sm (filled circle)[17] and those for tightly bound projectiles [25, 26]. Total and normalized complete fusion cross-sections obtained from coupled channel calculation for ^{6}Li+^{144}Sm system are shown by red dotted and black solid lines respectively.

interest to study these nuclei populated by multi nucleon transfer reactions, involving weakly bound projectiles where breakup/transfer induced fission probabilities are large. Importantly, such reaction may act as a surrogate reaction of some desired reaction for which the cross section is unknown. For example, if a compound nucleus (C) can not be formed in a desired reaction (a+A $\rightarrow$ C), it can be done by a transfer or ICF reaction (b+B $\rightarrow$ C+d), known as surrogate reaction. Such reactions are widely used to determine fast neutron induced fission cross-sections, extremely important for the Generation-IV reactor by employing surrogate ratio technique [31, 33].

1.4 Previous measurements on breakup or transfer induced fission reaction

A large number of measurements identifying breakup or transfer induced fission channels from either folding angle distributions or velocity distribution of fissioning nuclei

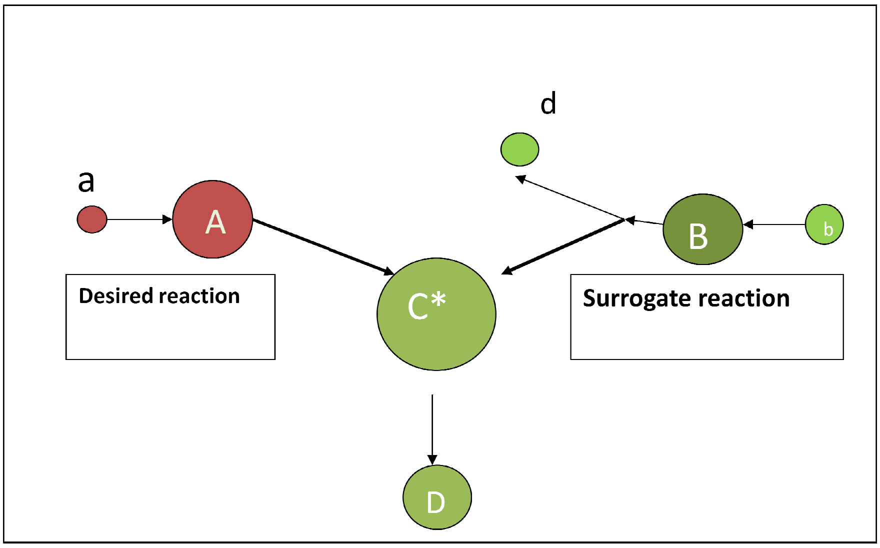

Figure 1.7: If a compound nucleus (C) can not be formed in a desired reaction (a+A $\rightarrow$ C), it can be done by a transfer or ICF reaction (b+B $\rightarrow$ C+d), known as surrogate reaction.

have been carried out. The disadvantage of such techniques is the lack of knowledge of a particular transfer channel and also chance of getting mixed with the complete fusion channel. In fact, for a light projectile such as ^{6,7}Li, the separation of breakup or transfer induced fission channel is not at all possible using the technique mentioned above. Then the direct coincidence technique between fission fragments and projectile like fragment is the only way by which one can distinguish breakup or transfer fission from inclusive fission. The advantage of such technique is that one can identify each transfer channel and carry out measurement for each channel. Only a few measurements on direct breakup or transfer induced fission reaction using the coincidence technique between fission fragments and projectile like fragment, is available in literature, as it needs a large detector array for detecting both light charged particle and fission fragments. Few results from experiments on breakup or transfer induced fission reaction have been described below.

1.4.1 Measurements of transfer induced FFAD

In the study of transfer induced fission following direct coincidence technique on ^{16}O + ^{232}Th system [34], Lestone *et al.* have observed a strong fission fragment angular correlation with respect to the recoil direction of the fissioning nuclei. However integration over all recoil angles results in a weak distribution relative to the beam direction. In another measurement, using the folding angle distributions of the fission fragments, Kailas *et al.* [35] have been able to separate the transfer induced fission and compound nucleus fission for ^{11}B+^{237}Np, ^{12}C+^{236}U and ^{16}O+^{232}Th systems. They concluded that at energies close to the Coulomb barrier, the transfer fission component is not significant enough to modify the anisotropy values obtained from the total FF angular distribution.

1.4.2 Measurements of FFMD of nuclei populated in multinucleon transfer reactions

Similarly, following direct coincidence technique, FF mass distributions for transfer induced fission channel have been obtained for several experiment as described below. FF mass distributions of two compound nuclei ^{227,228}Ac formed by transfer reactions have been obtained for the first time by Koneckny *et al.* [38], where they have extracted the mass distributions from ^{226}Ra(^{3}He,df) and ^{226}Ra(^{3}He,pf) reactions respectively. Using ^{239}Pu(d, pf) transfer fission, Nishio *et al.* [39] have studied the mass distributions of the ^{240}Pu composite nucleus via the super deformed β vibrational resonance. Hulet *et al.* [40] have studied the spontaneous fission of ^{259}Fm from its isomeric state with a half life of 1.5 s, which was produced in ^{257}Fm(t, pf) reaction. In a recent article by Leguillon *et al.* [32], the authors have simultaneously studied the FF mass distributions of several neutron rich isotopes of Th, Pa and U, populated by the multi-nucleon transfer channels in the ^{18}O + ^{232}Th reaction. Role of multichance fission at higher excitation energies have been demonstrated by Hirose *et al.* [30] in order to explain the FF mass distributions of nuclei populated in multinucleon transfer reactions on ^{18}O + ^{238}U system.

1.4.3 Measurement of ICF cross-sections

As mentioned in the last section, one can determine incomplete fusion cross-sections by measuring breakup or transfer induced fission events. Raabe *et al.* [29] has applied the above technique to obtain ICF cross-sections in ^{7}Li,^{7,9}Be +^{238}U reactions. In this method, first differential cross-sections for breakup or transfer induced fission are obtained as a function of emission angle of PLF. Then total angle integrated ICF cross-sections are determined.

1.4.4 Measurement of (n,f) cross-sections

Utilizing the novel property of a breakup or transfer reaction that if a nucleus can not be populated by a desired reaction, it can be done by a surrogate reaction, several cross-sections for neutron induced fission reactions useful for fast reactors have been determined. Surrogate method first employed by Britt and Cramer in 1970 [41, 42] is a well celebrated method to measure the (n, f) cross sections indirectly. Later on, the 'Surrogate Ratio (SR)' method has been proposed by Plettner *et al.* [43] for the same purpose. Recently, the SR method has been benchmarked and applied to determine several neutron induced fission cross-sections [33, 44, 45, 46, 47, 48, 49, 50]. Another method named 'Hybrid Surrogate Ratio (HSR)' method is also being used to determine the (n, f) cross-sections as done in Ref. [33] by Nayak *et al.*.

1.5 Motivation of the present thesis

Reactions involving weakly bound projectiles like ^{6,7}Li and ^{9}Be are known to exhibit many interesting features such as fusion suppression at above barrier energies, absence of threshold anomaly in the real part of optical potential, large alpha particles production and anomaly in fission observables. The present thesis work, however, focuses on the study of the effects of projectile breakup on fission by measuring the basic observables like fission fragments angular distributions (FFAD), fission fragments mass distribution (FFMD), fission fragments folding angle distributions (FFFAD) etc. in reactions involving weakly bound projectiles aiming to resolve some of the anomalies in fission observables.

For reactions involving weakly bound projectiles, there is a substantial contribution of transfer/breakup fission to total fission which is difficult to separate from compound nucleus fusion-fission. The aim of the present thesis work is to identify, separate and find out the effect of these breakup/transfer induced fission channels on the observables in inclusive fission channel (containing both fusion-fission and breakup/transfer induced fission) through exclusive measurements described below.

(i) As already seen in the previous discussions that there exists anomaly in inclusive angular anisotropy data compared to the statistical model prediction in reactions involving weakly bound projectiles [13, 14]. Similarly, inclusive FFAD measurements on ^{6}Li+^{232}Th system have been carried out and compared with statistical model calculations. If any deviation is found, investigations have been carried out whether it arises due to transfer or breakup channel. Hence FFAD for transfer or breakup induced fission have been exclusively measured for the same system at energies near the Coulomb barrier.

(ii) We have observed a difference in P/V ratio of FFMD between inclusive fission

and complete fusion-fission. Presence of kink like structure in inclusive FFFAD and enhancement of the width of FFFAD are also some of the interesting features in reactions involving weakly bound projectiles. In literature, breakup or transfer induced fission have been cited as one of the possible reasons. Now exclusive measurement on ^{6,7}Li+^{238}U systems have been carried out to explain the unusual behavior in FFFAD and FFMD by measuring the same in coincidence with PLF. There is also a scope to study the basic properties of a few nuclei which can not be populated using stable target and projectile. In particular, for ^{6,7}Li+^{238}U reactions, several composite nuclei are expected to be populated by the capture of unstable PLFs like t, ^{5}He and ^{6}He through different breakup/transfer induced fission channels.
Another interesting feature of weakly bound projectile is the complete fusion suppression at above barrier energies. In literature, for few cases the incomplete fusion cross-sections are found to be same as the missing complete fusion cross-sections. In this context, the incomplete fusion cross-sections on ^{6,7}Li+^{238}U systems have been measured.

(iii)Motivated by the same physics issues as mentioned above, the Mass-distributions on ^{10,11}B+^{238}U systems have also been measured. It is worth to mention that ^{10,11}B are also considered to be weekly bound projectiles [20, 51] but with larger breakup threshold compared to ^{6,7}Li. It may be mentioned that this experiment has been carried out with our recently developed MWPC detectors.

(iv) Fast neutron induced reactions have been proposed for the incineration of actinide materials which are produced in Th-U or U-Pu fuel cycles. The spent fuel will be burned in a dedicated reactor, where (n,2n) or (n,f) cross-sections can be used to reduce the content of radio toxic isotopes. The transfer/breakup induced fission reactions have been employed to extract indirect information on neutron induced fission cross-sections useful for nuclear waste management program. Here ^{238}Pu(n,f) and ^{236}Np(n,f) cross sections have been determined by surrogate ratio method by measuring fission fragments on ^{6}Li + ^{232}Th,^{235}U systems.

The thesis has been organized as follows. In Chapter 1, a brief introduction with the present status of the field and general motivation is presented. General experimental techniques used for the detection of fission fragments and projectile like fragments are presented in Chapter 2. The developmental work on MWPC detectors is described in Chapter 3. The results on fission fragment angular distribution for inclusive as well as transfer or ICF-fission are presented in Chapter 4. The results from the measurement of mass distributions for inclusive and ICF/transfer fission for ^{6,7}Li+^{238}U systems are described in Chapter 5. Measurements of mass distributions on ^{10,11}B+^{238}U systems are presented in Chapter 6. Determination of neutron induced fission cross sections using surrogate reactions is described in Chapter 7. Finally, the conclusions of the thesis and future scope of the work are highlighted in Chapter 8.

Chapter 2

Experimental Tools

As discussed in the introductory Chapter, the study of the present thesis aims at finding the transfer/breakup effect of weakly bound projectiles on fission observables in reactions involving such projectiles. It also aims at determining the neutron induced fission cross-sections useful for nuclear waste management purposes utilizing the transfer or breakup induced fission reactions. In fission reactions, transfer or breakup induced fission events easily get mixed up with compound fusion-fission, which are not easy to separate. There are two ways to separate these contributions.

(1)Indirect technique: one can apply folding angle technique or $v_{\|}$ vs. $v_{\perp}$ plots (to be discussed later) to separate these two, although which is not very reliable to identify individual transfer channel.

(2)Direct coincidence technique: By detecting projectile like fragments (PLF) in coincidence with fission fragments, individual transfer channels can be reliably separated out from the compound nucleus fusion- or complete fusion- fission channel.

As mentioned in Chapter 1, four experiments have been carried out detecting fission fragments in coincidence with the projectile like fragments for reactions involving weakly bound projectiles and actinide targets. Out of these four, three experiments are based on the measurements of basic observables like FFAD and FFMD. The fourth

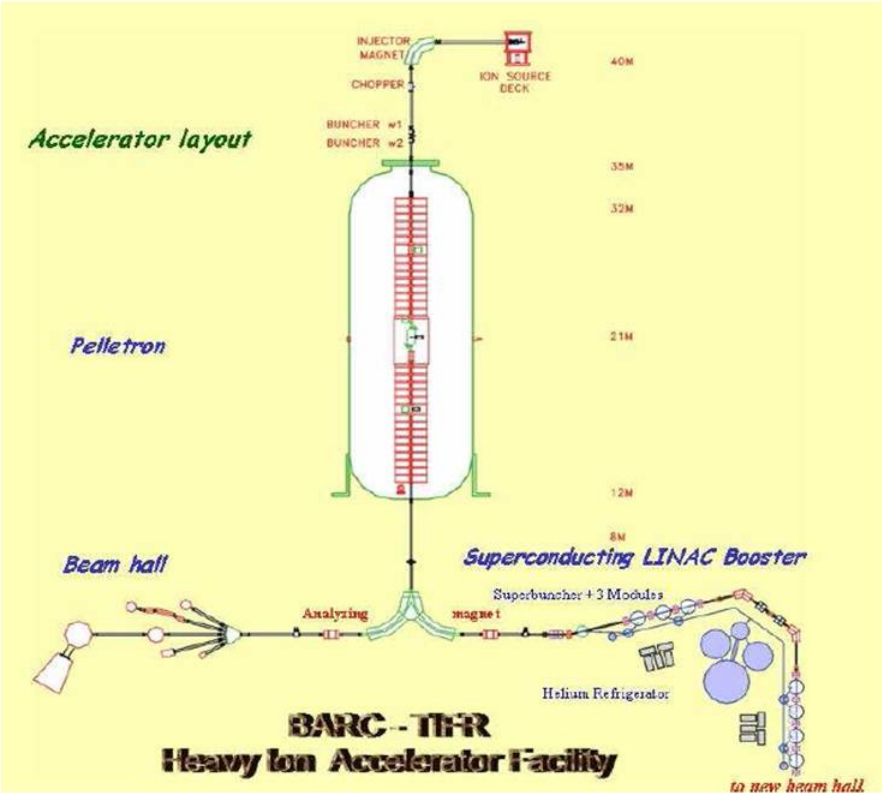

Figure 2.1: The schematic drawing of the accelerator facility

one is the simplest FF and PLF coincidence experiment to determine neutron induced fission cross-sections using surrogate technique.

The main ingredients to carry out an experiment on a nuclear reaction are: an accelerator facility for delivering beam, a target, a scattering chamber and detectors to detect reaction products. A brief discussion on the accelerator facility used for carrying out the experiment, target preparation techniques, different types of detectors used in the experiment have been discussed below.

2.1 Accelerator facility

Two accelerators, one at TIFR, Mumbai and the other at IUAC, New Delhi have been used for all the experimental nuclear reaction measurements of the present thesis work.

Measurement of FFAD on ^{6}Li+^{232}Th system, measurement of FFMD on ^{10,11}B+^{238}U systems and surrogate measurement on ^{6}Li+^{232}Th,^{235}U systems to determine neutron induced cross sections have been performed at BARC-TIFR Pelletron-Linac facility, Mumbai. Other experiment on FFMD measurements on ^{6,7}Li+^{238}U systems has been carried out at 15UD Pelletron accelerator facility, IUAC, New Delhi. As a basic operation principle of a Linear accelerator, the one for BARC-TIFR Pelletron-Linac facility has been described below. In this accelerator, negative ions extracted from a SNICS ion source at the top are mass analyzed using a 90° magnet (injector magnet) before injecting into the low energy accelerating tube. At the injector magnet all the ions having same charge state (1^-) have same energy and pass across the same pre-acceleration voltage. A particular ion species is selectively injected into the accelerating tube by setting the appropriate magnitude of magnetic field. High terminal voltage V_T million Volt has been set at the middle, which causes the negative ions to accelerate downwards and to gain V_T MeV amount of energy. The maximum terminal voltage upto 14MV is achievable in this facility. At the terminal the accelerated negative ions pass through a stripper, which can be a carbon foil of thickness $\sim 5\ \mu g/cm^2$ or a small volume of gas. While passing through the stripper the negatively charged ions lose electrons resulting in a distribution of positively charged ions which further gets repelled downwards by the positive terminal voltage, thus achieving qV_T amount of energy. Thus total amount of energy becomes (q+1)V_T MeV. After the ions come out of the accelerating tube, a particular charge state and hence a particular energy is selected by 90° bending magnet (analyzing magnet). The energy of the analyzed ions of mass A and charge state q in the present accelerator is given by the relation $B = 720.46\frac{\sqrt{AE}}{q}$, where B is the magnetic field in Gauss and E is the energy in MeV. This analyzed beam of ions with high energy resolution (ΔE $\sim$ 2 keV) is then switched to various experimental beam lines using a switching magnet. There are five beam lines among which 0° beam line in Old beam hall and 30° beam line in Hall-1 have been used for performing the experiment.

2.2 Target preparation

Thin targets are required for the the study of fission fragments, otherwise the fission fragments will either stop in the target and remain undetected or will loose a lot of energy before detection. For FFAD measurement, typical target thickness required is ~100-500 $\mu g/cm^2$. But for mass distribution measurement it should be even thinner. Energy loss in the target material modifies the measured velocity distribution of the fragments and hence affects the mass energy distribution derived from kinematical relations involving the FF velocities. Smaller target thickness $\sim$ 100 $\mu g/cm^2$ introduces less uncertainty in the derived mass distributions, although it is very much challenging to prepare such thin targets.

For mass distribution measurement $\sim$ 100 $\mu g/cm^2$ thick ^{238}U target sandwiched between $\sim$ 15 $\mu g/cm^2$ ^{12}C is prepared using evaporation method. For FFAD measurement and neutron induced fission cross-section measurement, $\sim$ 400-1300$\mu g/cm^2$ ^{232}Th target has been prepared using rolling method. This method does not require any kind of backing and therefore it is easy to prepare a target following this method. However, it has a limitation that we can not prepare very thin target using this method.

2.3 General purpose scattering chamber

All the measurements have been carried out in general purpose scattering chamber (diameter is ≥1.0 m) either in Mumbai (30° beam line in Linac Hall1 and 0° beam line in Pelletron Hall) or in New-Delhi (GPSC). Each chamber is equipped with two rotatable arms for mounting detectors and a target ladder capable of holding six targets at a time. Height adjustment of the target ladder and rotations of the arms are performed either manually (for GPSC at 0° beam line, Mumbai and New-Delhi) or using a programmable software (for GPSC at 30° beam line, Mumbai). Each chamber is also capable of holding hanging detectors for monitoring incident beam flux.

2.4 Detectors

Different types of detectors including gas detectors, scintillation detectors and semiconductor detectors have been used in the experiment. Semiconductor detectors and CsI(Tl) scintillator detectors have been used for detecting PLF, whereas semiconductor detectors and MWPC detectors have been used for detecting fission fragments.

2.4.1 Semiconductor detector

Silicon semiconductor detectors having band gap of ∼1.1eV are used for the detection of both, light charged particles and fission fragments. Two types of silicon detectors: (i) surface barrier detector having smaller area and (ii) strip detectors having larger area, are used for the detection of projectile like fragments. Typical images of the detectors are shown in Fig. 2.2. We use position sensitive strip detector having 16 vertical strips, with a total active area of $5 \times 5\ cm^2$. The operating principle for both types of detectors are same.

When a charged particle falls on the depleted region of the detector under reverse biased condition, electron and hole pairs are created proportional to the energy deposited in the detector. An electrical pulse is generated during the collection of electrons. The energy loss which varies with the incident energy (E), mass (M) and charge (Z) of the incident particle (non-relativistic) is given by the Bethe-Bloch formula ($\frac{\Delta E}{\Delta x} = C\frac{MZ^2}{E}$). Now if the energy loss ΔE is plotted against the incident energy, light charged particles with different Z and A should come in different hyperbole. In

Figure 2.2: Images of two silicon surface barrier detectors (left) and one strip detector (right) .

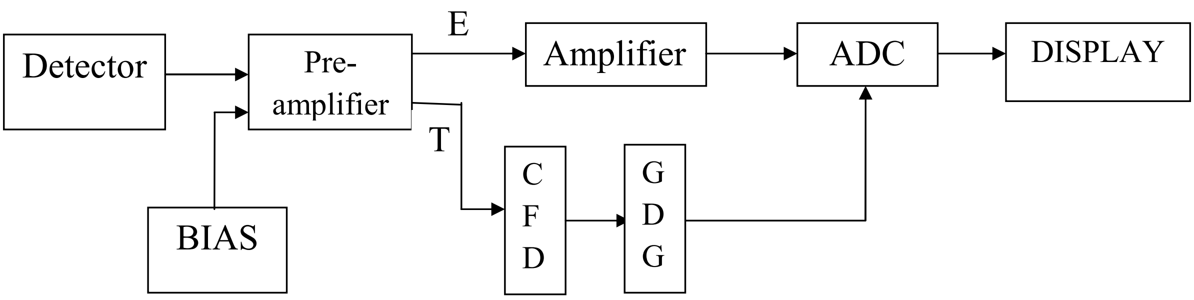

Figure 2.3: Schematic drawing of electronics circuit for processing of signals .

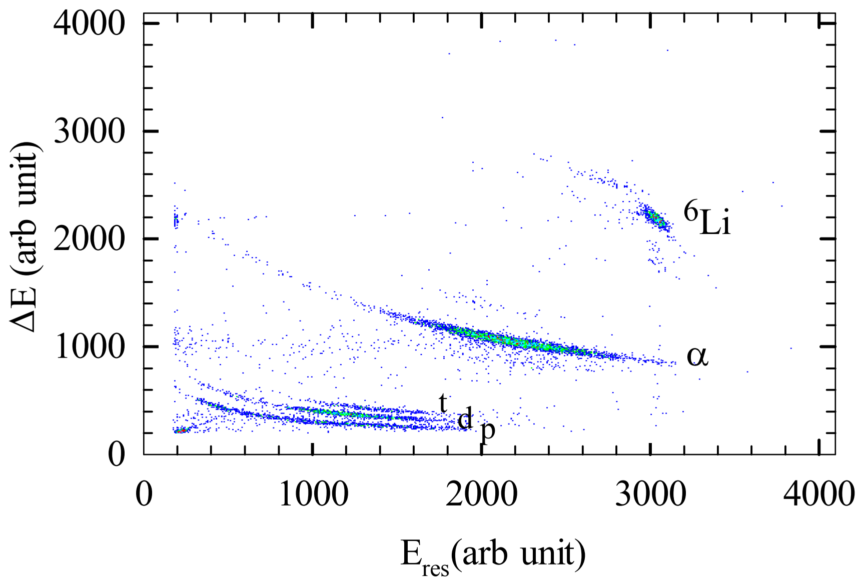

Figure 2.4: Typical 2D spectrum showing different particle bands with Z=1-3 .

practice, it can be achieved by measuring the energy loss (ΔE) in a relatively thin detector (ΔE detector) followed by a second detector (E detector) in which the particle stops. The sum of the detector signals gives the initial (total) energy of the particle. This arrangement is called ΔE - E telescope.

As shown in Fig. 2.3, signal obtained from a detector is first processed through a preamplifier which creates two signals: one energy signal (slow) and one timing signals (fast). After initial amplification from pre-amplifier module, the energy signal is processed through an amplifier for further amplification following which the signal is fed into an ADC (Analog to Digital Converter). The timing signal is processed parallelly through a CFD (Constant Fraction Discriminator) and a GDG (Gate and Delay Generator) to generate a master gate which enables the ADC to record the signal. For a strip detector having 16 strips, all the signals coming from 16 strips are processed together through a compact 16 channel Pre-amplifier (MPR16), an amplifier(MSCF16) and an ADC. ADC signals from ΔE and E detectors are simultaneously plotted to identify different types of incident particles. As shown in Fig. 2.4, a typical 2D

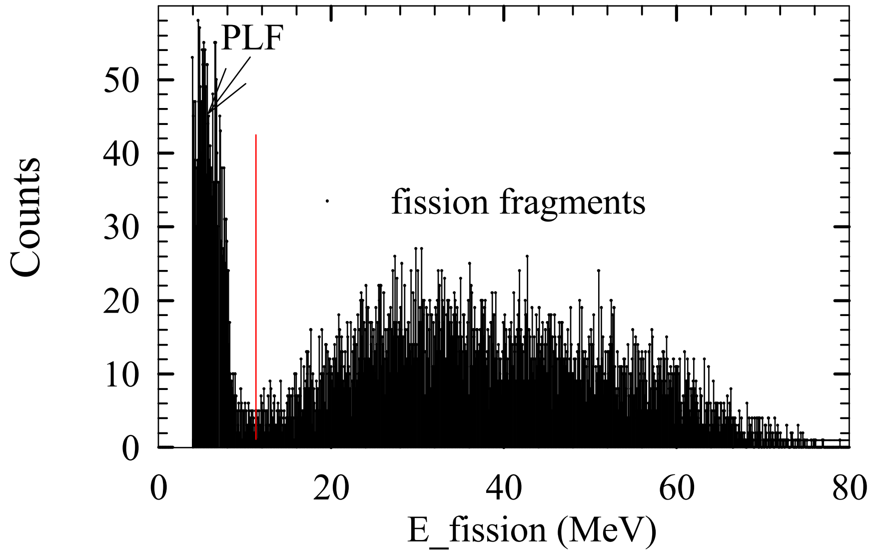

Figure 2.5: Typical 1D spectrum showing clear separation between fission fragments (right of red line) and projectile like fragments (PLF) (left of red line).

spectrum obtained from a strip detector shows different particle bands with Z=1-3 obtained in $^{6}Li+^{232}Th$ reaction.

For fission fragments, the above energy loss formula is not exactly valid. The highly positively charged fission fragments having energy $\sim$ 1MeV/u, tend to pick up few electrons from the interacting material. Consequently, it reduces own effective charge. The probability of picking up electrons goes down with increasing kinetic energy. As a result, the effective charge increases with increasing energy, thereby causing more energy loss in the detector with increasing kinetic energy, which is contrary to energy loss formula for light charge particle. However, the fission fragments can be identified by their high specific energy loss (dE/dx) or smaller range as compared to projectile like fragments. As shown in Fig. 2.5, a typical 1D spectrum obtained from a silicon strip detector shows a clear separation between fission fragments and PLF.

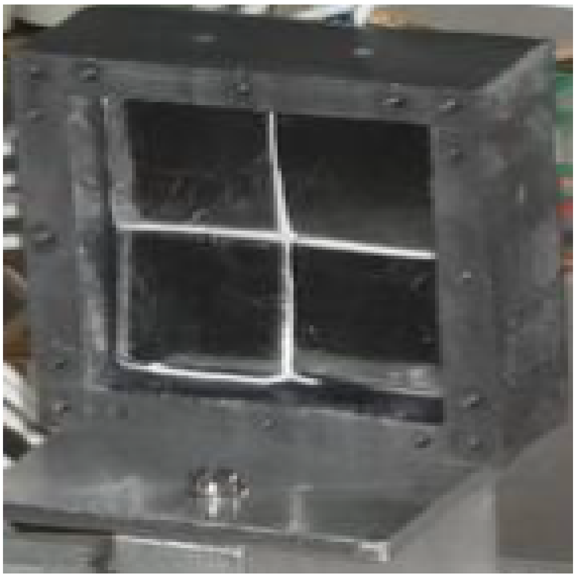

Figure 2.6: Image of Csi (Tl) detector showing mounting of four crystals together .

2.4.2 Scintillation detector

Inorganic (CsI(Tl)) scintillator detectors are used for the detection of PLF. An image of CsI (Tl) detector showing mounting of four crystals together has been shown in Fig. 2.6. Operating principles of inorganic scintillation detectors are little bit different from the ones of semiconductor detector. Here the incident particle excites an atom of the detector material. De-excitement of the atom produces some scintillation light which generate electrical signal in photo multiplier tube. The scintillation light contains slow as well as fast components. The energy levels of the activator atoms in the inorganic scintillators help to produce fast component of the signals. If we plot the fast (Short) component against the slower (Long) one, we will be able to distinguish different kinds of incident particles. As shown in Fig. 2.7(a), the different particle bands (^{6}Li,α,t,d,p) have been separated out. It happens due to different dE/dx for different incident particles. More is dE/dx, higher is the short component of the scintillation light for the same long component. As a result, ^{6}Li band comes top in the Long vs. Short plot (Fig. 2.7(a)). On the other hand, if we plot PID=(1-Short/Long) against the

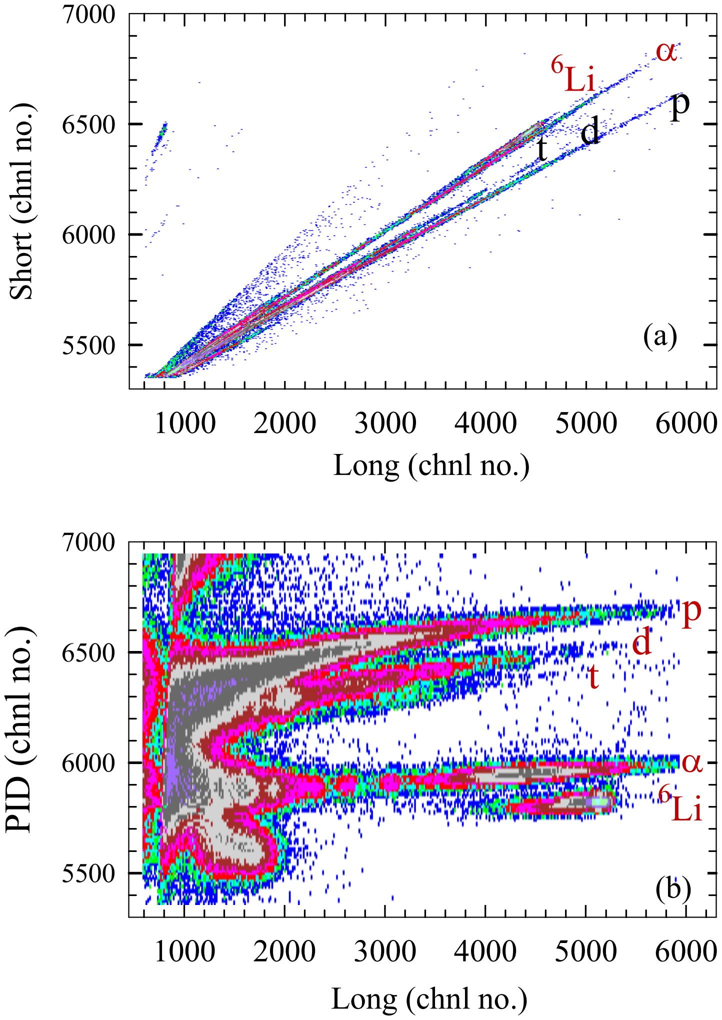

Figure 2.7: Typical Short vs. Long plot (a) and (1-Short/Long) vs. Long plot (b) obtained from CsI(Tl) scintillator detector in ^{6}Li+^{238}U reaction.

Long component, the same ^{6}Li band comes in the bottom and other bands α,t,d,p come sequentially on top of ^{6}Li band as shown in Fig. 2.7(b). As Long component corresponds to full collection of scintillation lights, it carries the energy information of the incident particles. The pulse processing circuit is same as the one used for semiconductor detector. The shaping time in Linear amplifier for Short and Long components have been fixed as 400 ns and 2 μs respectively.

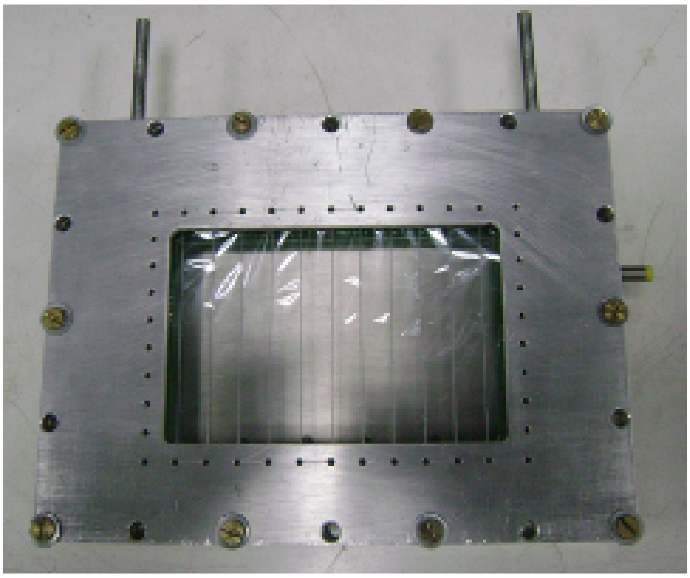

Figure 2.8: Image of a MWPC detector having 5 PCB frames inside .

2.4.3 Multi-wire proportional counter

Apart from semiconductor detectors, another type of detector known as multi-wire proportional counter (MWPC) has been used for detecting fission fragments in the present measurements. It is basically a gas detector operated in the proportional region. An image of a typical MWPC detector is shown in Fig. 2.8. The position resolution of a MWPC detector is far better than that of a semiconductor detector. Semiconductor detectors consist of 16 strips each with width of 3 mm. In contrast, there are many closely spaced wires in MWPC detectors to determine position (x and y) information, where each wire acts like a cylindrical proportional counter. It consists of either 5 PCB frames (Cathode, X frame, Anode, Y frame and another Cathode) or 3 PCB frames (X frame, Cathode and Y frame).

To detect two fragments simultaneously, we need two MWPC detectors which should be placed in either side of the beam direction. Here central Anode frame (for detector with 5 PCB frames) or central Cathode (for detector with 3 PCB frames) frame provide us the timing information of the incident particles. The MWPC detectors

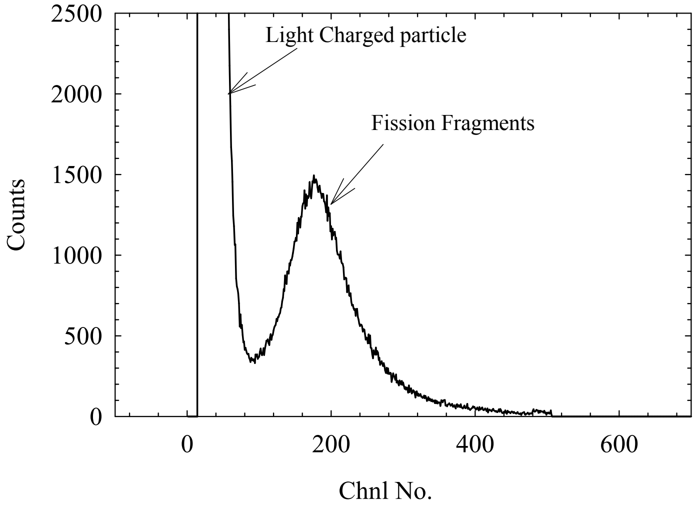

Figure 2.9: Typical cathode spectrum recorded in ^{11}B+^{238}U reaction showing clear separation between light charged particle and fission fragments.

with 3 PCB frames have been used in the experiment on ^{6,7}Li+^{238}U reactions. We have developed two MWPC detectors consisting of 5 frames and used in the experiment on ^{10,11}B+^{238}U reactions. The detailed design, operating principle, electronics circuit etc. have been presented in the next chapter. Here we have shown the separation between light charged particles and fission fragments obtained from cathode spectra in Fig. 2.9. We also get a clean separation in the 2D spectrum of time-of-flights obtained from two MWPC detectors (to be discussed in the next chapter). Here the start of the time-of-flight spectrum is taken either from a pulsed beam or from another gas detector known as START detector.

After equipped with all the instrumentations, required beam has been bombarded on the specific targets for the reactions to take place. Since the arrangement of the different kinds of detectors vary experiment to experiment, details of each experimental arrangement will be presented chapter wise.

Chapter 3

Development of MWPC Detectors

Detection of charged particles produced in a nuclear reaction is very crucial to understand the reaction mechanism. Conventionally silicon detectors are used for the detection of light charged particles. However, for heavy particles like fission fragments, these are not suitable due to their fast degradation of performance with radiation damage and small geometrical efficiency. Large area position sensitive silicon detectors are commercially available not only at high cost but also with limited sustainability when used for fission fragments. To overcome this, other detectors such as position sensitive micro channel plates 'CORSET' gas ionization chambers, and proportional counters have been developed. Large area micro channel plate system is difficult to develop and is generally fragile. Gas ionization chambers have poor count rate handling capabilities, and also have poor timing, position, and energy resolutions.

The multi-wire proportional counter (MWPC) detectors have been an efficient solution to the above problems which provide very good timing and position resolutions, higher count rate handling capability and also insensitivity to radiation damage. They can also be fabricated easily with various sizes according to the need for experimental investigations. Moreover, the operating parameters such as gas pressures and voltages on electrodes can be adjusted to make it transparent to unwanted light particles and

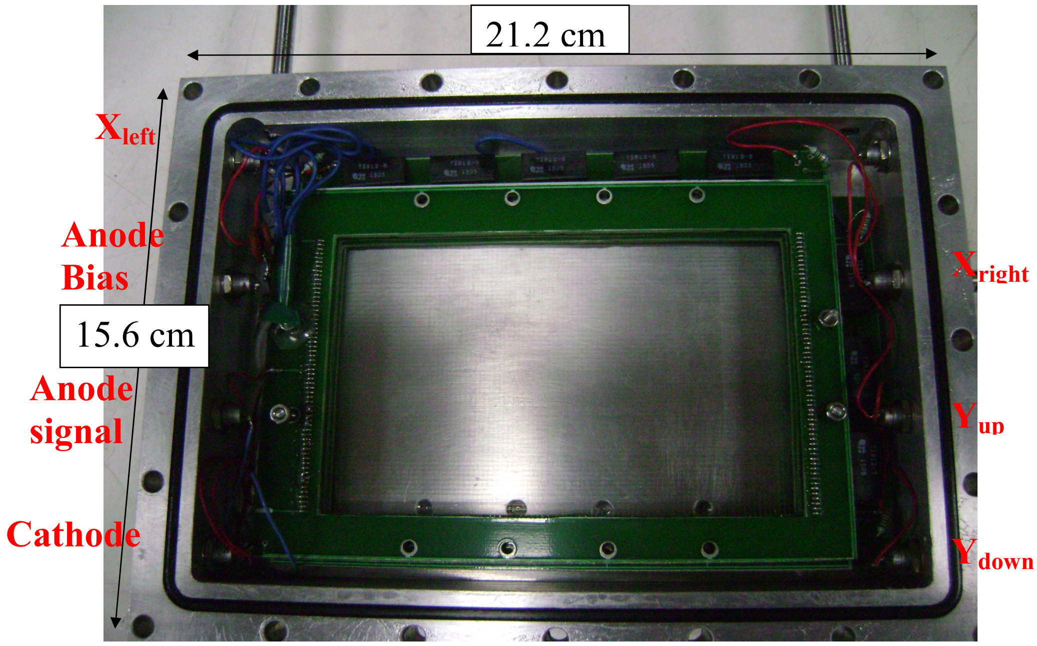

Figure 3.1: The detector cavity containing 5 PCB frames and 7 feedthrus for signals and bias supplies.

make it sensitive only to heavier particles such as fission fragments. Although energy resolution of the detector is very poor, it provides a clear distinction between light and heavy charged particles.

The development of gas detectors was truly revolutionized by the invention of the MWPC [52] by Georges Charpak in 1968. Later Amos Breskin developed a detector (known as Breskin detector) [53, 54] which consisted of a pre-amplification stage operating as a parallel plate chamber (PPAC) directly coupled to a MWPC. To understand fission dynamics near Coulomb barrier, we have also developed two compact MWPC detectors for the detection of fission fragments, which are similar to Breskin detectors. Each of the detectors are having identical dimensions, identical design features and identical performance. It consists of 5 PCB frames (2 cathodes, 1 anode, 1 X-frame and 1 Y-frame) and there are 7 LEMO feedthrus as shown in Fig. 3.1. Both cathode frames are connected to a single LEMO connector using which simultaneously we sup-

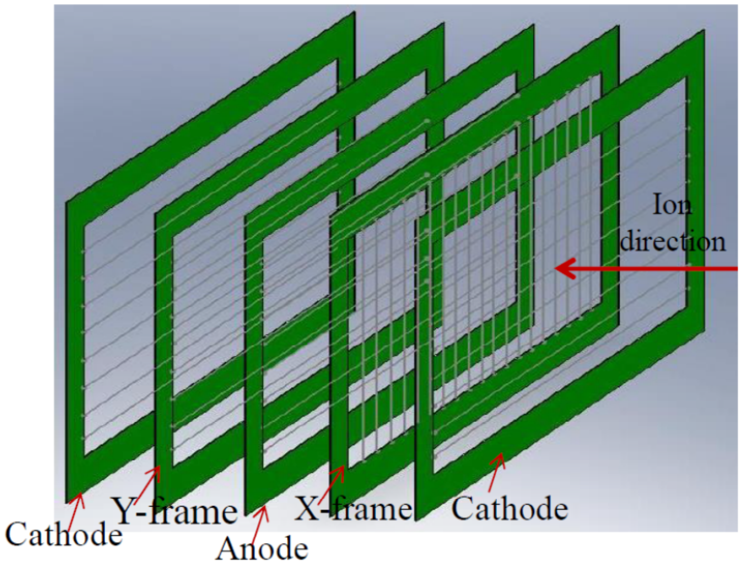

Figure 3.2: Schematic diagram showing arrangement of PCB frames.

ply bias voltage and collect the signal with the help of a charge sensitive pre-amplifier. There are two separate connections for anode frame: one for supplying bias and another for extracting signal. X-position frame have two connections: X_{left} and X_{right}. Similarly two output Y_{up} and Y_{down} have been taken from Y-position frame. The detector has been successfully tested with sources and in-beam experiment. The detailed design and the results of its performance testing have been described below.

3.1 Detector design

The detector has been designed based on the requirements that (i) it should provide good position (∼1.5 mm) and timing resolution (∼1ns) (ii) it should provide a reasonably good angular coverage and (iii) it should be compact so that it can be placed at extreme backward angle without blocking the beam direction. The design, similar to one developed by Breskin [54], can fulfill the above criteria.

The core of the detector consists of five frames each with an active area 12.5×7.5 cm^2. As shown in Fig. 3.2, the arranged wire frames starting from the entrance of

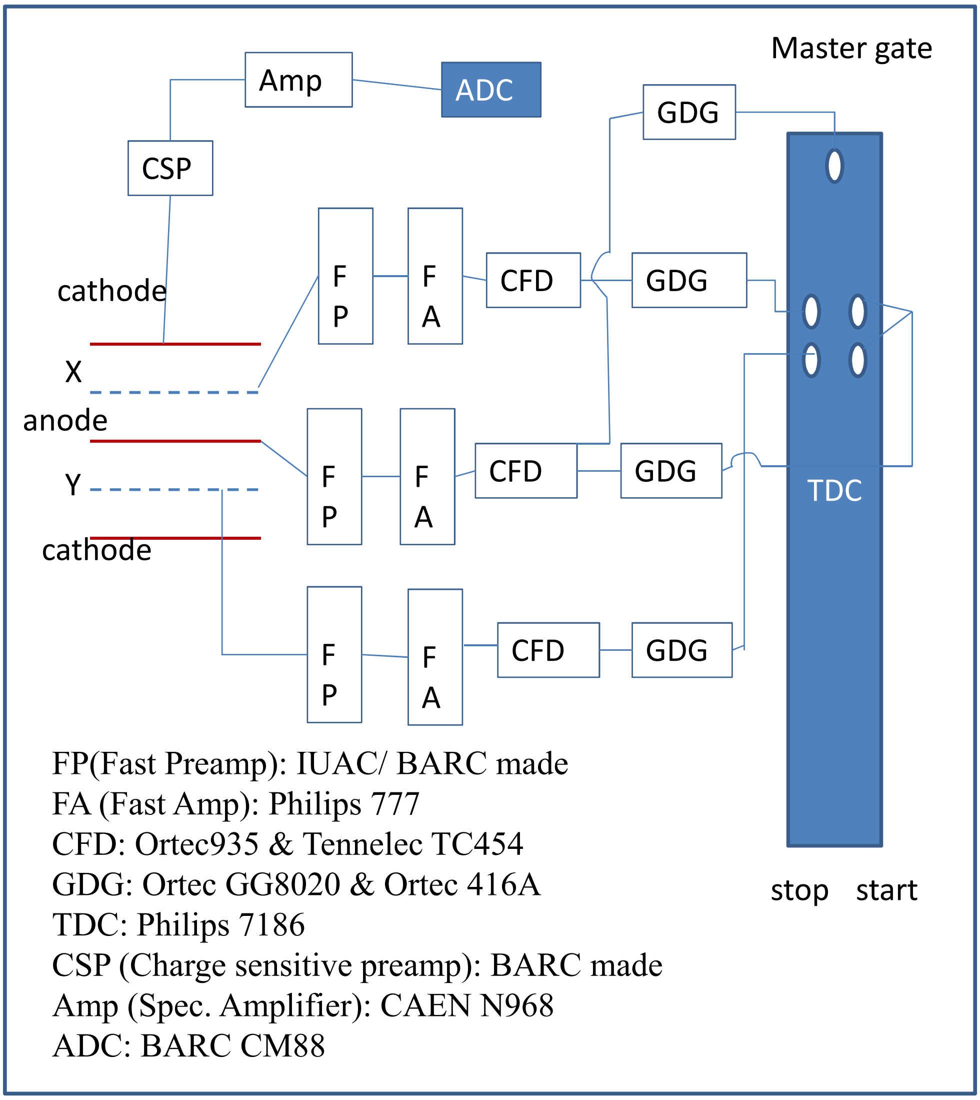

Figure 3.3: Schematic of the electronic circuit used for data acquisition.

the detector are: a cathode, an X-frame, an anode, a Y-frame and a second cathode (shorted with the first cathode). Such a design provides high gain for both heavy and light ions at low pressure [$\sim$1-5 torr]. All wire frames are made from gold plated tungsten wire with 20μm diameter, stretched on a 1.6 mm thick printed circuit board. All the frames are stacked one after another. The X frame is made from 100 wires whereas the remaining frames have 60 wires each. The separation of two consecutive wires is 1.27 mm. Using commercially available rhombus delay line integrated chips (model TZB12-5) position information from X and Y frames are extracted. In position electrodes, wires are shorted in pair and connected to one tap of delay line chip. End to end delay in X and Y-position frames are 100 and 60 ns, respectively. The position frames are kept at ground potential by terminating both ends of delay lines through 150 kΩ resistors. The electrode assembly is mounted inside a rectangular metal housing milled out from a solid aluminum block of dimension 21.2 cm $\times$ 15.6 cm. At the entrance of the detector 0.5 μm thick mylar foil has been used to isolate it from the vacuum chamber. The foil is supported by nylon wire. The detector is operated with flowing iso-butane gas at $\sim$1-4 torr pressure.

3.2 Detector performance testing

3.2.1 With source

The detector has been tested with ^{229}Th alpha source and ^{252}Cf fission source as well as with in-beam experiment. For fission fragment detection +360V and -180V were supplied to anode and cathode respectively. Readout electronics is as important as other parameters like gas pressure, operating voltages etc. to get its best timing and position resolution. A schematic drawing of electronics setup is shown in Fig. 3.3. The images for position, cathode and anode signals as observed in oscilloscope are shown in

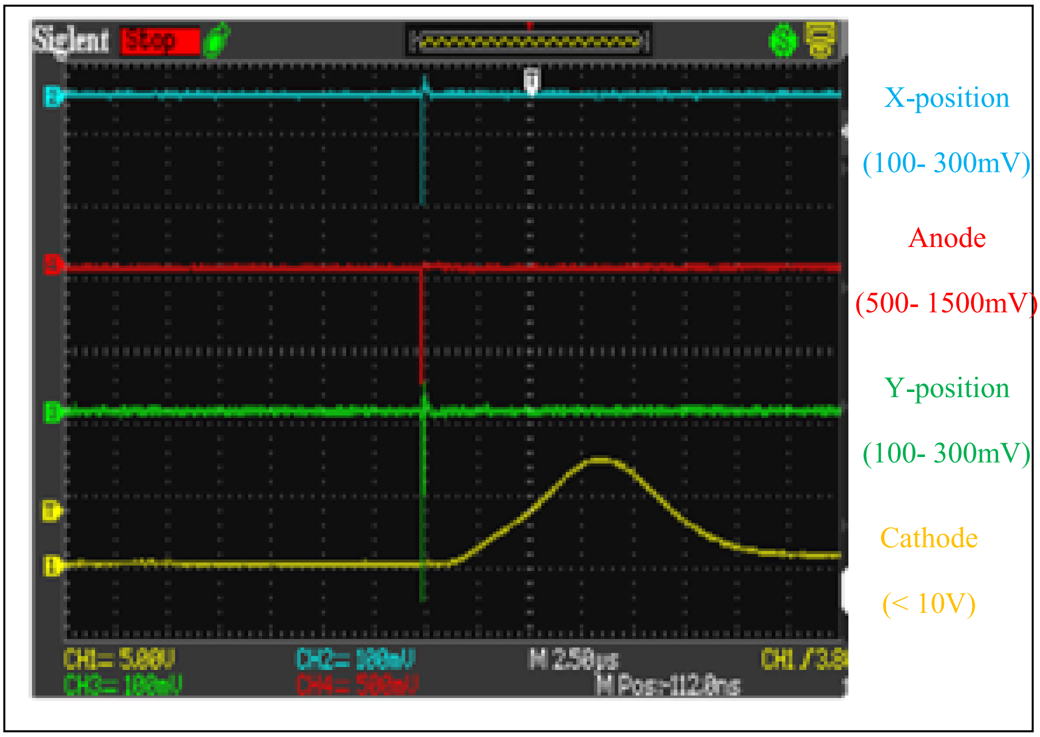

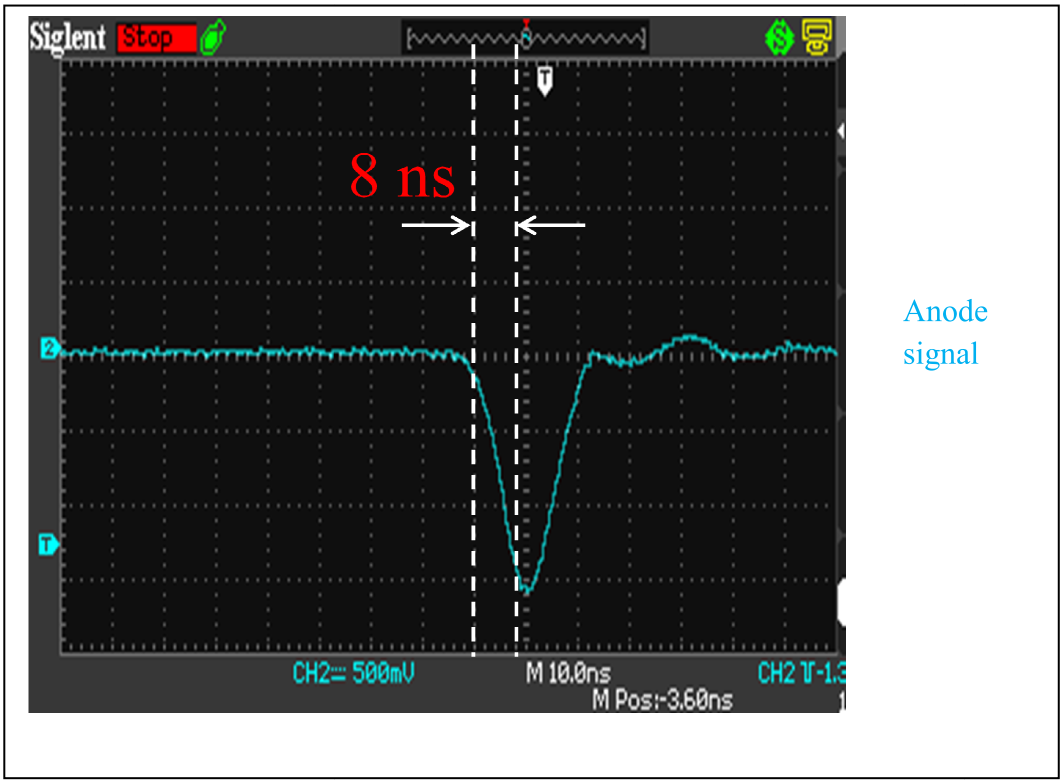

Figure 3.4: (top panel) Pre-amplifier output of all the signals in oscilloscope and (bottom panel) zoomed-in view of the anode signal showing rise time ∼8 ns.

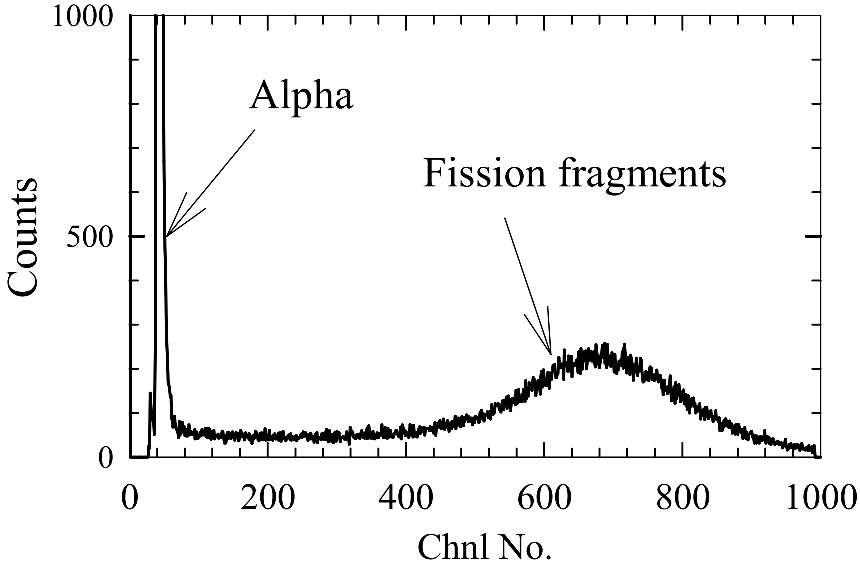

Figure 3.5: Cathode spectrum showing clear distinction between alpha particles and fission fragments.

Fig.3.4. The anode signal (negative) is read out by a non-inverting fast pre-amplifier developed inhouse and the pulse height of 500 mV-1.5V was observed with a rise time less than 10 ns as shown in Fig. 3.4 (bottom panel). The positive signals from the position wire frames are processed through inverting fast preamplifiers to convert the polarity. Typical pulse height of 100-300 mV was observed for the position signals. It is further amplified by a fast amplifier (PHILIPS 777). All the timing signals are fed into CFD (ORTEC935/TENELLEC TC454) to generate NIM logic pulse. After adjusting the timing delay using GDG module(ORTEC GG8020/PHILIPS741) one can use anode and position signals as start and stop signals respectively for timing measurements whereas anode signal is used for the master trigger in the data acquisition system. The cathode signal which is a measure of energy deposition in the active volume of the detector is read out by homemade low gain charge sensitive preamplifier. The pre-amplifier output of the cathode signal is fed into a linear amplifier which shows typical pulse height of 1-10 V. The recorded cathode spectrum as shown in Fig. 3.5 also shows clear distinction between light and heavy charge particles.

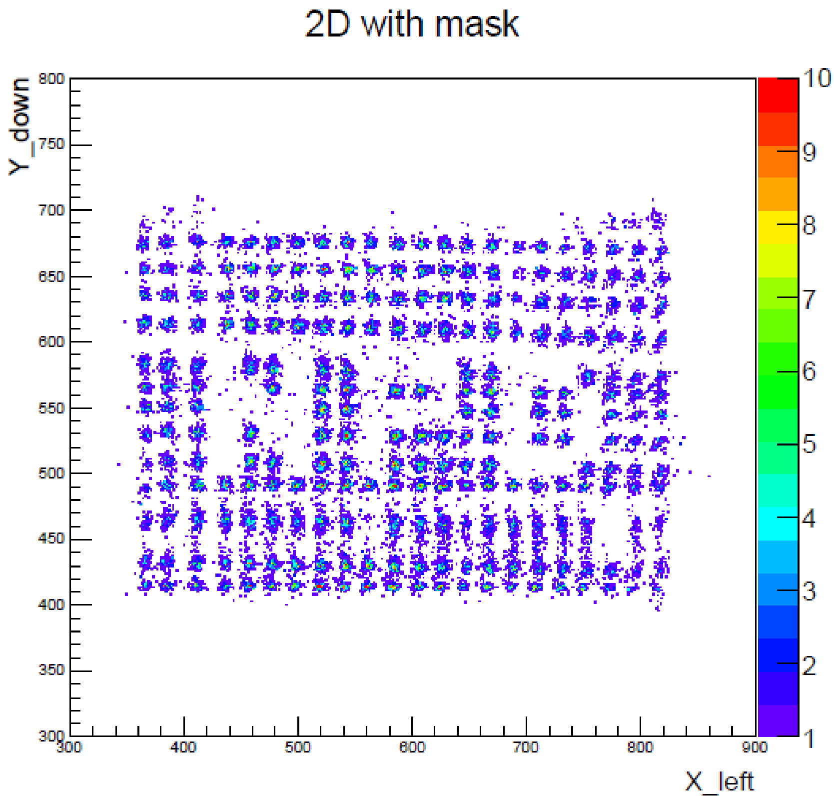

Figure 3.6: 2-D pattern obtained from the detector testing.

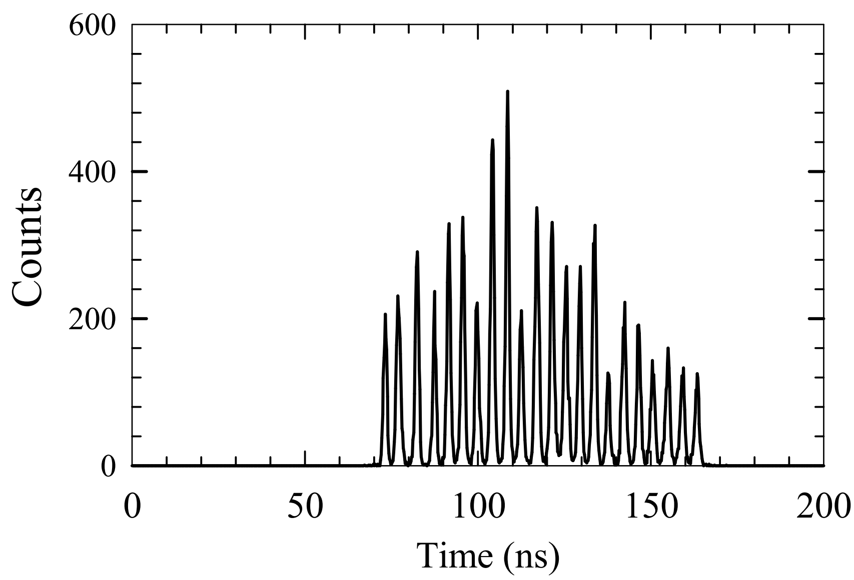

Figure 3.7: X-projection of the above 2-D spectra.

To determine position resolution one mask made of aluminum plate with (22 $\times$ 14) holes with 1 mm diameter and separation of 5 mm between two adjacent holes were placed in front of the detector at a distance of ~25 cm from the source and the mask is at ~2 cm from the first electrode. As shown in Fig. 3.6, the projection of the mask on the detector is reproduced hole by hole in the two dimensional spectrum when we plot the spectrum of X_{left} versus Y_{down}. Some holes were deliberately blocked to create the shown pattern. The x projection of the mask on the detector has been shown in Fig. 3.7(b) where peak to peak separation is 5 mm. The average FWHM of the peaks for X frames have been found to be 1.5 mm. Similarly the average FWHM of 1.7 mm has been obtained from the y projections (not shown here) of the above 2-D spectra . Slightly broader FWHM of the Y positions are due to the location of the Y wire frame at larger distance from the source, compared to the X wire frame. Thus the projection of the hole on the Y wire frame is likely to be more magnified as compared to X.

From the individual spectra of X_{left}, X_{right}, Y_{up} and Y_{down}, one get the x,y position information of a event. However, if we record all the signals simultaneously, one can obtain x position spectrum by taking the difference between X_{left} and X_{right} (i.e. $X_L - X_R$). Similarly, y position can be obtained by taking the difference between Y_{up} and Y_{down} (i.e. $Y_U - Y_D$). Interestingly the sum of the position signals (X_L+X_R) and (Y_U+Y_D) should be equal to the total delay of the delay line which should remain constant. This is used to eliminate events arising from reflections and pickups in delay lines and transmission cables, weak signals which are triggered by CFD on one side but not on the other side, and multiple hit events. While tuning electronics these widths are monitored to get the best possible width as narrow as possible. The width of these peaks is a measure of the time dispersion in the detector as well as electronics setup. Time dispersion of 1.7 ns in the detector as well as electronics setup has been determined from the width of the peaks of sum spectra as shown in Fig. 3.8. With

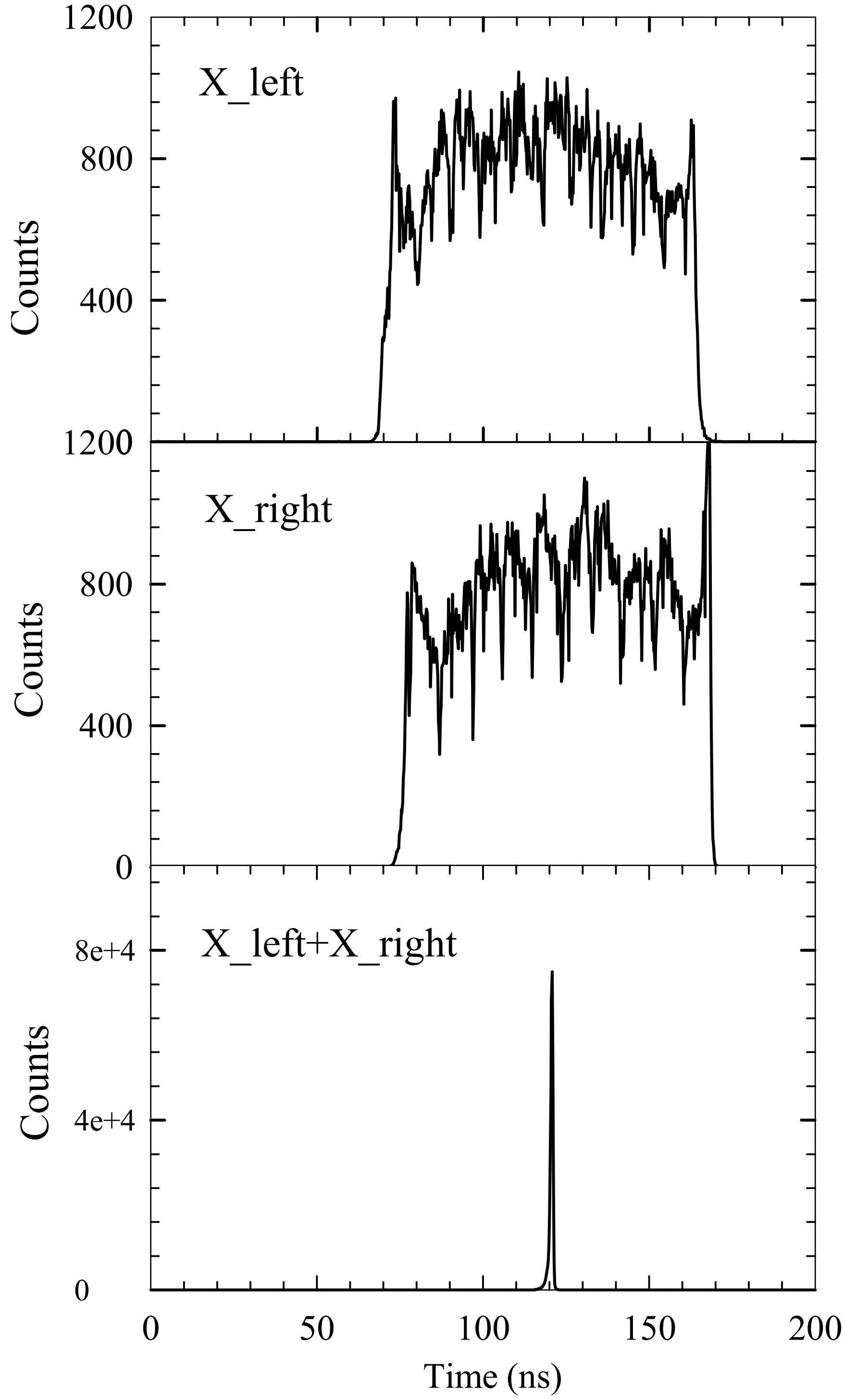

Figure 3.8: X_L, X_R and $X_L + X_R$ spectra.

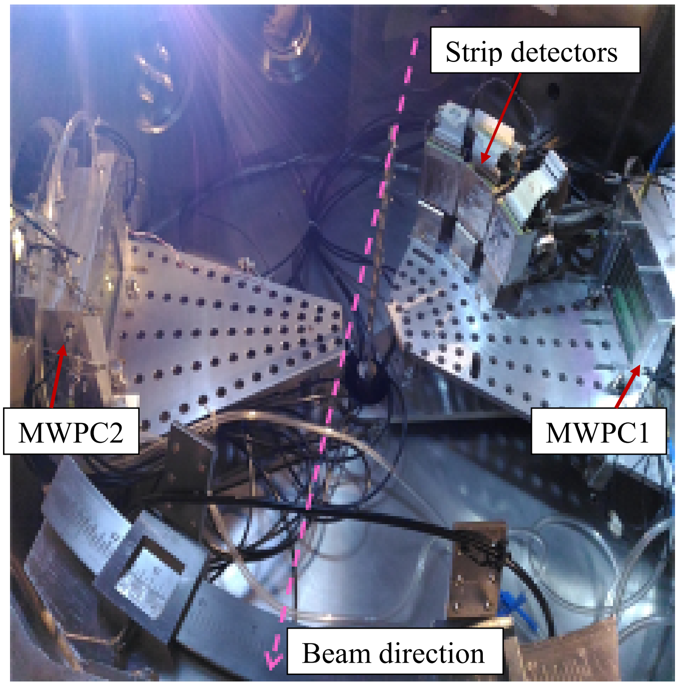

Figure 3.9: The two MWPC detectors have been placed for in-beam testing.

satisfactory test performance including position resolution and time dispersion, the detector is made ready for online fission measurements.

3.2.2 In-beam testing

The detectors were tested successfully with fission fragments produced in a reaction on $^{10,11}B$ + ^{238}U systems using general purpose scattering chamber at BARC-TIFR Pelletron-Linac facility. As shown in Fig. 3.9, two MWPC detectors (MWPC1 and MWPC2) have been placed at folding angles at a distance of 41.4 cm and 39.4 cm respectively from the target centre. Pulsed RF beams of $^{10,11}B$ were used to get the start signal of the time-of-flight. Master has been generated using "AND" logic operation between RF signal and "OR" of GDG output of two anode signals. The correlations of time-of-flights for the two fission fragments, which distinguishes the fission fragments from projectile like fragments, have also been shown in Fig. 3.10. After calibrating the position and timing spectra, one can extract velocity and angle information using

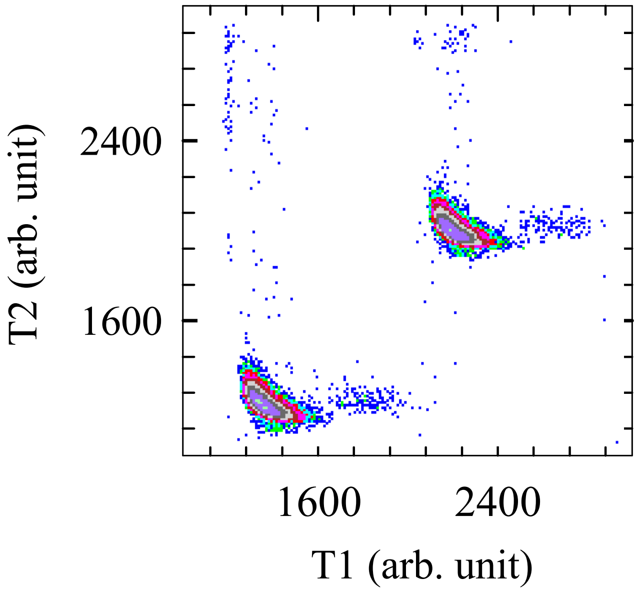

Figure 3.10: The correlations of time-of-flights of two fission fragments obtained in $^{11}B+^{238}U$ reaction.

which kinematical relations can be applied to derive mass distributions, folding angle distributions, total kinetic energy distributions etc. The detailed results on the fission observables obtained from the in-beam testing have been presented in Chapter 6.

Chapter 4

Fission Fragment Angular Distributions in ^{6}Li+^{232}Th reaction

Fission fragment angular distribution is an important observable where the projectile breakup may play a dynamic role in modifying the angular anisotropy. The FF angular distributions for CF-fission and transfer/breakup induced fission are expected to be different as the temperature and the angular momentum in the fissioning nuclei are different in these two processes. In our earlier measurements for ^{6,7}Li+^{235,238}U systems [13], the FF angular anisotropies have been observed to be higher than the ones expected from SSPM predictions. It has been concluded that the observed discrepancy may be due to the combined effect of entrance channel dependent pre-equilibrium fission and transfer/breakup induced fission. At near barrier energies, for lower ground state spin, the entrance channel K (projection of J along the nuclear symmetry axis) distribution becomes narrower which may lead to an enhanced anisotropy compared to the SSPM prediction. On the other hand, a significant contribution from α and d/t induced fission with different K_0^2 and $< J^2 >$ may be responsible for the anomalous anisotropy of total fission. Similar conclusions can also be made on the existing data on FF angular distributions for ^{6,7}Li+^{232}Th systems measured by Freiesleben et al. [55]. However, there is no data available in the literature on the individual transfer or breakup induced fission channels and their contributions responsible for overall angular anisotropy of the total fission fragments for the above systems. In literature, there are limited number of studies available on transfer induced FFAD. In the study of transfer induced fission in ^{16}O + ^{232}Th system [34], Lestone *et al.* have observed a strong fission fragment angular correlation with respect to the recoil direction of the fissioning nuclei. However integration over all recoil angles results in a weak distribution relative to the beam direction. From the folding angle distributions of the fission fragments, Kailas *et al.* [35] have been able to separate the transfer induced fission and compound nucleus fission for ^{11}B+^{237}Np, ^{12}C+^{236}U and ^{16}O+^{232}Th systems. They concluded that at energies close to the Coulomb barrier, the transfer fission component is not significant enough to modify the anisotropy values obtained from the total FF angular distribution. Using the same technique Majumdar *et al.* [36] and Hinde *et al.* [37] have separated out the fission events following full momentum transfer for ^{19}F+^{232}Th and ^{16}O+^{238}U system respectively. Angular anisotropy values for CF-fission events were observed to be more compared to inclusive fission events at sub-barrier energies. Zhang *et al.* [56] observed anomalous increase in anisotropy at sub-barrier energy for ^{19}F+^{232}Th system and considered transfer induced fission as one of the possible reasons, however they found that contribution of transfer induced fission is not so significant ($\sim$10%) . But in case of a reaction involving ^{6}Li or ^{7}Li as projectile, due to their low breakup threshold, the contribution of tranfer/breakup induced fission could be significant as a direct manifestation of large suppression ($\sim$25-30%) of complete fusion [17, 22, 23].

To find the transfer or breakup effect, we have carried out investigation on FFAD for ^{6}Li+^{232}Th system as there is no data available for transfer induced FFAD. Hence, to identify these ICF fission channels and disentangle their individual contributions on total fission, exclusive measurements of fission fragments in coincidence with the complementary breakup fragments or light charged particles are essential.

To get a complete picture on the overall anisotropy due to transfer induced fissions, both the in-plane and out-of-plane anisotropies are in principle necessary. However, contradictory observations on the out-of-plane anisotropy have been reported for different systems [34, 57, 58]. While Dyer *et al.* [57] have observed a strong out of plane correlation compared to in-plane correlation for the system ^{86}Kr + ^{209}Bi, Lestone *et al.* [34] have observed nearly isotropic (anisotropy $\sim$ 0.8-1.1) out-of -plane correlation for ^{16}O+^{232}Th system. Similarly, Wolf *et al.* [58] have also observed a smaller value of the out-of-plane anisotropy ($\sim$ 1-1.5) compared to the in-plane anisotropy ($\sim$ 1.5-2) with respect to the angle of emission of PLF for ^{239}Pu(d,pf) reaction. In particular, when the PLFs are emitted in the backward angles, a nearly isotropic out-of-plane correlation has been observed for both ^{16}O+^{232}Th as well as d+^{239}Pu reactions. So, for beam energies near and below the Coulomb barrier, the probability of PLF emission in backward directions (grazing angles) being maximum, the out-of-plane correlation may be expected to be isotropic.

In the present work, the in-plane angular anisotropy for transfer/breakup induced fission for ^{6}Li+^{232}Th system has been measured exclusively at few energies around the Coulomb barrier to identify the possible transfer/breakup reaction channels leading to fission and to investigate the effect of these ICF fission processes on the total fission fragment angular anisotropy. The detector setup used for the present experiment allowed us to obtain the anisotropy only in the reaction plane.

4.1 Experiment and data analysis

The experiment was carried out using the ^{6}Li beam from BARC-TIFR Pelletron accelerator facility, Mumbai, at three bombarding energies of 28, 32 and 36 MeV. A self-supporting ^{232}Th foil of thickness $\sim$400 μg/cm^2 was used as a target. A schematic diagram of the experimental setup has been shown in Fig. 5.1. To detect the fission fragments, four silicon strip detectors (as described in chapter 2), $F_1 - F_4$, of size 50 mm $\times$ 50 mm each, covering a total angular range of $\sim$94°-172°, were placed on a fixed arm. The distance of the central strips of each detector from the target center was 176 mm. The gap between two adjacent fission detectors is $\sim$4°. A typical fission spectrum measured in coincidence with light charged particles by a single strip detector at $E_{\mathrm{beam}} = 36$ MeV is already shown in Fig. 2.5. It provides a good separation between light charged particles and fission fragments.

To measure the PLFs, three telescopes, $T_1 - T_3$, have been used. Each of these telescopes ($\Delta E - E$) is made of two silicon strip detectors of same size as mentioned earlier. The thicknesses of ΔE detectors are $\sim 50 - 60$ μm and that of E detectors are $\sim$ 1500 μm. One of the telescopes, T_1, with an angular coverage of $\sim$72°-88°, was mounted on the same (fixed) arm where fission detectors were mounted. Other two telescopes, T_2 and T_3, having a combined angular coverage of $\sim$36°, were placed on another arm which is rotatable and kept on the other side of the beam. These detectors were placed around the grazing angles to obtain good coincidence statistics while investigating the transfer/ breakup effect on inclusive FF angular distribution. They were also placed at non-grazing angles (i) to find out the dependence of FF angular anisotropy on the angle of PLF emission if any, and (ii) to measure the angular distributions of outgoing α, d and p.

Data was first recorded in singles mode to measure the inclusive fission fragment angular distribution and then in coincidence mode to measure the breakup/transfer induced fission angular distribution. For coincidence mode, the fission fragment detected in any of the Fission detectors (F_1 OR F_2 OR F_3 OR F_4) is recorded when there is a simultaneous light charged particle detected in any of the three telescopes (T_1 OR T_2

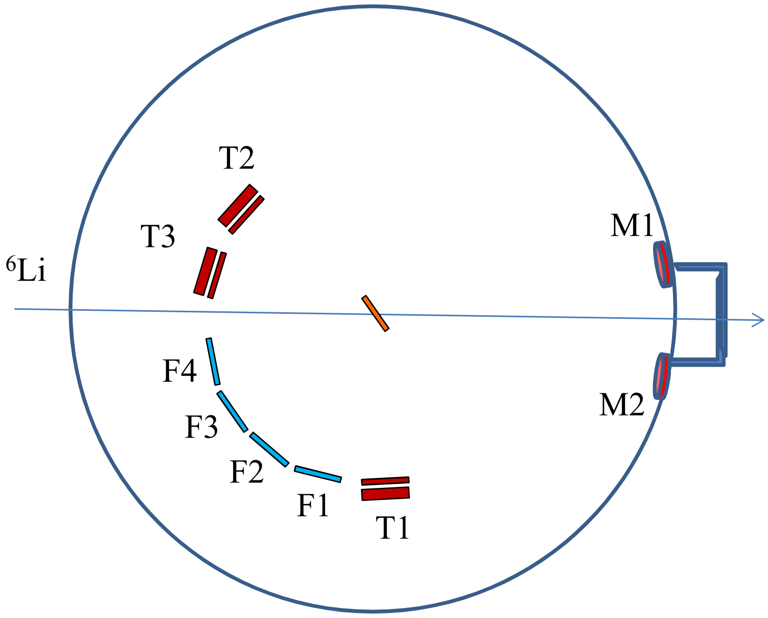

Figure 4.1: Schematic diagram of the experimental setup inside scattering chamber with four single silicon strip detectors ($F_1 - F_4$) to detect fission-fragments, three telescopes ($T_1 - T_3$) made of $\Delta E - E$ silicon strip detectors to detect light charged particles and two monitor detectors (M_1 and M_2).

OR T_3) to get the breakup/ transfer induced fission yield.

Typical two dimensional ($\Delta E - E_{\text{total}}$) spectrum for light charged particles (with atomic number Z=1,2 and 3) obtained from 16 strips of T_3 in coincidence mode was also shown in Fig. 2.4. E_{total} was obtained by adding the ΔE and E_{res} signals after gain matching and energy calibration.

4.2 Inclusive fission fragment angular distribution

Inclusive fission fragment angular distributions $W_{lab}(\theta_{\text{lab}})$ were obtained from the fission yields detected in the fission detectors in singles mode for three near barrier bombarding energies, E_{beam} = 28, 32 and 36 MeV. Yields from two adjacent strips of fission detectors have been combined together to improve the statistics. The measured distributions have been transformed to the center-of-mass system using the expressions as described in Appendix A

$$W_{\rm cm}(\theta_{\rm cm}) = W_{\rm lab}(\theta_{\rm lab}) \frac{1 + x\ cos(\theta_{\rm cm})}{(1 + 2x\ cos(\theta_{\rm cm}) + x^2)^{3/2}} \tag{4.1}$$

where, x is the ratio of center-of-mass velocity '$v_{\rm cm}$' to the velocity of fission fragments in center-of-mass frame 'v_f' (i.e., $x = \frac{v_{\rm cm}}{v_f}$). The value of '$v_f$' has been calculated from Viola's systematics for fragment kinetic energies [59]. The center-of-mass angle is calculated using the relation, $\theta_{\rm cm} = \theta_{\rm lab} + x\ sin\theta_{\rm lab}$. The inclusive FF angular distributions in center-of-mass frame thus obtained at $E_{\rm lab}$= 28, 32 and 36 MeV are shown as solid circles in Fig. 4.2(a), (b) and (c) respectively.

The angular distribution data in center-of-mass frame has been fitted using the expression $W(\theta) = a_0 + a_2\ cos^2\theta$. From the fitted curves, shown as solid lines in Fig. 4.2, the ratio '$W(180°)/W(90°)$' has been calculated to obtain the FF angular anisotropy of the respective angular distributions which are tabulated in Table 4.1. The above anisotropy values, shown by filled circles in Fig. 4.3, are found to be within the experimental errors of the existing data (hollow circles) measured by Freiesleben *et al.* [55]. However, the central anisotropy values for the present data are sightly higher than the ones from the literature. Anisotropy values from the present measurement as well as from Ref. [55] are in general found to be higher compared to the SSPM predictions as shown by a solid line in Fig. 4.3.

Table 4.1: Fission fragment angular anisotropy for total (inclusive) fission.

Energy (MeV)	Anisotropy (inclusive)
28	1.13 ± 0.04
32	1.16 ± 0.03
36	1.27 ± 0.02

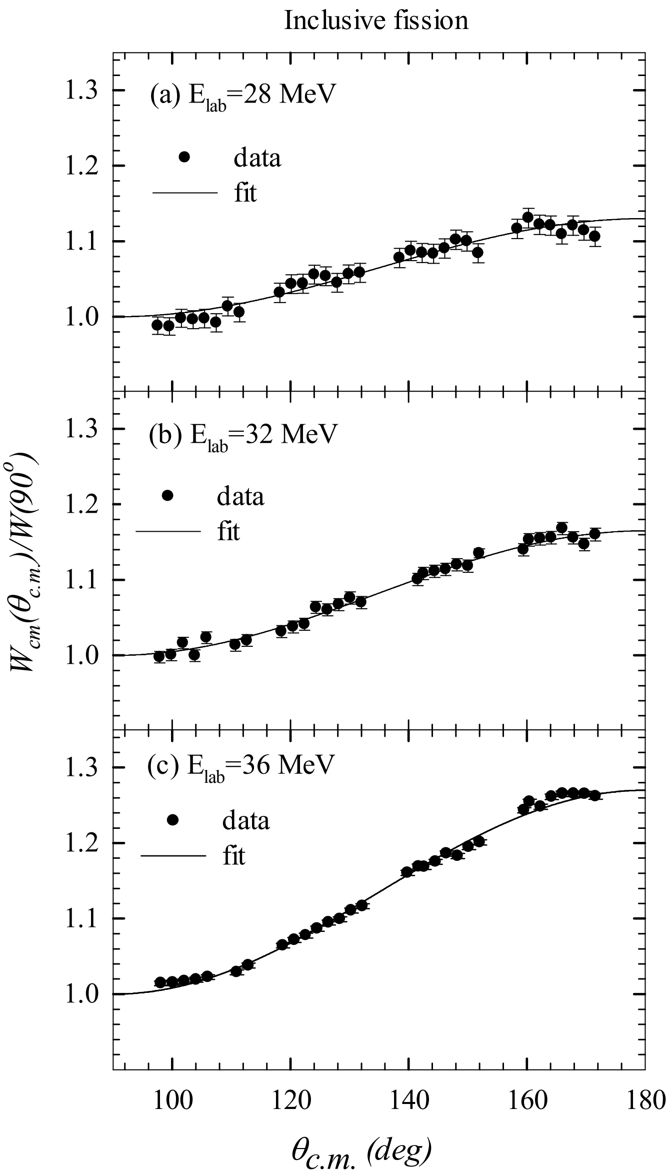

Figure 4.2: Inclusive (total) fission fragment angular distribution in ^{6}Li+^{232}Th reaction at beam energies of (a) 28 MeV, (b) 32 MeV, and (c) 36 MeV.

4.2.1 SSPM calculation

Based on SSPM formalism, the anisotropy A has been calculated as $A = 1 + \frac{<\ell^2>}{4K_0^2}$, where $< \ell^2 >$ was derived from the σ_ℓ versus ℓ distribution obtained from CCDEF code [60]. The input parameters of CCDEF are constrained by the fission excitation function available in the literature. The potential parameter with $DV = 40.0$, and target deformation parameters with $\beta_2(^{232}Th)$=0.22 and $\beta_4(^{232}Th) = 0.09$ [61] have been used. The variance of the K distributions is $K_0^2 = I_{eff}T/\hbar^2$. Here, I_{eff} is the effective moment of inertia and T $=\sqrt{(E^*/a)}$ is the saddle point temperature of the compound nucleus. The level density of the compound nucleus of mass A_{CN} is taken to be $a = A_{CN}/10\ MeV^{-1}$. The excitation energy E^* at the saddle point is given by $E^* = E_{c.m.} + Q - B_f - E_{rot} - E_n$, where Q is the Q value for the formation of the compound nucleus. The spin dependent fission barrier B_f, ground-state rotational energy E_{rot}, and effective moment of inertia I_{eff} are calculated using the Sierk model [62]. E_n is the average energy removed by the evaporated neutrons from the compound nucleus [63]. The average number of pre-scission neutron was found to be in the range of $0.65 - 1.68$ for the beam energy $24 - 40$ MeV.

4.3 Breakup or transfer induced fission fragment angular distributions

The anisotropy of the breakup induced fission fragments can be extracted using the measured yields of fission fragments in coincidence with projectile breakup fragments like α, deuteron and proton. In an incomplete fusion reaction, the composite nucleus formed by the capture of a breakup fragment and the complementary breakup fragment of the projectile start moving simultaneously at certain angles with respect to the beam direction. The recoil direction of the composite system will depend upon the angle and

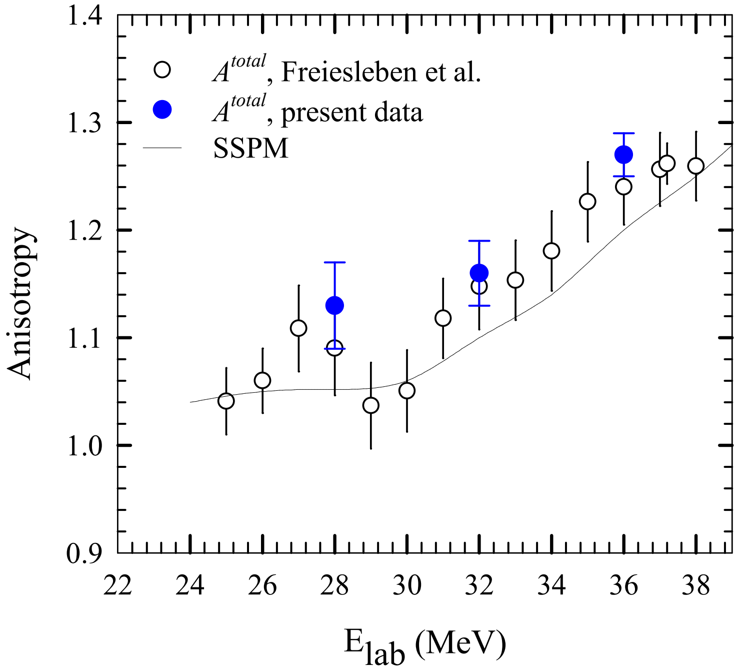

Figure 4.3: Fission fragment angular anisotropy for inclusive fission obtained from the present data (filled circle) and the existing data by Freiesleben et al. [55] (hollow circle) are compared with SSPM calculations (solid line) at near barrier energies.

momentum of the outgoing projectile like fragment (PLF). The direction of the recoiled composite nuclei and the corresponding angles of the fission fragments with respect to the recoil direction were calculated event by event to obtain the actual FF angular distributions with respect to an average recoil direction. To obtain the transfer/breakup induced FF angular distributions $Y'(\theta')$ in the rest frame of the recoiling nuclei, the following conversions have been used. Here θ' is the angle of fission fragments in the rest frame of recoiling nuclei which is calculated as,

$$\theta' = \theta'' + y\ sin(\theta'') \tag{4.2}$$

where θ'' is the angle in the laboratory frame between the direction of the fission fragment emission (θ_{fission}) and the direction of the recoil of the composite nucleus formed by the capture of the breakup fragment by the target (θ_{recoil}), i.e.,

$$\theta'' = \theta_{\text{fission}} - \theta_{\text{recoil}}, \tag{4.3}$$

and 'y' is equal to the ratio of recoil velocity of the residue nuclei 'v_{rec}' to the velocity of fission fragment 'v_f' i.e., $y = \frac{v_{rec}}{v_f}$.

In the rest frame of recoiling nuclei, the solid angle transformation for the FF angular distribution is given by

$$Y'(\theta') = Y''(\theta'') \frac{1 + y\ cos(\theta')}{(1 + 2y\ cos(\theta') + y^2)^{3/2}} \tag{4.4}$$

where, $Y''(\theta'')$ is the FF angular distribution in the laboratory frame with respect to recoil direction.

4.3.1 Fission in coincidence with α

The most dominating channel for the transfer/breakup induced fission was found to be the channel producing fission in coincidence with α. The breakup or transfer induced FF angular distribution $Y''(\theta'')$ has been obtained with respect to average recoil angle for two different situations corresponding to the detection of FF in coincidence with the α emitted (i) at forward angles and (ii) at backward angles. These two distributions will bring out any dependence of FF angular anisotropy on the angle of the α emission. To detect the α, the telescope 'T_3' was placed once at forward angle and then at backward angle covering the angular range of $72° - 88°$ and $154° - 170°$ respectively. To limit the range of recoil angles, the coincident counts of only 8 central strips of T_3 have been used for obtaining the FF angular distributions. The variation in the corresponding recoil angle of the composite nucleus was found to be within $\pm 3°$.

In the first case, the telescopes T_1 and T_3 were placed at symmetric positions on either side of the beam, in the angular range of $\pm(72° - 88°)$, to get the angular anisotropy with respect to forward moving alpha. For a typical beam energy of $E_{\text{beam}} =$ 36 MeV, when alpha is detected at T_3 which is placed on the left side of the beam, the recoil direction is on the right side of the beam, and the average recoil angle with respect to the beam direction is calculated to be $\theta_{\text{recoil}} \approx +35°$. Thus, with respect to the recoil direction, the FF angular distribution covers the angular range of $\theta'' \sim 59° - 138°$. Simultaneously, when alpha gets detected at T_1, which is placed on the right side of the beam, the recoil direction is on the left side of the beam direction with $\theta_{\text{recoil}} \approx -35°$ leading to the FF angular distribution range of $\theta'' \sim 129° - 208°$. Hence, using data of both T_1 and T_3, the FF angular distribution in the rest frame of recoiling nuclei could be measured in the angular range of $\theta'' \sim 59° - 208°$. Similarly, the angular distribution of fission fragments measured in coincidence with α for E_{beam} = 32 MeV was obtained. The resultant FF angular distribution after transformation to the rest frame of the recoil nuclei are shown as open circles in Fig. 4.4 for (a) 32 MeV and (b) 36 MeV. The measured FF angular distributions were fitted by the expression $Y'(\theta') = a_0 + a_2 cos^2\theta'$ (solid lines) to obtain the angular anisotropy at two energies. For E_{beam} = 28 MeV, the coincidence yield of outgoing alpha particles detected at the telescopes T_1 and T_3 are very less as they are placed at $72° - 88°$ which are far from the grazing angle ($\sim 180°$). So, the FF angular distribution was not obtained at this energy. The angular anisotropy obtained for 32 and 36 MeV are 1.16±0.04 and 1.17±0.03 respectively.

For the second case (backward moving α), i.e., when alpha gets detected by T_3 telescope placed in the angular range $154° - 170°$, the average recoil angle $\theta_{\text{recoil}} \approx +10°$. The fission yield in coincidence with alpha detected in T_3 telescope only has been used to obtain the FF angular distribution in the rest frame of recoiling nuclei which are shown as filled circles in Fig. 4.5. The measured FF angular distributions were fitted by the expression $Y'(\theta') = a_0 + a_2 cos^2\theta'$ (solid line) and angular anisotropy obtained for 28, 32 and 36 MeV respectively are 1.26±0.04, 1.16±0.04 and 1.23±0.03.

Comparing the above results, it was found that the FF anisotropy is same (within

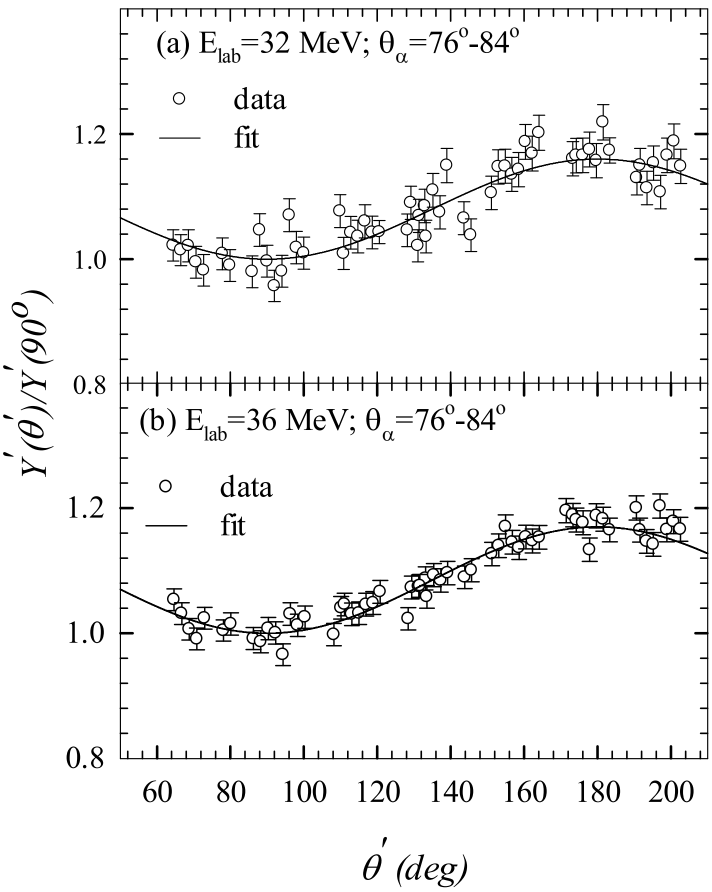

Figure 4.4: Angular distributions of α-gated fission fragments in the rest frame of the recoil nuclei for the beam energies of (a) 32 MeV and (b) 36 MeV when α is detected in the forward angles.

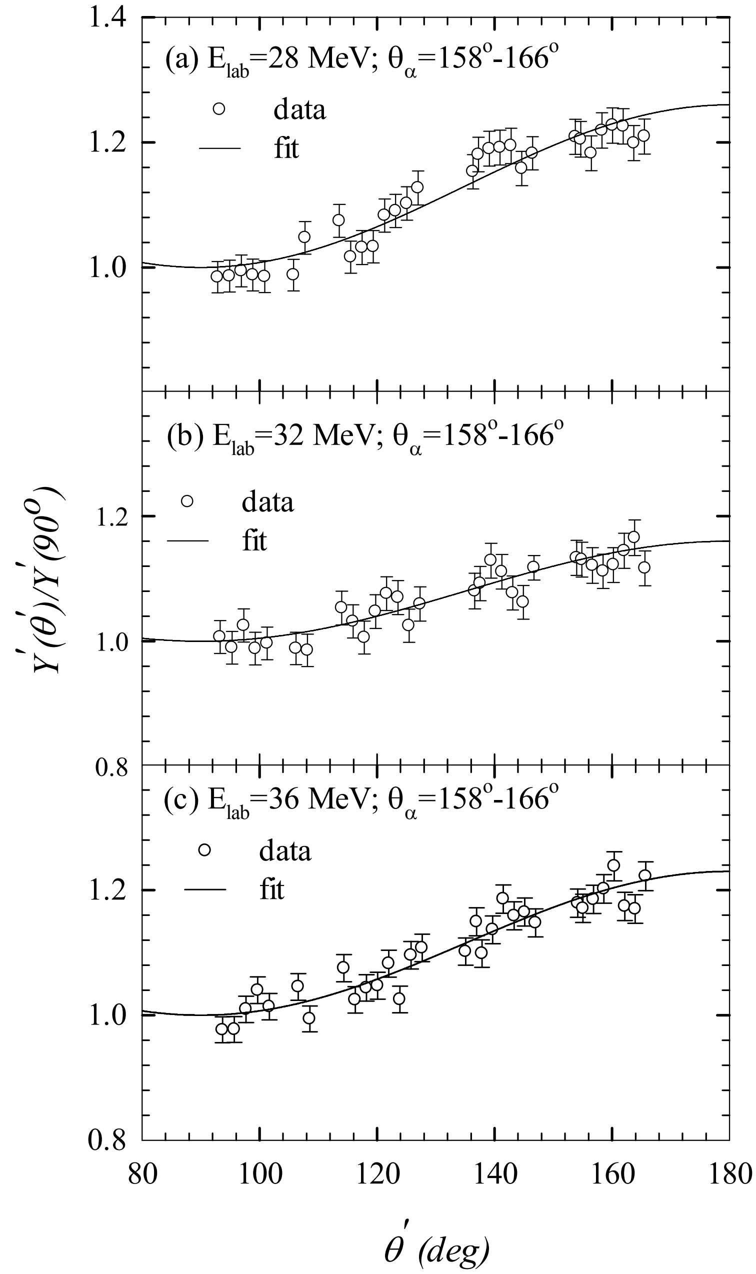

Figure 4.5: Angular distributions of α-gated fission fragments in the rest frame of the recoil nuclei for the beam energies of (a) 28 MeV, (b) 32 MeV and (c) 36 MeV when α is detected at the backward angles.

the experimental errors) for the two cases. Hence it can be assumed that the anisotropy is independent of the direction of the emission of the α, alternately, it is independent of the recoil direction of the residual fissioning nuclei. The average values of the anisotropy obtained from the two cases for α-gated fission fragments are found to be 1.26±.04, 1.16±.04 and 1.20±.04 for E_{beam} = 28, 32 and 36 MeV respectively. These values have been used in section 4.4.2 to obtain the overall contributions corresponding to all possible values of θ_{PLF}.

4.3.2 Fission in coincidence with deuteron and proton

Interestingly, there is a significant yield of fission fragments detected in the fission detectors in coincidence not only with deuterons but also with protons observed in telescopes T_1 and T_2. Similar to the previous subsection, the yield of fission fragments detected in fission detectors in coincidence with the deuterons and protons detected in the telescopes have been extracted. The statistics for deuteron and proton gated fission for E_{beam} = 28 MeV was poor. So, for remaining two beam energies, E_{beam} = 32 and 36 MeV, the angular distributions of the fission fragments in coincidence with deuterons and protons have been obtained in the frame of recoil nuclei and shown in Fig. 4.6 and Fig. **??** respectively. Using the fit by the expression $Y'(\theta') = a_0 + a_2 cos^2\theta'$, the FF angular anisotropy for deuteron and proton gated fissions have been obtained.

A comprehensive list of in-plane fission fragment angular anisotropy for breakup induced fissions gated with α, d and p in the rest frame of recoiling nuclei has been given in Table 4.2. It was interesting to observe that some of the anisotropy values, particularly for d-gated and p-gated fissions, in the rest frame of recoiling nuclei are stronger than those for the inclusive fission in centre-of-mass frame. While the in-plane anisotropy for α-gated fission is found to be higher at E_{beam} = 28 MeV, it is smaller at E_{beam} = 36 MeV with respect to the ones for inclusive fission at respective energies.

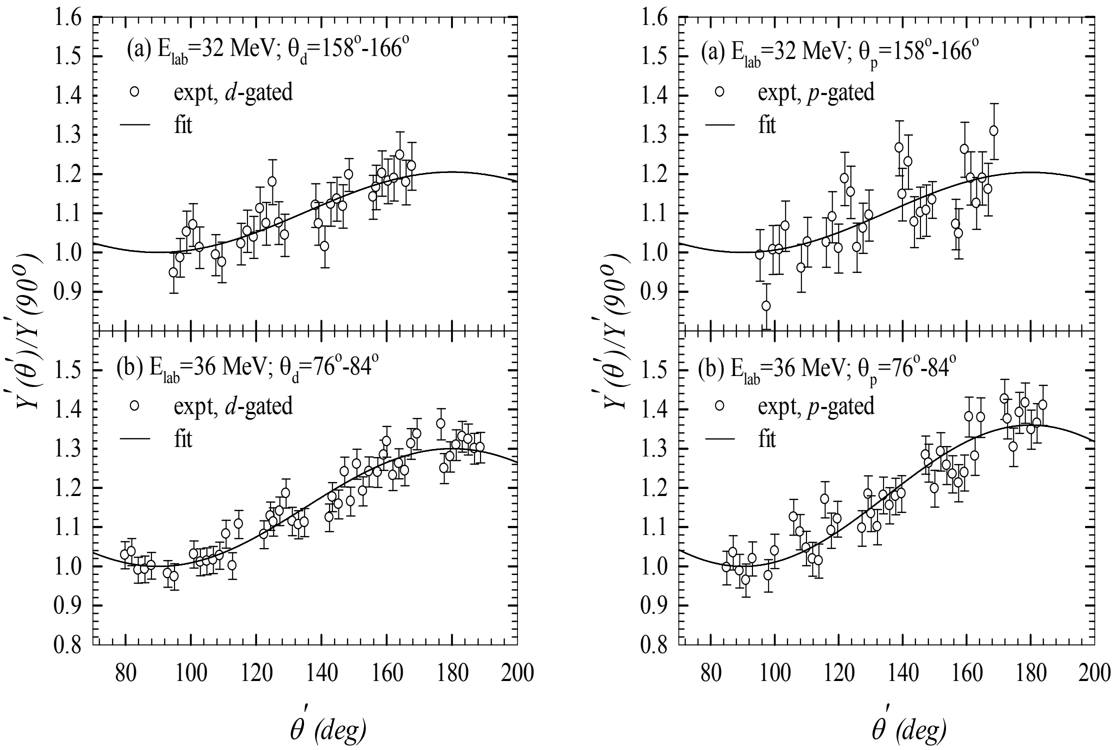

Figure 4.6: Angular distribution for fission fragments measured in $F_1 - F_4$ detectors in coincidence with deuterons (left) and protons (right) detected by the telescopes in the angular range of (a) $158^\circ - 166^\circ$ for $E_{\rm beam} = 32$ MeV and (b) $76^\circ - 84^\circ$ for $E_{\rm beam} = 36$ MeV .

Table 4.2: Fission fragment angular anisotropy (A) for breakup/transfer induced fissions gated with α, d and p in the frame of recoil nuclei.

Energy (MeV)	A (α-gated)	A (d-gated)	A (p-gated)
28	1.26 ± 0.04	-	-
32	1.16 ± 0.04	1.21 ± 0.09	1.20 ± 0.24
36	1.20 ± 0.04	1.30 ± 0.08	1.36 ± 0.08

However, these anisotropy values may not give the exact picture of how the overall anisotropy due to breakup/transfer induced fission affects the anisotropy of the inclusive total fission. Because, these FF angular distributions have been obtained in coincidence with light charged particles detected only in limited solid angles in a reaction plane. Secondly, the contribution to the overall anisotropy for total fission will depend on the individual probabilities of different breakup/transfer induced fission channels.

4.4 Effect of projectile breakup on inclusive fission

One of the motivations of the present work is to investigate the effect of projectile breakup, if any, on the FF angular anisotropy of inclusive fission. In order to obtain the overall anisotropy of the FF angular distribution correlated with the PLFs emitted in all solid angles, the knowledge of both in-plane and out-of-plane anisotropies is essential. However, as mentioned in the introduction and observed in Refs. [34, 58], for beam energies near and below the Coulomb barrier where grazing angles are in backward directions, the out-of-plane correlations between FFs and PLFs are expected to be isotropic. For the present measurements at low energies, especially at 28 and 32 MeV, the isotropic correlations may be assumed. In other words, the angular distribution with respect to the direction of the recoiling heavy nucleus is symmetric.

Thus, the overall effect of breakup induced fissions can be obtained by using their in-plane anisotropy only. It may be recollected that the present experimental setup is consisted of detectors for both FFs and PLFs placed in the same plane that provides the in-plane correlation.

The FF angular anisotropies of the breakup induced fission fragments measured in coincidence with α, deuteron and proton that are emitted in the same plane have already been extracted in the previous section. However, due to limited coverage of the light charged particle detectors, even in the reaction plane itself, the above anisotropy does not provide the correct representation of the effect of breakup on the inclusive fission fragment angular anisotropy. To study the overall effect, one needs to find out the contributions of breakup induced fissions corresponding to all possible laboratory angles (θ_{PLF}) of the outgoing complementary projectile breakup fragments emitted in the same plane in coincidence with fission fragments with proper weight factor $P(\theta_{\mathrm{PLF}})$. This weight factor is proportional to the differential cross sections of the outgoing projectile like fragments. For each angle of the light charged particles with an average momentum, there is a corresponding recoil angle (θ_{recoil}) of the composite nuclei formed by the capture of the complementary breakup fragments by the target nuclei.

To find the effect of breakup induced fission on the angular anisotropy of the total fission the following procedure has been followed. First, the experimental angular distribution of breakup induced fission fragments was obtained in the rest frame of recoiling nuclei. Second, the angular distributions $\mathrm{d}\sigma(\theta_{\mathrm{PLF}})/\mathrm{d}\Omega$ were obtained for the outgoing projectile breakup fragments like α, d and p to find the weight factors $P(\theta_{\mathrm{PLF}})$ mentioned above. Third, the overall angular distribution of breakup induced fission fragments was obtained by integrating the contributions corresponding to all possible angles of PLF emissions with weight factor $P(\theta_{\mathrm{PLF}})$.

4.4.1 Angular distributions of outgoing α, d and p

Inclusive yields for α, d and p have been extracted from the data recorded by the telescopes in singles mode. Angular distributions for α, d and p productions obtained from these yields are shown in Fig. 4.7. The cross sections for inclusive α produced in the present reaction at E_{beam} = 28, 32 and 36 MeV are shown in Fig. 4.7(a) as stars, open circles and filled circles respectively. Dashed lines represent the fits to the experimental data.

Similarly, the experimental differential cross sections for inclusive deuterons and protons produced in the present reaction have been shown in Fig. 4.7(b) and (c) respectively. The data for E_{beam} = 32 and 36 MeV have been represented by open and filled circles respectively. Dashed lines represent the fits to the data that are used to obtain the weight factor $P(\theta_{\mathrm{PLF}})$ at any angle θ_{PLF}. The cross sections of protons and deuterons at E_{beam} = 28 MeV have not been shown in the figure as statistics of the fission fragments detected in coincidence with d and p at these two beam energies were very poor.

4.4.2 Overall anisotropy for breakup induced fission

As mentioned earlier, the overall effect of breakup induced fission on inclusive fission fragment angular anisotropy can be found only when one considers all the fission events detected in coincidence with light charged particles emitted in all possible solid angles. However, for the case of isotropic emission of correlated PLFs and FFs in the out-of-plane, the in-plane anisotropy becomes important. In the present measurement, the grazing angles at E_{beam} = 28, 32 and 36 MeV, are $\sim 180^\circ$, 160° and 90° respectively,

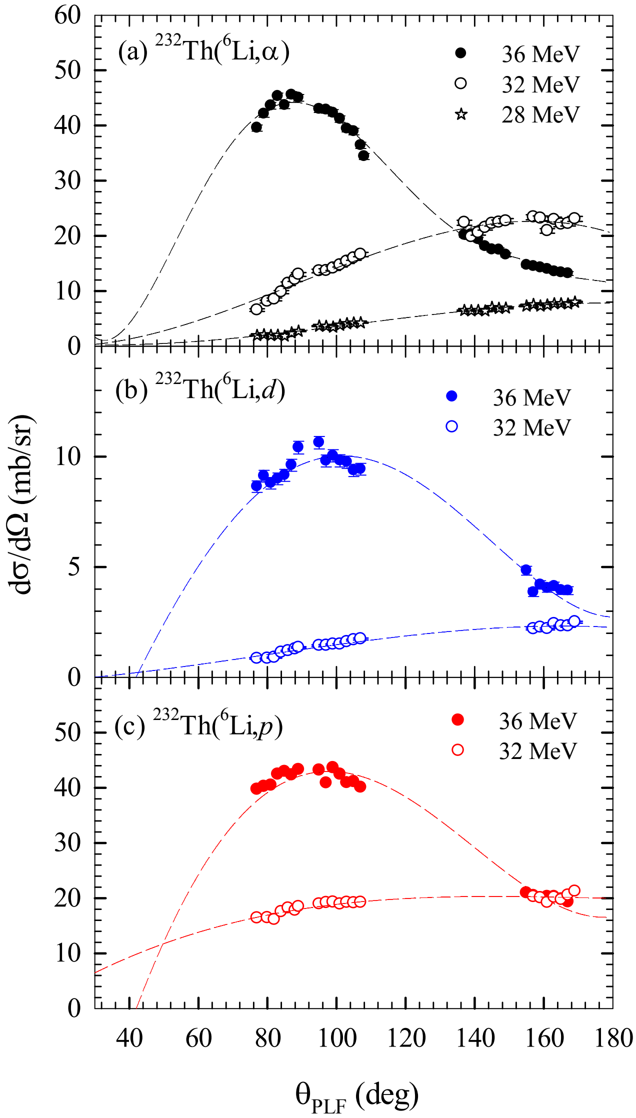

Figure 4.7: Differential cross sections for (a) inclusive α at E_{beam} = 28, 32 and 36 MeV, (b) inclusive deuteron at E_{beam} = 32 and 36 MeV, and (c) inclusive proton at E_{beam} = 32 and 36 MeV, produced in ^{6}Li+^{232}Th reaction.

which are not in forward angles. Similar to the one observed in Refs. [34, 58] for ^{16}O+^{232}Th and d+^{239}Pu reactions, one can expect that the out-of-plane distributions at lower energies for the present system with grazing angles in backward directions especially for 28 and 32 MeV are isotropic. In such cases, the in-plane anisotropy in transfer/breakup induced fissions plays an important role in modifying the inclusive FF angular anisotropy.

However, to account for all transfer events including those where the projectile-like fragment has not been observed, one has to realize that the directions of recoils, beam axis and a fission fragment will not generally be situated in the same plane. The recoils should be allowed to go out of plane, and one must then average over recoil directions out of plane, for given recoil angle with respect to the beam axis. As shown in the Appendix, this can be carried out applying spherical harmonics algebra and arriving at a very simple expression. The angular distribution of breakup/transfer fission in the frame of recoil nuclei has been assumed to be independent of the direction of recoil. The overall effect of breakup induced fission due to all possible recoil angles of both in- and out-of-planes can thus be inferred using the in-plane angular distribution only. As described in Appendix A, by averaging over all the recoil angles (θ_{recoil}) the angular distribution in the rest frame of recoil nuclei with respect to beam axis can be obtained as,

$$W(\theta_{\text{fission}}) = 1 + A_2 P_2(cos\theta_{\text{recoil}}) P_2(cos\theta_{\text{fission}}) \tag{4.5}$$

Here, the angular distribution coefficient has just been multiplied by a factor $P_2(cos\theta_{\text{recoil}})$ that accounts the contribution from all out-of-plane recoil angles. Once this extra factor is included, the effect of out-of-plane recoils is incorporated while considering the θ_{PLF}, θ_{recoil} and θ_{fission} to be in the same reaction plane.

To obtain the overall angular distribution following steps have been followed. First, the angular distribution of breakup/transfer induced fission in the frame of recoil nuclei obtained in the previous section was assumed to be independent of the direction of recoil. This is a valid assumption because the difference in the FF anisotropy corresponding to fission in coincidence with forward moving α and backward moving α was not significant compared to the experimental error as observed in Fig. 4.4 and Fig. 4.5. For the case of α-gated FF angular distribution in recoil frame, at $E_{\text{beam}} = 32$ and 36 MeV, the average shape of the two angular distributions was assumed to be independent of recoil direction. And for the other cases, the FF angular distributions measured in coincidence with the PLFs detected around the grazing angles were used as representative angular distribution for all the recoil directions.

Now, for a fixed θ_{recoil}, the above distribution of $W(\theta_{\text{fission}})$ in the rest frame of recoil nucleus can be converted into the distribution in lab frame ($Y_{\text{lab}}(\theta_{\text{lab}})$). These distributions were then multiplied by a corresponding weight factor $P(\theta_{\text{PLF}})$. Sum of these weighted angular distributions, i.e., $\Sigma_{\theta_{\text{PLF}}} Y_{\text{lab}}(\theta_{\text{lab}}) P(\theta_{\text{PLF}})$, is the overall breakup/transfer fission angular distribution in laboratory frame with respect to the beam axis corresponding to each of the outgoing channels at measured energies. These angular distributions were finally converted to the center-of-mass frame distribution $Y_{\text{cm}}(\theta_{\text{cm}})$, as shown in Fig. 4.8. The solid, dashed and dash-dot lines represent the estimated overall angular distributions corresponding to the fission fragments emitted in coincidence with p, d and α respectively.

The final anisotropy of the above overlapping distributions considering both in- and out-of-planes recoils obtained for alpha, deuteron and proton gated fission events at various energies have been tabulated in Table 4.3.

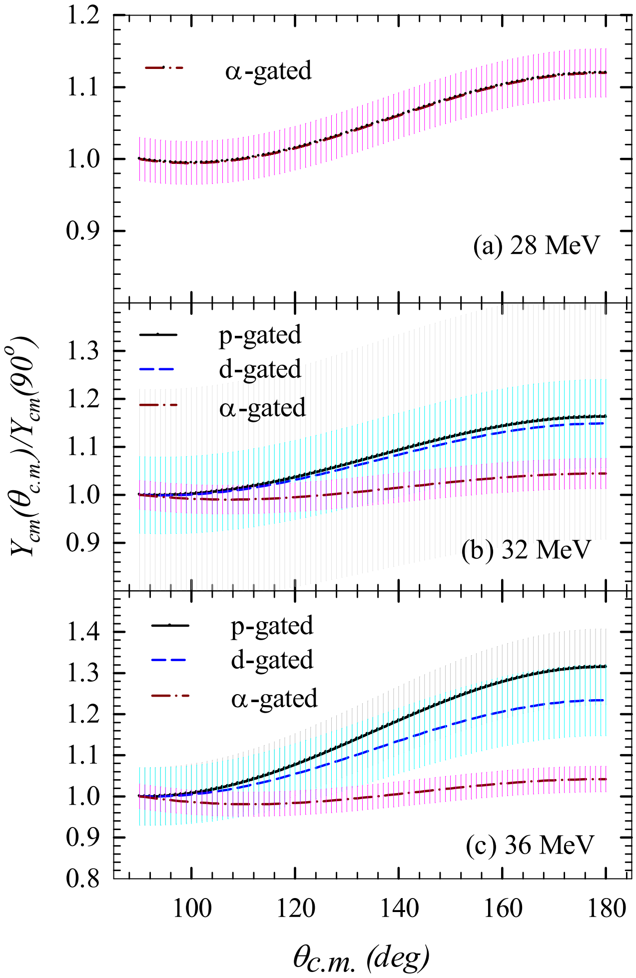

Figure 4.8: Estimated overall angular distributions of breakup/transfer induced fission fragments in coincidence with p, d and α emitted in all possible directions, with respect to the beam axis in center-of-mass frame.

Table 4.3: Overall fission fragment angular anisotropy A in center-of-mass frame due to breakup/transfer induced fissions gated with α, d and p emitted in- as well as out-of-plane compared to inclusive total fission.

Energy (MeV)	A (inclusive)	A (α-gated)	A (d-gated)	A (p-gated)
28	1.13 ± 0.04	1.19 ± 0.04	-	-
32	1.16 ± 0.03	1.12 ± 0.04	1.18 ± 0.09	1.19 ± 0.24
36	1.27 ± 0.02	1.19 ± 0.04	1.29 ± 0.08	1.35 ± 0.08

The estimated anisotropy of breakup induced fission in coincidence with both in- and out-of-plane α (the dominant channel) is less than or equal to the ones observed for the inclusive fission fragments. For d- and p-gated fission fragments, the angular anisotropy values are found to be slightly higher but within the experimental errors of inclusive fission. In the present measurements, since the dominant breakup induced fissions are the ones measured in coincidence with α particles, the overall in-plane anisotropy of the breakup/transfer fission will be less than or equal to the total anisotropy. Therefore, the anisotropy corresponding to pure CF fission could actually be more than the anisotropy observed for the total fission. This will further enhance the difference in the anisotropy between SSPM prediction and the ones for pure CF fission.

So it can be concluded that the observed enhancement in the anisotropy for total fission compared to the SSPM predictions at near barrier energies is not due to the contribution from breakup/transfer induced fissions. However, it may be emphasized that the above conclusion is true only when the out-of-plane correlation is isotropic.

Further measurements of fission fragments in coincidence with the PLFs emitted in all possible solid angles using both in-plane and out-of-plane detectors are necessary to confirm the above picture of the FF angular anisotropy corresponding to the breakup/transfer induced fission.

4.5 ECD K state model calculation

The enhancement of experimental FF angular anisotropy compared to SSPM predictions can be understood in terms of pre-equilibrium fission (PEF) model based on the Entrance Channel Dependent (ECD) K-state distribution [10, 64, 65]. If the input K distribution is not fully equilibrated, the PEF mechanism can lead to anomalous fission fragment anisotropies. For many reactions involving actinide targets the contribution from PEF along with compound nucleus fission have been observed, particularly at sub- and near barrier energies. In case of ^{10,11}B+^{232}Th [61], ^{10,11}B+^{237}Np [66] and ^{6,7}Li+^{235,238}U [13] systems the experimental anisotropy values have been explained by the ECD pre-equilibrium fission model with the incorporation of the effect of ground state spin of the target and projectile (S).

The PEF model calculations were performed for the present system to understand the measured anisotropy. Here, the K distribution has been modified to incorporate the entrance channel ground state spin of the target and projectile as given below.

$$F(J,K,K') = exp\left[\frac{-(K-K')^2}{2\sigma_K^2}\right] \times exp\left[\frac{-K^2}{2K_0^2}\right].$$

Where $K' = Jsin\omega \pm S$ and $\sigma_K = qJ\sqrt{Tt}$ with 't' being the Bohr Wheeler Fission time and 'q' being a constant obtained from the fit to the experimental data. 'T' is the temperature of the compound nucleus and K_0^2 is the variance of the K distribution. The entrance channel K-state population for a particular angular momentum value J and ω decides the fusion cross section $\sigma_{fus}(J,\omega)$ for the angular momentum value J at various target projectile orientations ω. Now the modified angular distribution is given by

$$W(\theta) \propto \Sigma_{J=0}^{Jmax}\Sigma_{M=-S}^{S}\Sigma_{\omega}\sigma_{fus}(J,\omega) \times \frac{\Sigma_{K=-J}^{J}(2J+1)|d_{M,K}^{J}(\theta)|^2 F(J,K,K')}{\Sigma_{K=-J}^{J}F(J,K,K')}$$

Here, $d_{M,K}^{J}(\theta)$ is the rotational wave function [67]. The orientation dependent partial cross-section $\sigma_{fus}(J,\omega)$ for the present system have been calculated using the coupled-channels code for fusion CCDEF [60]. Using the above expressions and including the g.s. spins of the projectile and target, the FF angular distributions i.e.,

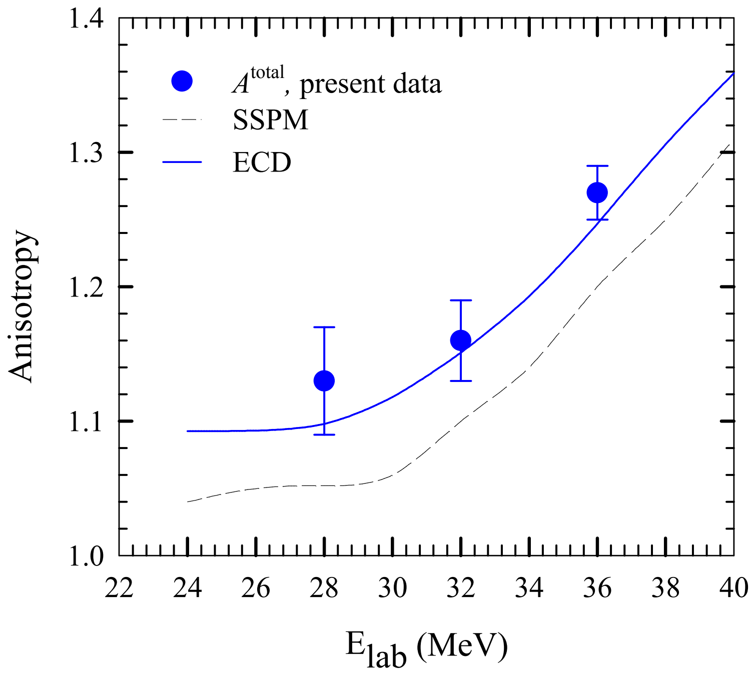

Figure 4.9: Fission fragment angular anisotropy for total fission obtained from present data (filled circle) are compared with the calculations using ECD K-state model (solid line) at near barrier energies.

$W(\theta)$ have been calculated at different energies. The results for corresponding FF angular anisotropy are shown in Fig. 4.9 as a solid line. The anisotropy values obtained from the ECD K-state distributions are larger than the SSPM values (dashed lines) and they reproduce the measured values reasonably well. The parameter 'q' has been adjusted to 0.12 (MeV x 10^{-21} s)$^{-1/2}$ (slightly smaller than the value used in Ref. [61] for ^{10,11}B+^{232}Th reactions) to reproduce the measured anisotropy data assuming the discrepancy between the SSPM anisotropy and experiment is totally due to pre-equilibrium fission. Hence, the PEF alone can explain the deviation in observed anisotropy for total fission from SSPM prediction.

4.6 Summary

Inclusive and exclusive FF angular distributions have been measured at three near barrier projectile energies i.e., 28, 32 and 36 MeV for ^{6}Li+^{232}Th system. The FF angular anisotropy obtained from the measured inclusive data were found to lie within the experimental errors of the existing values [55], though the central values of the present anisotropies are slightly higher. Inclusive FF angular distribution consists of both CF- and ICF-fission events. To disentangle the angular anisotropies of ICF fissions from CF fission the fission fragments were measured in coincidence with outgoing projectile breakup fragments like α, deuteron and proton in the reaction plane, and the corresponding FF angular anisotropies in the rest frame of the recoiling nuclei were obtained. The α-gated fission reaction was found to be the major ICF-induced fission channel. Interestingly, some of the anisotropies of transfer induced (e.g., p-gated and d-gated) fissions in the rest frame of recoiling nuclei were found to be stronger than the respective anisotropies for inclusive FFs in the center-of-mass frame.

The overall angular anisotropy for the exclusive fission events in coincidence with α particles emitted in all possible directions within and out-of-the reaction plane were estimated to be smaller than or equal to that of the inclusive fission for all three beam energies. The FF angular anisotropy corresponding to the deuteron-gated and proton-gated fission were found to be slightly more than the α-gated fission but they are within the experimental errors of the inclusive fission. Therefore, assuming isotropic out-of-plane angular correlations as observed in Refs. [34, 58], it may be concluded that the breakup induced fission channels are not contributing to the enhancement of total anisotropy compared to the theoretical SSPM predictions. However, further measurements using PLF detectors both in- as well as out-of the reaction plane are necessary to obtain an exact angular distribution of transfer/breakup induced fission and confirm the above conclusion.

The observed anisotropy for total fission at near barrier energies could be explained in terms of entrance channel dependent pre-equilibrium fission model, implying that the contribution from pre-equilibrium fission along with compound nucleus fission may be one of the reasons behind the enhanced anisotropy for total fission compared to the SSPM prediction.

Chapter 5

Fission fragment mass distributions and ICF cross-sections measurement in ^{6,7}Li+^{238}U reactions

In the last chapter, we have attempted to find the effect of breakup or transfer channel on inclusive fission fragments angular distributions. We found that, though the FF angular anisotropies of individual transfer fission channels are higher than that of total fission, the overall anisotropy that includes the fission events with all possible directions of projectilelike fragments for any particular transfer channel is found to be smaller than total fission. In this chapter, we attempt to find out the transfer or breakup effect on fission fragment mass distributions. As mentioned in Chapter 1, there are certain observations available in literature which indicate that breakup or transfer induced fission may play a key role in modifying the inclusive FF folding angle distributions and mass distributions [15, 16]. Hence it is desirable to confirm the above observations directly by carrying out exclusive measurements on FF mass and folding angle distributions corresponding to individual transfer or breakup induced fission channels and disentangle their contributions, if possible.

On the other hand, so far very few experiments on FFMD measurement following transfer reactions have been carried out. For example, the FF mass distributions of two compound nuclei ^{227,228}Ac formed by transfer reactions have been obtained for the first time by Koneckny *et al.* [38], where they have extracted the mass distributions from ^{226}Ra(^{3}He,df) and ^{226}Ra(^{3}He,pf) reactions respectively. Using ^{239}Pu(d, pf) transfer fission, Nishio *et al.* [39] have studied the mass distributions of the ^{240}Pu composite nucleus via the super deformed β vibrational resonance. Hulet *et al.* [40] have studied the spontaneous fission of ^{259}Fm from its isomeric state with a half life of 1.5 s, which was produced in ^{257}Fm(t, pf) reaction. Again, the study of FFMD from nuclei populated by multi-nucleon transfer channels is of great interest as many of the fissioning nuclei can not be populated otherwise (using stable target and stable projectile).Recently the FF mass distributions of several neutron rich isotopes of Th, Pa and U, populated by the multi-nucleon transfer channels in the ^{18}O + ^{232}Th reaction have been studied by Leguillon *et al.* [32]. Similarly, Role of multichance fission at higher excitation energies have been demonstrated by Hirose *et al.* [30] in order to explain the FF mass distributions of nuclei populated in multinucleon transfer reactions on ^{18}O + ^{238}U system. Fission experiments taking advantage of transfer or incomplete fusion reactions are performed not only in direct kinematics, but also in inverse kinematics [68, 69, 70].

Here, we present new results on the FF mass and folding angle distributions for transfer or breakup induced fission for ^{6,7}Li+^{238}U systems measured exclusively at a few energies around the Coulomb barrier. The possible reasons for the unusual behaviors in FF mass and folding angle distributions for the above systems observed previously have been investigated. In addition, the mass-distributions of fission-ing nuclei ^{241,242,243,244}Pu and ^{240,241}Np populated in multi-nucleon transfer/ ICF reactions have been studied, where the mass-distributions of ^{244}Pu nuclei, formed by capture of ^{6}He by ^{238}U target have been studied in the excitation energy range complementary to that of Ref [30].

5.1 Experiment and data analysis

The experiment on ^{6,7}Li + ^{238}U reactions was carried out at 15-UD Pelletron facility in Inter University Accelerator Centre, New Delhi. Three beam energies of 30, 34 and 40 MeV were used for ^{6}Li and two beam energies of 31.4 and 41.4 MeV for ^{7}Li. The ^{238}U target of thickness $\sim$ 100 μg/cm^2 was sandwiched between two layers of ^{12}C of thickness $\sim$ 15 μg/cm^2 each. Two position sensitive multi-wire proportional counter (MWPC) detectors [71] were used to detect fission fragments. They were placed on two rotatable arms and kept on either side of the beam direction making a folding angle of $\sim 172^\circ - 175^\circ$ relative to the position of one of the MWPC. For example, when one of the detectors is kept at 35° (65°), the folding angle is 175° (172°). A schematic diagram of the experimental set up has been shown in Fig. 5.1. Each MWPC detector has an active area of 16×11 cm^2. The central distances of MWPC1 and MWPC2 from the target centre were 39.5 cm and 33.5 cm respectively. Each MWPC detector provides position information (horizontal and vertical) and a timing signal (STOP signal) for the time of flight measurement. The start of the timing signals were taken from two transmission type gas detectors of active area 3.7 × 3.7 cm^2 (S1 and S2) placed in front of the two MWPC detectors at a distance of 11 cm from the target centre. The position signals were calibrated using the known dimensions of the active areas of the MWPC detectors and the overall 2D plots of X and Y positions. The timing signals were calibrated using a "Dual pulsar" which generates two signals simultaneously, one of them is fed as the START signal and the other is fed as the STOP signal after delaying it suitably (in ns). The time offset (δt) has been determined from the velocities of alpha particles from a standard source. Using the above calibrations for position and

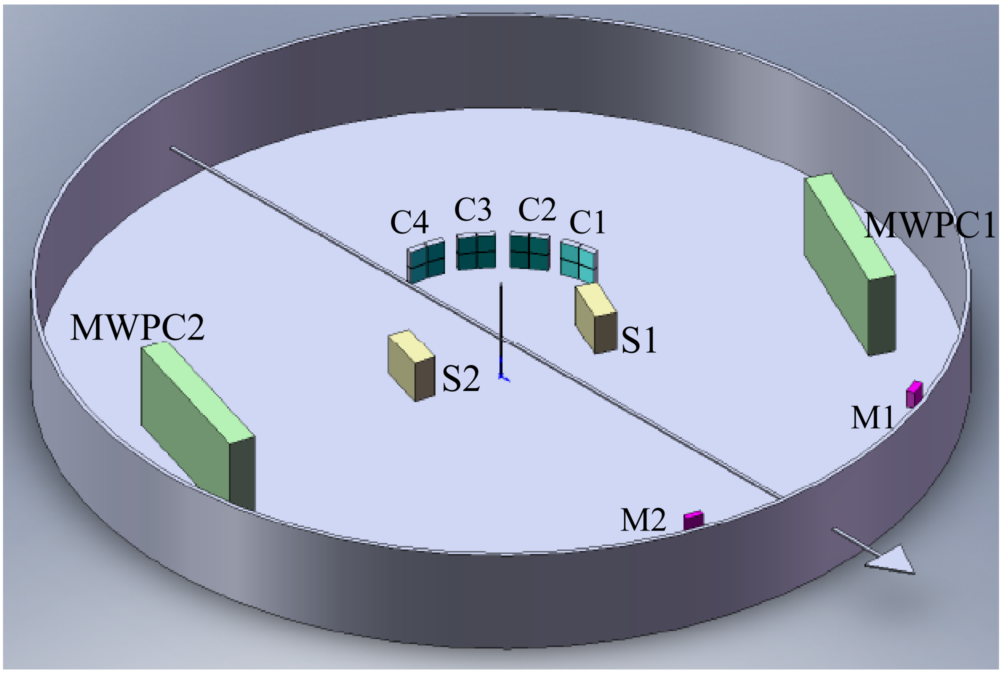

Figure 5.1: Schematic diagram of the experimental setup inside scattering chamber consisting of two MWPC detectors (MWPC1 and MWPC2) to detect fission-fragments, two transmission type START detector (S_1 and S_2), four CsI(Tl) detectors (C_1-C_4) with 4×4 crystals to detect light charged particles and two monitor detectors of Si surface barrier type (M_1 and M_2).

time, the values of scattering angle (θ), azimuthal angle(ϕ) and the velocity (v) of the fission fragments in the laboratory frame were obtained on event-by-event basis. Energy loss in the start detector has been calculated using the semi-empirical formula given in Ref. [72] and the change in velocity due to the energy-loss has been corrected for each event iteratively until the correct mass of the fission fragment is determined.

Four CsI(Tl) detectors having 4 crystals each [73] were used to detect projectile like fragments (PLF) covering the angular range of 101-168° for beam energies of 30, 31.4 and 34 MeV and 71-138° for beam energies of 40 and 41.4 MeV. The energy spectra of these detectors were calibrated using the known energies of α from a standard ^{229}Th source. A typical 'PID (particle identification) vs. Energy' spectrum obtained from one of the CsI(Tl) detector for ^{6}Li+^{238}U reaction at a beam energy of 40 MeV, has been

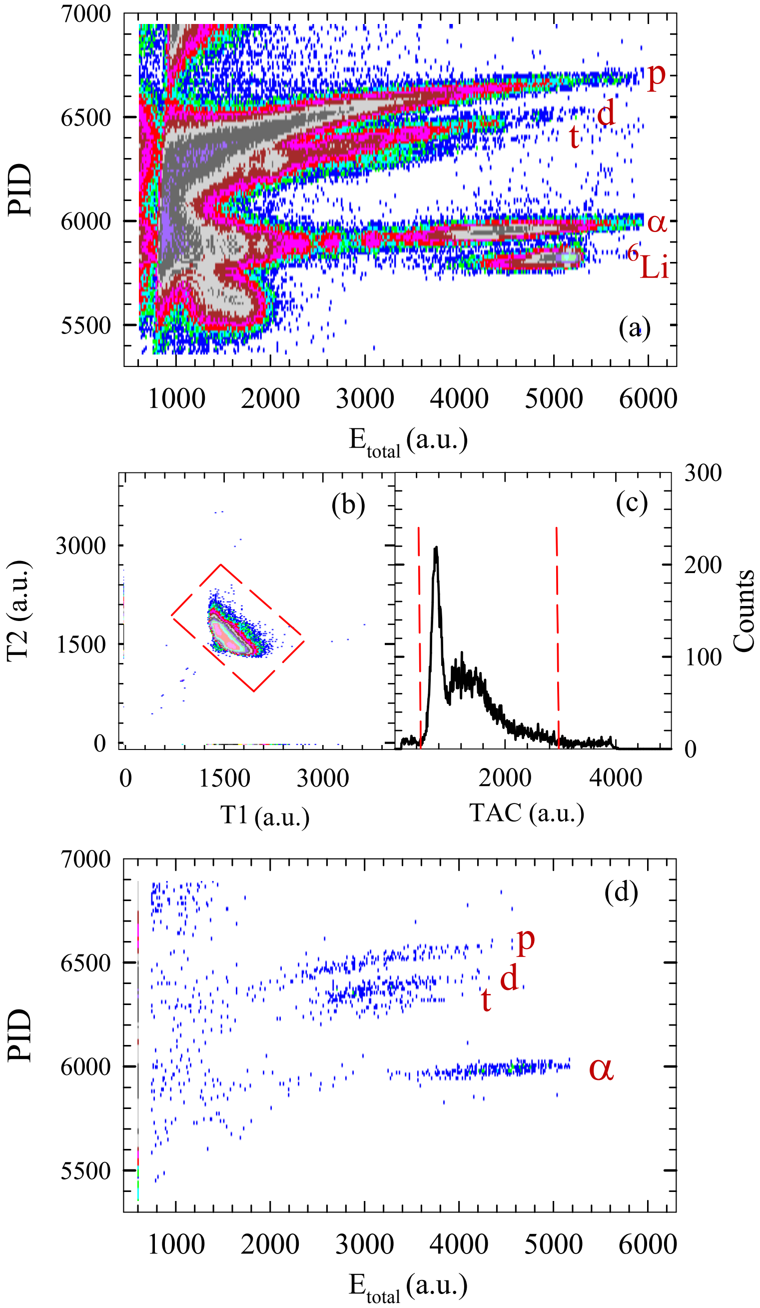

Figure 5.2: Typical spectra involving 40 MeV ^{6}Li beam correspond to (a) PID (particle identification) vs. Energy spectrum obtained from one of the CsI(Tl) detectors, (b) 2-D plot for the timings of two MWPC detectors, T1 vs T2, (c) TAC spectrum between MWPC detectors and CsI(Tl) detectors, and (d) the PID vs energy spectrum gated with the TAC and the banana gate in the 2D plot of MWPC timings as shown in spectra (b).

shown in Fig. 5.2(a). The correlation between the time-of-flight signals, 'T1 vs T2' obtained from two MWPC detectors has been shown in Fig. 5.2(b) which shows a clean spectrum of correlated fission events. Figure 5.2(c) shows the TAC spectrum between fission fragments and the PLFs. The 'PID vs. Energy' spectrum of Fig. 5.2(a) has been gated with the above fission timing distributions (within red contour) and the TAC spectrum, and the resultant 2D spectrum is shown in Fig. 5.2(d). It provides clear distinction between proton, deuteron, triton and α bands.

5.2 Fission fragment folding angle distributions

Typical FF folding angle distributions for total fission in laboratory frame for ^{7}Li+^{238}U reaction are shown in Fig. 5.3 for beam energies of (a) 31.4 MeV and (b) 41.4 MeV. Similar to our earlier observation in Ref. [16], a kink at $\sim$168° can be seen along with the main peak at $\sim$172° for 31.4 MeV, whereas, the distribution is symmetric around $\sim$175° for 41.4 MeV. As explained earlier, the shoulder structure in the FF folding angle distributions at 31.4 MeV is possibly due to the presence of ICF fissions along with the CF fission. The present data for the FF folding angle distributions obtained from exclusive measurements of transfer or breakup induced fission channels indeed confirm the above reasoning. The FF folding angle distributions in laboratory frame measured in coincidence with α, t and p detected in CsI detector array ($C_1 - C_4$) for ^{7}Li+^{238}U reaction have been shown in Fig. 5.3(c,d), (e,f) and (g,h) respectively for beam energies of 31.4 MeV (left panels) and 41.4 MeV (right panels). The peaks in the folding angle distributions of the fission fragments in coincidence with α, t and p, have been observed at $\sim$168°, 170° and 172° respectively (marked by dotted lines) for 31.4 MeV, consistent with the kinematics (indicated by up-arrows). The momentum transfer to the target is the highest in case of α emission at backward angles (grazing angle) for 31.4 MeV, leading to smaller folding angle for α gated fission compared to p or t gated fissions. The α and t gated fissions, being the most dominant transfer or ICF channels, are mainly responsible for the presence of the kinks in inclusive FF folding angle distributions at sub-barrier energies. On the other hand, for 41.4 MeV beam energy, the grazing angle being $\sim 90°$, the mean momentum transfers to the composite nuclei (when proton, triton and α are PLFs) are similar to that of a CF process which leads to a single peak in inclusive FF folding angle distribution.

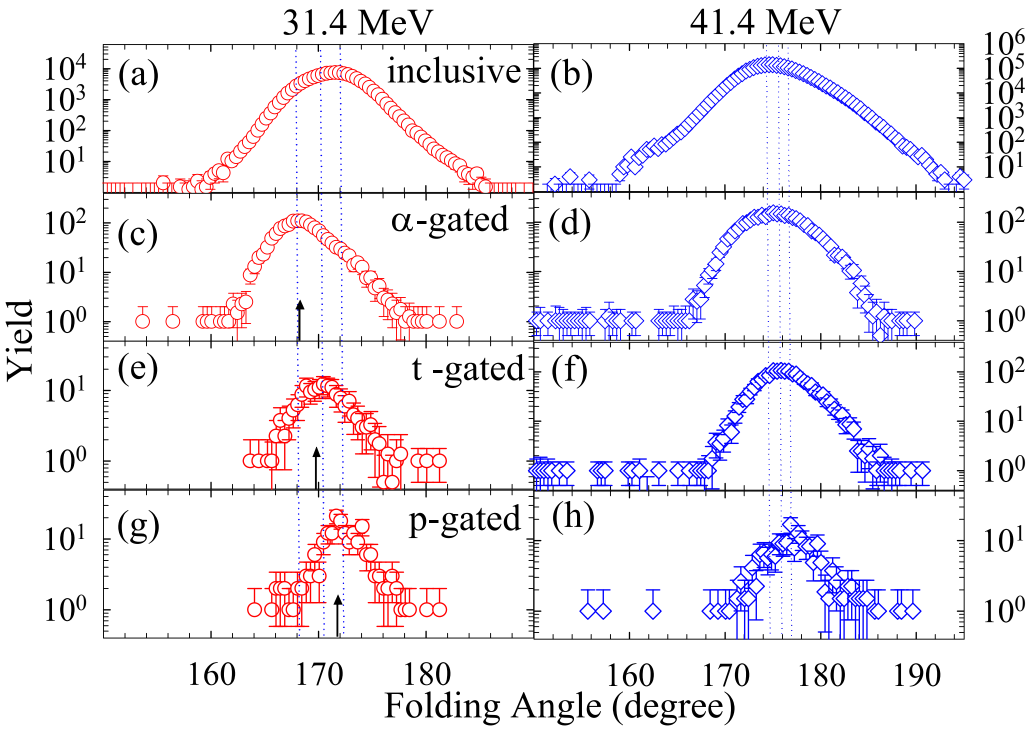

Figure 5.3: Typical folding angle distributions for (a,b) inclusive fission and (c,d) in coincidence with α, (e,f) triton and (g,h) proton in $^{7}Li+^{238}U$ reactions at beam energies of 31.4 MeV (left panels) and 41.4 MeV (right panels). Peak positions for α, triton and proton-gated fissions have been shown by dotted lines. The up-arrows in the left panels indicate the positions of the folding angles calculated from kinematics.

5.3 Fission fragment mass distributions

First, the mass distributions for the inclusive fission events were obtained by assuming all the events to be due to CF-fission. If the fragments of masses m_1 and m_2 move in the direction of θ_1 and θ_2 with respect to the beam axis with velocity v_1 and v_2 respectively, applying momentum conservation equation along the beam direction, one can obtain the required equation for fragment masses, as

$$m_1 v_1 \cos\theta_1 + m_2 v_2 \cos\theta_2 = P_{beam} \tag{5.1}$$

where $m_1 + m_2 = m_{CN}$, the compound nucleus mass, and P_{beam} = momentum of the incident projectile. Mass distributions thus obtained for inclusive fission in ^{6}Li+^{238}U and ^{7}Li +^{238}U reactions have been shown in Fig. 5.4 (a-c) and Fig. 5.5 (a,b) respectively. In both the reactions the double humped mass distributions are observed.

The peak to valley ratios for the above inclusive mass distributions have been extracted and found to be in good agreement with our earlier measurements [16]. Here the excitation energy has been calculated using the expression $E^* = E_{cm} + Q$, with the notations having their usual meanings. As shown in Fig. 5.6 by red filled circles, the P:V ratio increases with the decreasing excitation energy of the compound nucleus. This is understood in terms of increasing shell effect at lower excitation energies that causes the system to go through asymmetric mass division producing a larger P:V ratio. With the increase in excitation energy, the shell effect gradually washes out making the mass distribution more symmetric, reducing the P:V ratio.

Mass distributions for pure CF-fission events have also been obtained by selecting the central region of the plot of parallel versus perpendicular components of the velocity of the composite nuclei with respect to the velocity of compound nuclei ($\frac{v_{\parallel}}{v_{cn}}$ vs. $\frac{v_{\perp}}{v_{cn}}$). As expected [16], the P:V ratio for CF-fission, shown as red hollow circles in Fig. 5.6,

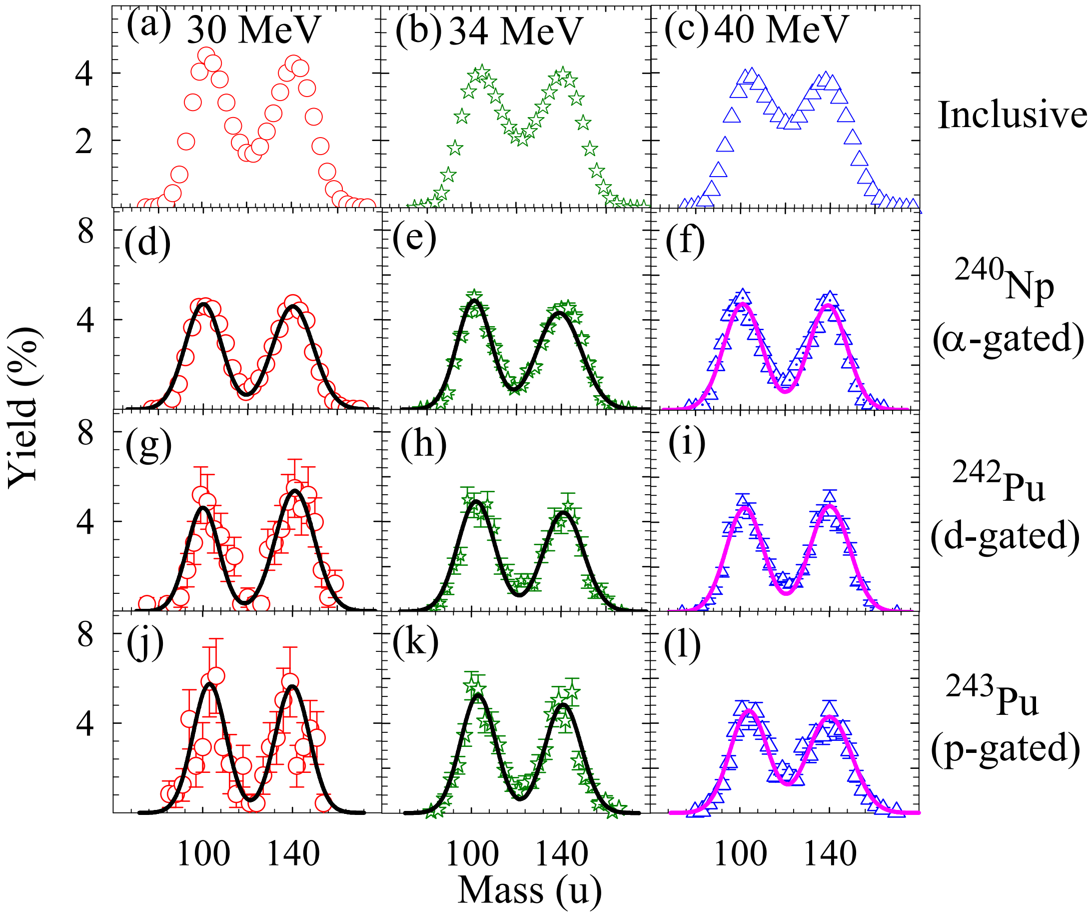

Figure 5.4: Mass distribution obtained in ^{6}Li+^{238}U reactions for (a-c) inclusive fission, (d-f) fission in coincidence with α, (g-i) fission in coincidence with deuteron and (j-l) fission in coincidence with proton, corresponding to beam energies of 30 MeV (left), 34 MeV (middle) and 40 MeV (right). A fit to each of the experimental data by two Gaussians is represented by a solid line.

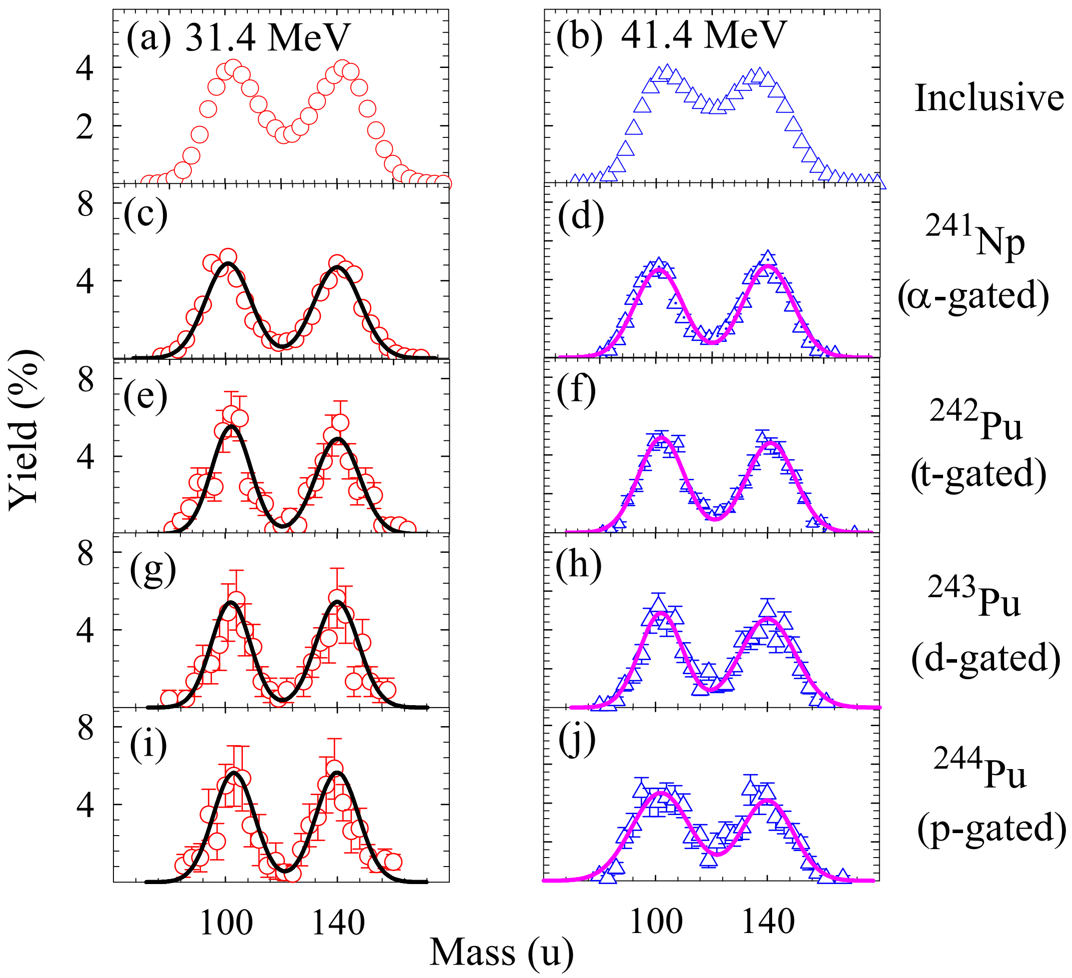

Figure 5.5: Mass distribution obtained in ^{7}Li $+^{238}$U reactions for (a,b) inclusive fission, (c,d) fission in coincidence with α, (e,f) fission in coincidence with triton, (g,h) fission in coincidence with deuteron and (i,j) fission in coincidence with proton for beam energies corresponding to 31.4 MeV (left panel) and 41.4 MeV (right panel). A fit to each of the experimental data by two Gaussians is represented by a solid line.

are less than the P:V ratio for inclusive fission (red filled circles). The contamination of ICF-fission with CF-fission is believed to be the main reason for generating the above discrepancy. So, in order to find the contributions from the non-compound fission channels, the mass distributions for individual ICF- or transfer-fission channels (prime motivation of the present work) have been derived separately as follows.

The mass distribution of the fission fragments detected in coincidence with a projectile breakup fragment (say x) emitted in the angle of θ_x with respect to the beam axis is obtained from the following equation,

$$m_1 v_1 \cos\theta_1 + m_2 v_2 \cos\theta_2 + m_x v_x \cos\theta_x = P_{beam} \tag{5.2}$$

where $m_1 + m_2 = m_{CN} - m_x$.

In case of ^{6}Li+^{238}U reaction, the fission fragments measured in coincidence with α, t, d and p are assumed to have been produced from the fission of composite nuclei ^{240}Np, ^{241}Pu, ^{242}Pu and ^{243}Pu, formed by the capture of the complementary breakup fragments, i.e., d, ^{3}He, α and ^{5}He respectively. Similarly, for ^{7}Li+^{238}U reaction, the fission fragments measured in coincidence with α, t, d and p are assumed to have been produced from the composite nuclei ^{241}Np, ^{242}Pu, ^{243}Pu and ^{244}Pu, formed by the capture of the complementary PLF clusters, i.e., t, α, ^{5}He and ^{6}He respectively. However, in case of proton-gated fission for ^{6}Li(^{7}Li)+^{238}U reaction the complementary breakup fragment is ^{5}He(^{6}He) which is unstable against $n(2n) + \alpha$ breakup and hence only one of the breakup fragments i.e., α or $n(2n)$ may induce fission. But, the probability of these multi-step processes could be considered to be negligible compared to the direct ^{5}He(^{6}He) induced fissions. It may be interesting to note that the mass distributions of fission fragments produced from the composite nuclei ^{244}Pu, formed by the capture of ^{6}He by ^{238}U target with excitation energy in the range of 15-22 MeV, have been measured for the first time in the present work.

In order to validate the above procedure, the present mass distributions for ^{240,241}Np and ^{241,242,243,244}Pu nuclei (red filled circles) have been compared with the literature data (hollow blue circles) for the same fissioning nuclei at comparable excitation energies as shown in Fig. 5.7. It may be pointed out that the mass resolution achieved in the present experiment is $\sim$ 4-5 u. It was also observed that the centre of gravities of heavy and light fragments are around 140-142u and 100-103u respectively, consistent with the observation by Leguillon et al. [32] and Hirose *et al.* [30].

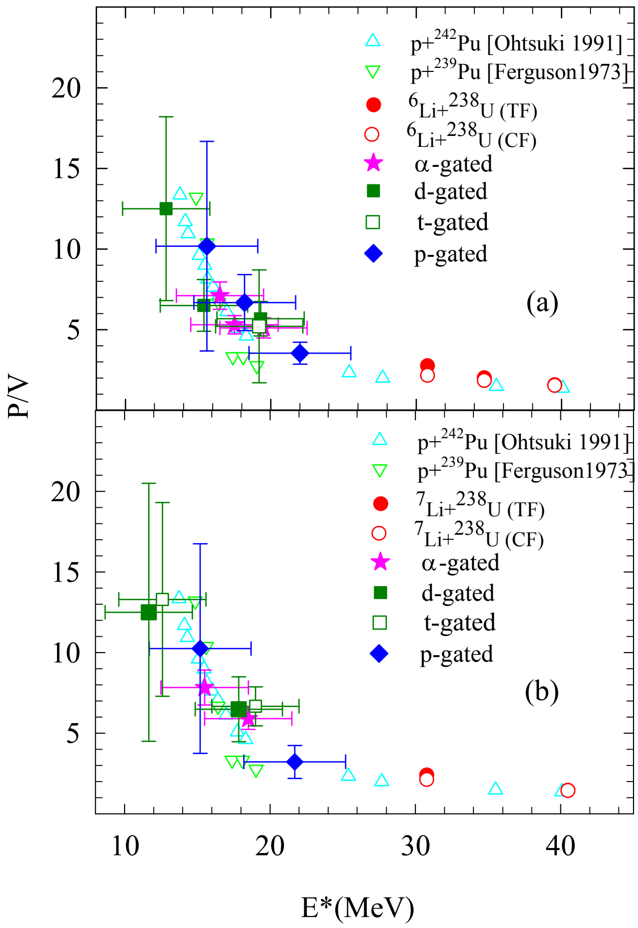

Figure 5.6: Peak to valley (P:V) ratio for total fission (filled red circle), CF-fission (hollow red circles), alpha-gated fission (filled pink stars), triton-gated fission (filled green squares), deuteron-gated fission (hollow green squares) and p-gated fission (filled blue diamonds) in reactions involving (a) ^{6}Li and (b) ^{7}Li projectiles.

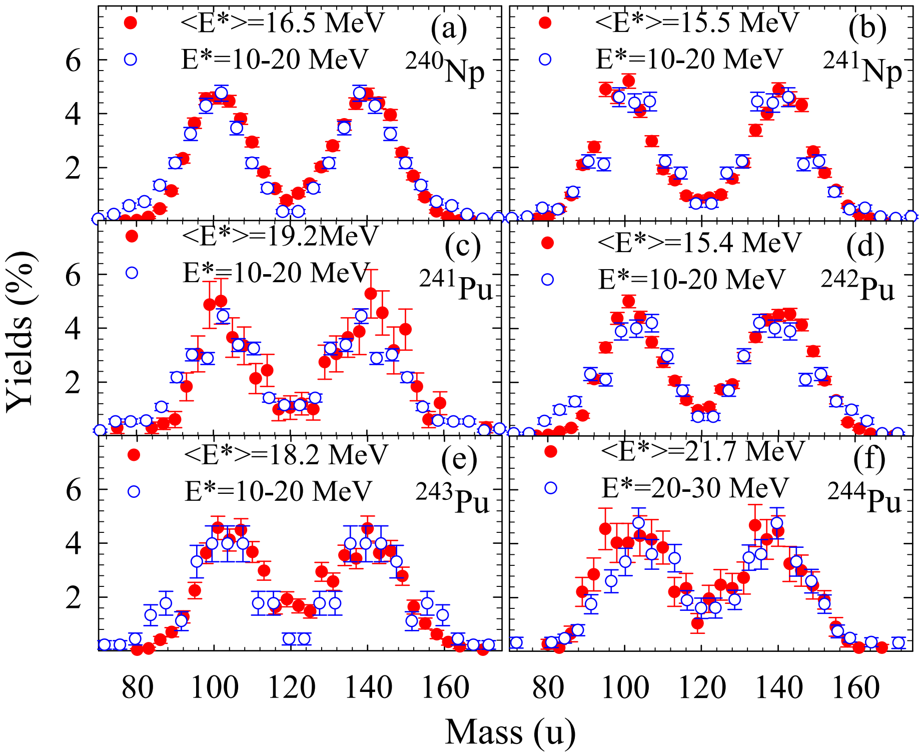

Figure 5.7: Comparison of the experimental mass distribution (red filled circles) for ^{240,241}Np and ^{241,242,243,244}Pu nuclei with the literature data (blue hollow circle) [30].

Now, the mass distributions of the fission fragments emitted in coincidence with α (the dominant PLF) have been obtained as shown in Fig. 5.4 (d-f) and Fig. 5.5 (c,d) for reactions involving ^{6}Li and ^{7}Li projectiles respectively corresponding to all the beam energies. It can be observed that, for a particular beam energy, the above distributions have more asymmetric mass components compared to those for total fission.

Similarly, the mass distributions obtained for fission in coincidence with d and p for ^{6}Li beam are shown in Fig. 5.4(g-i) and (j-l) respectively. Due to poor statistics for t-gated fissions involving ^{6}Li beam at lower energies, mass distribution has been obtained only at 40 MeV (Fig. 5.7(c)). For ^{7}Li beam, the mass distributions for fission in coincidence with t, d and p are shown in Figs. 5.5 (e,f), (g,h) and (i,j) respectively. Each of these mass distributions has been fitted with two Gaussians, and the P:V ratio has been determined from the ratio of the average of the two peaks to the valley of the fits. The corresponding excitation energies of the composite nuclei have been calculated as $E^{*} = E_{\text{beam}} - E_{\text{PLF}} - E_{\text{recoil}} + Q_{gg}$, with the notations having their usual meanings.

The P:V ratios of the mass distributions of fission fragments gated with α, t, d and p at respective excitation energies have been shown as filled stars, filled squares, hollow squares and filled diamonds respectively in Fig. 5.6 (a) for ^{6}Li and Fig. 5.6 (b) for ^{7}Li projectiles respectively. The P:V ratios of FF mass distributions for all the transfer- or ICF-fission channels are found to be higher than the ones for total fission for a particular beam energy. Obviously, any admixture of ICF fission with CF fission will increase the P:V ratio of the total fission at the excitation energy corresponding to CF fission, thus explaining the difference in the P:V ratios between CF fission and total fission. It may also be emphasized that the measured P:V ratio for each of these transfer induced fissions at proper excitation energy is found to follow the trend of the

P:V ratios of mass distributions of fission fragments emitted from similar compound nuclei, populated in p +^{239}Pu and p +^{238}U reactions, measured by Ohtsuki *et al.* [74] and Ferguson *et al.* [75] respectively.

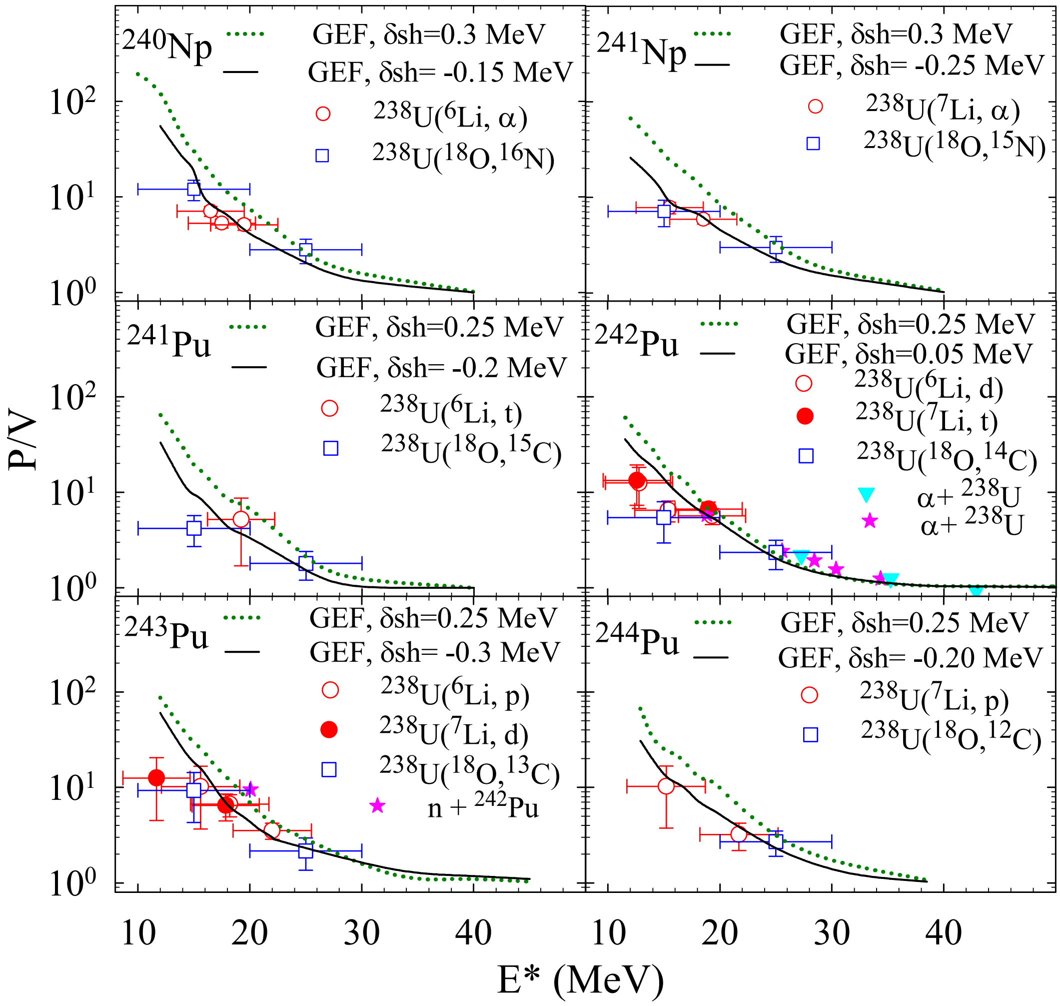

Figure 5.8: Comparison of the experimental P:V ratios of nuclei populated in present transfer reactions (circles) with the ones available in the literature (squares[30], triangles[76] and stars[77, 78]) and the GEF calculations (solid and dotted lines).

The P:V ratio for all the fissioning nuclei, namely, ^{240,241}Np and ^{241,242,243,244}Pu, have been compared with the available literature data as shown in Fig. 5.8. From the mass distributions reported in Ref. [30], the P:V ratios have been deduced and shown as blue squares in Fig. 5.8. Additional data for ^{242}Pu (pink stars [77], magenta triangles [76] in Fig 5.8 (d)) and for ^{243}Pu (pink star [78] in Fig 5.8 (e)) have also been compared. It can be observed that the excitation energy dependence of the present P:V ratio is consistent with the trend of the literature except the lone data point of ^{243}Pu which is lying above the present data (as well as that of Ref. [30]).

5.3.1 Calculation using GEF (General Description of Fission observables) model

The above experimental data have been compared with the P:V ratios calculated using a semi-empirical code GEF, version 2016/1.2 [4, 79], where two main inputs are: excitation energy and RMS angular momentum (calculated assuming grazing collision in transfer reaction). A list of the main parameters that determine the fragment yields in GEF is also given in Ref. [80]. For all the nuclei, the calculations with modified shell correction parameter (Table 5.1) for symmetric fission, represented by black solid lines in Fig. 5.8, agree with the experimental data reasonably well, compared to the calculations with default value (green dashed lines in Fig. 5.8), implying that the value of the shell correction for symmetric fragments plays an important role in FF mass distribution. The importance of the above shell correction is further illuminated as follows.

Table 5.1: Shell correction parameters for symmetric fission fragments.

Fissioning nuclei	δ_{sh} (default)	δ_{sh} (modified)
^{240}Np	0.3	-0.15
^{241}Np	0.3	-0.25
^{241}Pu	0.25	-0.20
^{242}Pu	0.25	0.05
^{243}Pu	0.25	-0.3
^{244}Pu	0.25	-0.2

In GEF, the P:V ratio of mass distribution depends on the relative yields of the asymmetric and the symmetric fission channels determined by the population of states in the respective fission valleys at or slightly beyond the outer fission barrier in thermal equilibrium. Fission valleys beyond the outer fission barrier are assumed to be essentially formed by fragment shells. In the actinides, where asymmetric fission prevails at low excitation energies, the depths of the asymmetric valleys decreases faster than the depth of the symmetric valley as energy increases [81], because the shell effect in the asymmetric valleys is larger.

For asymmetric fission, the mass of one of the fragments is independent of the fissioning system as it achieves shell closed configuration. For example, one of the fragments gains the mass $\sim$ 140u for all the fissioning systems in the actinide regions. Since the value of the shell correction for asymmetric fission is quite large, it is well determined for many fissioning systems and has already been taken into account in GEF code (by default).

In contrast, the mean mass in the symmetric channel unavoidably vary as a function of mass of the fissioning system. Since the binding energy of all nuclei in any shape is influenced by shell effects, the depth of the symmetric fission valley is modulated by (normally weak) shell effects. These shell effects depend on the fissioning system, and, thus the strength of this shell effect in the symmetric valley needs to be fixed by a measured value of the peak-to-valley ratio for the system of interest as done in the present case.

5.4 Measurement of incomplete fusion cross-sections

It is now well established that the ICF or transfer induced fission play an important role in the dynamics of total fission. For example, the presence of ICF channels modifies (i) the ratio of asymmetric to symmetric fission mass distributions, (ii) the width of fission fragment folding angle distributions, and (iii) the anisotropy of FF angular distributions. The same has been confirmed by a direct measurement of fission fragment mass distributions for different ICF or transfer-induced fission channels in ^{6,7}Li+^{238}U reactions (described in the previous section). It has also been confirmed that the folding angle distributions for individual ICF fissions peak around the same angles where kink like structures were observed in the folding angle distribution of total fission, thereby enhancing the width of the folding angle distributions of total fission at below barrier energies. Another important feature of a reaction involving weakly bound stable projectiles (^{6,7}Li and ^{9}Be) is the suppression of complete fusion cross-sections at energies above the Coulomb barrier[17, 18, 19, 20, 21, 22, 23, 24]. Interestingly, it has been observed that the cross sections for incomplete fusion for some of these systems [27, 28] are found to be of similar order as that of the missing complete fusion cross sections.The above examples lead to a fact that identification of different ICF channels and measurement of their cross sections is of utmost importance to understand many interesting features both qualitatively as well as quantatively in reactions involving weakly bound projectiles.

In literature, several methods have been employed to identify ICF channels, such as, by measuring (i) recoil range distributions, (ii) fission fragment folding angle distributions, (iii) characteristic charge particle decay from composite nuclei (iv) particle-gamma coincidence, and (v) coincidence of fission fragments with light charged particles. The recoil range distribution method [82, 83, 84] is applied for measurements only at above barrier energies where the ranges of the recoils corresponding to CF and ICF are supposed to be different. However, practically it has been observed that the ranges have a good overlap leading to large uncertainties in the separation of CF and ICF contributions. In the second method Itkis *et al.* [15] have extracted the contributions of ICF channels from the fit to the fission fragment folding angle distributions for ^{6}Li+^{232}Th system. Different peaks of the folding angle distribution correspond to different ICF channels. Using the same method, Kailas *et al.* have estimated the transfer fission cross section for ^{11}B+^{237}Np, ^{12}C+^{236}U and ^{16}O+^{232}Th systems [35]. However, there are large uncertainties in the fit to such peaks that lead to large errors in the extracted cross sections. Using the third technique, Dasgupta *et al.* [28] have measured the ICF cross-sections for the ^{6}Li+^{209}Bi, ^{7}Li+^{209}Bi, and ^{9}Be+^{208}Pb reactions, at energies near and below the Coulomb barrier where the ICF channels have been identified by characteristic α decay from the composite system. It has been mentioned that some of the composite systems may have been formed by both CF as well as ICF modes. Using the fourth technique, the ICF cross-sections due to triton (t) or alpha (α) capture have been measured using online and offline gamma counting for ^{7}Li+^{124}Sn [27], ^{7}Li+^{93}Nb [85] and ^{7}Li+^{178}Pt [86] systems. In this technique, gamma ray obtained in coincidence with the escaping particle has only been used to identify the composite system, but the cross-sections have been determined from the inclusive gamma counts. The fifth technique, i.e. light charged particle-fission coincidence technique has been used by Raabe *et al.*[29] to obtain ICF cross-sections in ^{7}Li,^{7,9}Be +^{238}U reactions.

It may be pointed out that out of all the techniques mentioned above, the last technique, i.e., 'light-charged-particle and fission-fragments coincidence' technique is the most reliable, as the triple coincidence of two fission fragments and one light-charged-particle (the non-captured projectile breakup fragment) confirms the occurrence of a specific ICF event. Whereas, the characteristics particle decay technique and the gamma counting technique have the major disadvantage that the same composite system which emits characteristics gamma or particle, can be formed by different mechanisms (ICF or CF followed by particle evaporation). In the present work, we have used the last technique i.e., the 'light-charged-particle and fission-fragment coincidence' technique to measure the cross sections for individual ICF (with respect to p, d, t and α-gated) channels, for the ^{6,7}Li+^{238}U reactions. It may be noted that p, d, t and α-

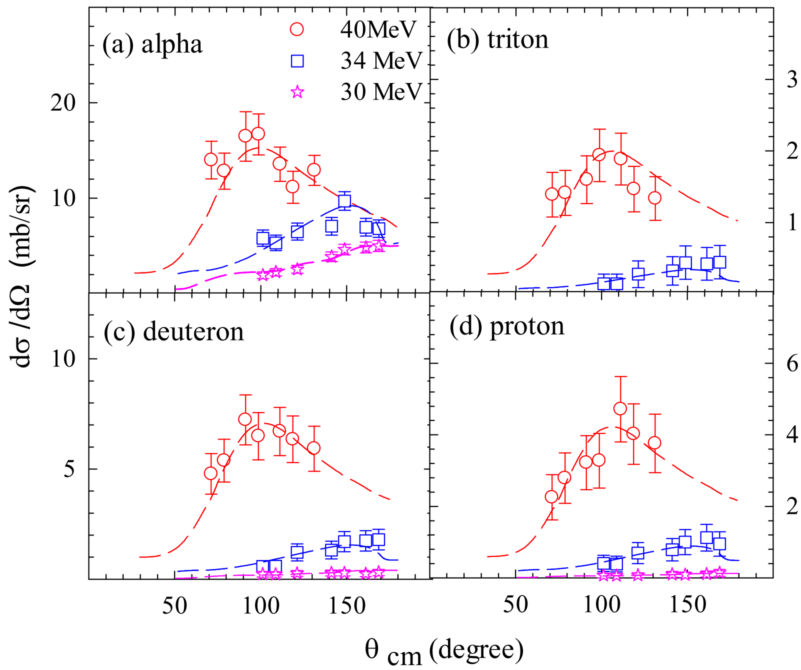

Figure 5.9: The differential ICF cross-sections at 40 MeV (red circle), 34 MeV (blue square) and 30 MeV (pink star) projectile energies corresponding to the ejectiles (a) alpha (b) triton (c) deuteron and (d) proton in ^{6}Li+^{238}U reaction. The fit to each of the data has been shown by dashed lines.

gated ICF channels correspond to the captures of ^{5}He, α, ^{3}He and d respectively in case of ^{6}Li projectile and captures of ^{6}He, ^{5}He, α and t respectively in case of ^{7}Li projectile. An attempt has also been made to address the quantitative difference in P:V ratio between total-fusion-fission and complete-fusion-fission as observed in Ref. [16], using the simulated mass-distributions for inclusive fission by overlapping the distributions for complete fusion and all ICF-fissions, taking into account proper weight factor proportional to the respective measured cross-sections.

5.4.1 Methods

Incomplete fusion (ICF) is a process where one of the breakup fragments is captured by the target following the breakup of the projectile into two or more fragments. Sometimes, the same set of nucleons as that of the fragment may be directly transferred from the projectile to the target, making the stripping transfer reaction indistinguish-

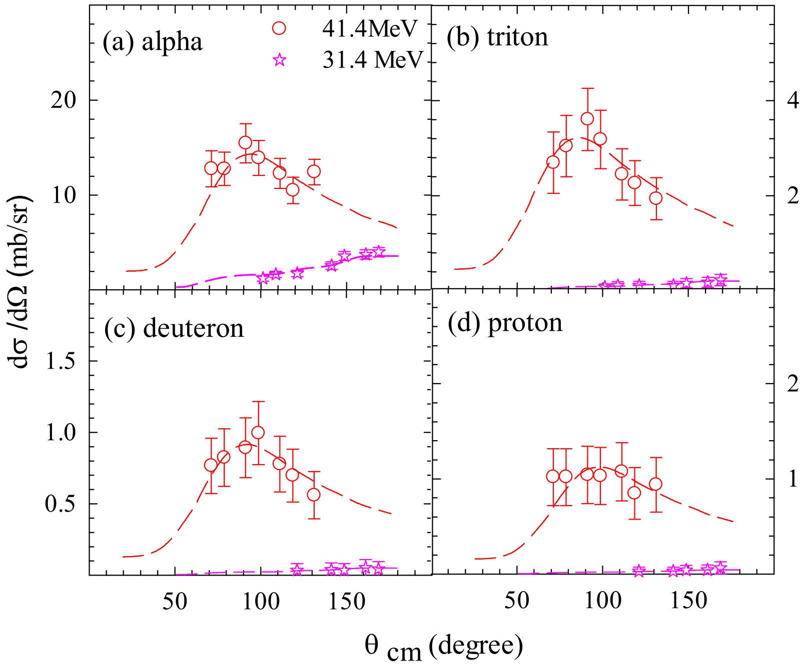

Figure 5.10: The differential ICF cross-sections at 41.4 MeV (red circle) and 31.4 MeV (pink star) projectile energies corresponding to the ejectiles (a) alpha (b) triton (c) deuteron and (d) proton in ^{7}Li+^{238}U reaction. The fit to each of the data has been shown by dashed line.

able from the ICF process. If the target is in actinide region, after capturing the fragment, the composite system readily undergoes fission. So, experimentally we can detect two fission fragments in coincidence with the escaping projectile like fragment (the ejectile) without distinguishing the origin of the process, ICF or transfer. The ICF cross-section which includes transfer cross-section as well, can be determined as follows. If Y_{coin} is the counts of the non-captured projectile like breakup fragments detected in coincidence with the two fission fragments, the differential ICF cross-section can be written as

$$\frac{d\sigma}{d\Omega}(\theta) = \frac{Y_{coin}}{Y_M}\frac{d\Omega_M}{d\Omega_{CsI}}\frac{d\sigma_{Ruth}}{d\Omega}\frac{1}{\epsilon}\frac{1}{P_f} \tag{5.3}$$

where, Y_M is the number of counts at monitor detector, $d\Omega_M$ and $d\Omega_{CsI}$ are the solid angles of monitor and CsI(Tl) scintillator detectors respectively, $\frac{d\sigma_{Ruth}}{d\Omega}$ is the Rutherford's differential scattering cross-section at the scattering angle of the monitor (θ_M),

ϵ is the 'fission-PLF' coincidence efficiency and P_f is the fission probability followed by transfer or incomplete fusion. The efficiency ϵ mainly depends on two factors: (a)the FF coincidence efficiency between the two MWPC detectors (ϵ_1) and (b) the geometric efficiency of the MWPC detectors (ϵ_2).

(a)*FF coincidence efficiency,* ϵ_1: Although the MWPC detectors have been placed in such a position that their central angles are at folding angles, but due to the finite width of the folding angle distribution, there is a chance that one of the two complementary fission fragments from a single fission event may miss the coincidence detection by the MWPC detectors. Hence, the inter detector coincidence efficiency have been determined using a Monte Carlo simulation assuming isotropic emissions of fission fragments in centre of mass frame, though it is not a valid assumption since FF angular distribution is in general anisotropic. However, for the present systems, FF angular anisotropy being less ($\sim 10-20\%$), the above assumptions is reasonable. Thus, using the Monte-Carlo simulation, the inter detector coincidence efficiency (ϵ_1) have been obtained and found to be $\sim 70-80\%$ for the present systems at all excitation energies.

(b)*Geometric efficiency,* ϵ_2: Geometric efficiency of the MWPC detectors depend on the effective solid angle of the detectors. It can be calculated from the formula $\epsilon_2 = \frac{d\Omega_{MWPC1}+d\Omega_{MWPC2}}{4\pi}$.

Therefore, the product of ϵ_1 and ϵ_2 will be equal to the total coincidence efficiency (ϵ). Now P_f has been calculated using GEF code, version 2016/1.2 [79], where three main inputs are: fissioning nuclei, excitation energy and RMS angular momentum (calculated assuming grazing collision in transfer reaction). P_f has been found to be $\sim 80-95\%$ for all the fissioning systems at the measured excitation energies.

The 'FF-PLF' coincidence counts will also depend on the position of the MWPC detectors, because of anisotropy of FF angular distribution. However, the anisotropy being small for the present systems at measured energy ranges, the ICF cross-sections have been obtained by integrating the differential cross-section over the all solid angles of PLF detectors.

$$\sigma_{ICF} = \int \frac{d\sigma}{d\Omega}(\theta) d\Omega = 2\pi \int_0^{\pi} \frac{d\sigma}{d\Omega}(\theta) \sin\theta d\theta \tag{5.4}$$

5.4.2 Results

Following equation (1) the differential cross-section as a function of θ_{cm} for alpha , triton, deuteron and proton gated ICF reactions on ^{6}Li+^{238}U systems, have been obtained for 40 (red circle), 34 (blue square) and 30 MeV (pink star) projectile energies and shown in Fig 5.9 (a), (b), (c) and (d) respectively.

Similarly, the differential cross-section as a function of θ_{cm} for alpha, triton, deuteron and proton gated ICF reactions on ^{7}Li+^{238}U systems, have been obtained for 41.4 (red circle) and 31.4 MeV (pink star) projectile energies and shown in Fig. 5.10 (a), (b), (c) and (d) respectively. In both the cases it is clearly observed that the differential cross-section is the highest for alpha emission and lowest for proton emission at all the measured energies.

It may be noticed that the data presented in Figs. 5.9 and 5.10 are of limited angular range surrounding the peaks though they cover the majority of the cross sections. So, in order to get the angle integrated cross section, a suitable fit with proper shape to the angular distribution data is necessary. The shape of the angular distribution of the inclusive alpha cross section for reactions involving weakly bound projectiles is known to be similar to that of the transfer reaction, i.e., both of these reaction cross sections peak at the grazing angles [87]. In the present measurements the coincident PLF angular distributions at different energies indeed peak at the respective grazing

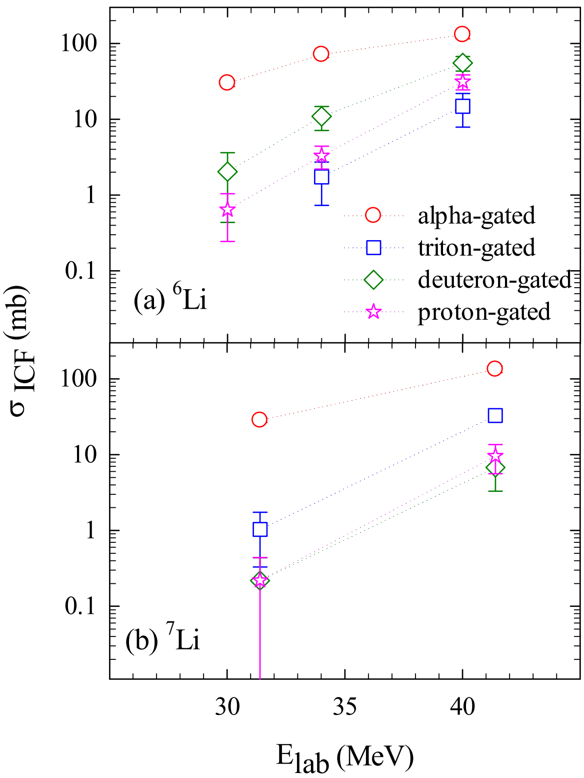

Figure 5.11: The angle integrated ICF cross sections corresponding to the ejectile α (red circle), t (blue square), d (green diamond), and p (pink star) at different energies of the projectile (a) ^{6}Li and (b) ^{7}Li.

angles. The shape of the angular distributions at a particular beam energy normalized to Coulomb barrier is expected to be similar to that for a nearby system, e.g., ^{6}Li+^{209}Bi [87]. Since the differential cross-sections for inclusive alpha are available for a wide angular range at several near barrier beam energies, the shapes of these data at matching beam energy of E_{cm}/V_b has been used to fit the present data for each PLF angular distribution. The fits to the PLF angular distribution data corresponding to α, t, d, and p-gated fissions are shown by dashed lines in Figs. 5.9 and 5.10.

Next, using Equation (2) the angle integrated ICF cross sections corresponding to the outgoing non-captured fragments like α (red circle), t (blue square), d (green diamond), and p (pink star) have been obtained at different projectile energies as shown in Fig. 5.11(a) for ^{6}Li and (b) for ^{7}Li. It has been found that alpha emission is the most dominant ICF channel in both the reactions. The ICF cross-sections have been observed to increase with increasing projectile energy, as expected. At higher ^{6}Li projectile energies the sequence of different ICF cross-sections associated with different non-captured fragments is observed to be $\sigma_\alpha > \sigma_d > \sigma_p > \sigma_t$, whereas for ^{7}Li, the sequence is $\sigma_\alpha > \sigma_t > \sigma_d > \sigma_p$. At lower projectile energies for ^{6}Li, $\sigma_p \sim \sigma_t$, whereas for ^{7}Li, $\sigma_p \sim \sigma_d$. The total ICF cross-section at a particular beam energy has been obtained by summing all the individual ICF cross-sections measured at that energy. The measured total ICF cross-sections, available TF cross-sections from the literature [13, 55] and CF cross-sections (calculated by subtracting total ICF cross-sections from total fusion cross-sections), have been compared in Table 5.2.

Table 5.2: ICF, TF and CF cross-sections for ^{6,7}Li+^{238}U systems.

Beam	Energy (MeV)	ICF x-section (mb)	TF x-section (mb)	CF x-section (mb)
^{6}Li	30	32.6 $\pm$ 3.4	47.0 $\pm$ 7.0	14.4 $\pm$ 7.8
	34	87.2 $\pm$ 7.2	258 $\pm$ 26.0	170.8 $\pm$ 27.0
	40	232.4 $\pm$ 21.6	807 $\pm$ 40.0	574.6 $\pm$ 45.5
^{7}Li	31.4	29.9 $\pm$ 2.1	62 $\pm$ 4.0	32.1 $\pm$ 4.5
	41.4	183.2 $\pm$ 14.9	950 $\pm$ 50.0	766.8 $\pm$ 52.1

5.4.3 Systematics of ICF and TF cross sections

(a)Ratio of ICF to TF cross sections:

To find the relative contribution of ICF to total fusion cross-section, the ratio of cross section for ICF to TF, i.e., $\frac{\sigma_{ICF}}{\sigma_{TF}}$ has been determined from the measured data at different energies and shown in Fig. 5.12 as red filled (red hollow) circles for ^{6}Li (^{7}Li) +^{238}U reaction. For a systematic study, the same quantity has been determined from the ICF and TF data available in the literature for several other systems involving weakly bound projectiles [27, 28, 29, 86, 88, 89] and compared with the present data in the same figure. The relative contribution of ICF to TF for the present systems has been found to be the highest ($\sim$ 70%) at the lowest measured energy and then it decreases with increasing energy, consistent with the trend for all the other systems obtained from the systematics. It is observed that the ICF to TF ratio for the present ^{6}Li+^{238}U system is nearly equal to that of ^{6}Li+^{209}Bi system [28] at near or below barrier energies. But, the ratio for ^{7}Li+^{238}U system obtained from the present measurement as well as from Ref. [29] is found to be slightly smaller than other systems available in the literature with ^{7}Li as a projectile. From the systematic study, it is interesting to note that the ratio of ICF to TF at above barrier energies is nearly equal to the complete fusion suppression factors for both the projectiles.

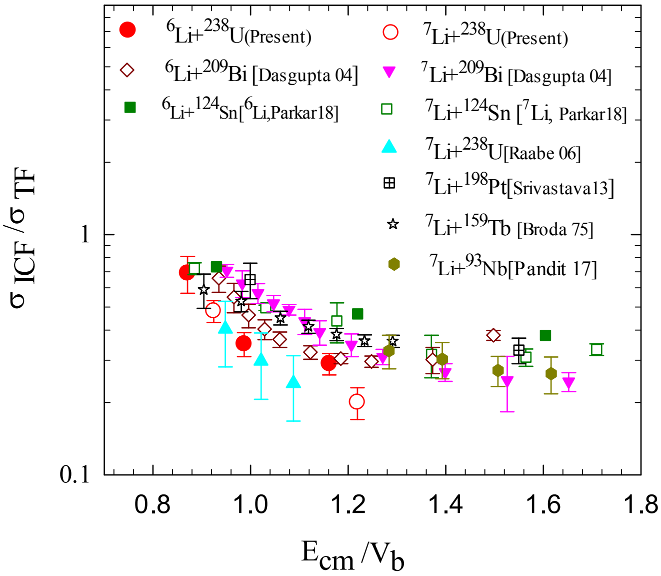

Figure 5.12: The ratios of total ICF cross-section to total fusion cross-section for the present systems ^{6}Li+^{238}U (red filled circles) and ^{7}Li+^{238}U (red hollow circles) have been compared with the literature data for ^{7}Li+^{124}Sn [27], ^{6}Li+^{124}Sn [88], ^{6}Li+^{209}Bi [28] and for ^{7}Li+^{209}Bi [28], ^{7}Li+^{238}U [29], ^{7}Li+^{196}Pt [86] and ^{7}Li+^{159}Tb [89].

(b)Systematics of TF cross sections:

Further to understand the role of projectile breakup threshold the ratio of TF cross sections for reactions with ^{6}Li projectile to that with ^{7}Li projectile but same target has been obtained as shown in Fig. 5.13. It may be observed that at above barrier energies the ratio is almost constant but as one goes down in energy the ratio increases sharply. Due to low breakup threshold of ^{6}Li (compared to ^{7}Li), the breakup cross sections for reactions involving ^{6}Li are expected to be higher leading to higher ICF cross section and higher TF cross sections than the reactions involving ^{7}Li. At sub-barrier energies the difference is expected to be much larger as the fusion cross sections vary exponentially with the difference in beam energy and fusion barrier.

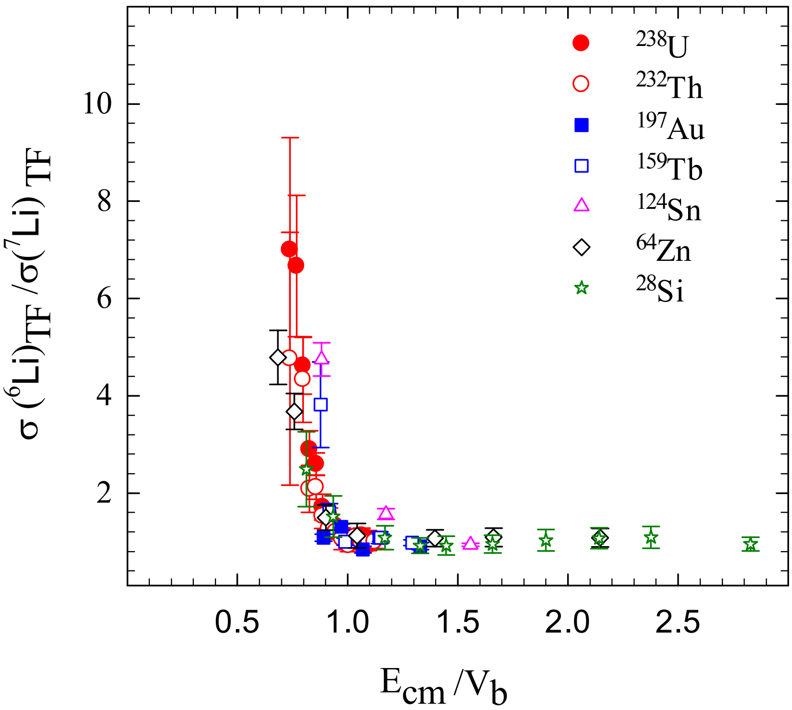

Figure 5.13: Ratio of the ^{6}Li to ^{7}Li induced total fusion excitation functions as a function of E_{cm}/V_b for different targets[55, 88, 90, 91, 92].

5.4.4 Understanding mass distribution of TF-fission

As stated earlier, a difference in peak to valley ratio (P:V) of mass distributions between TF-fission and CF-fission has been observed in ^{6,7}Li+^{238}U reactions [16] and ICF-fission was assumed to be the reason for this discrepancy. In our recent work [93], the mass-distributions of the nuclei populated in those ICF-channels have been measured for the same reactions and the P:V ratio of all the ICF channels (α, t, d and p-gated fissions) have been already obtained. In the present study, it has been possible to determine the cross-sections for individual ICF and CF channels (see Fig. 5.11 and Table 5.2). So, one can now obtain the combined (CF+ICF fission) mass distribution that can be compared with the experimental mass-distribution for TF-fission.

A typical case of mass distribution measured in ^{6}Li+^{238}U reaction at the beam energy of 30 MeV, where the difference between CF and TF fission is maximum, has been considered for the above purpose. An overlap of the mass-distributions of all ICF channels with the CF channel with proper weight factor proportional to the measured cross-sections has been obtained. The percentage contribution of CF and different ICF fissions to total fission is given in Table 5.3. In Fig. 5.14, the fits to the experimental mass distributions for CF, α-gated, t-gated, d-gated and p-gated fission events obtained from Ref. [93] have been shown by black dotted, red short-dashed, pink long-dashed, blue dash-dotted and green dash-dot-dotted lines. The experimental mass distributions for CF and TF fissions have been shown as black hollow circles and red filled circles respectively. The fits to each of the mass distributions for CF and individual ICF channels have been generated by overlapping two Gaussian distributions after reproducing the experimentally determined P:V ratio given in Ref. [93]. Here, the second peak corresponding to higher mass has been kept at a fixed mass $\sim 140u$ and the mass for lighter group has been varied according to the mass of the fissioning nuclei. Using these fits the overlap of all the mass distributions has been obtained using the following relation.

$$Y_{TF}(m) = \frac{\sigma_{CF} Y_{CF}(m) + \sum_i \sigma_{i-gated} Y_{i-gated}(m)}{\sigma_{TF}}$$
$$(i = \alpha, t, d, p) \tag{5.5}$$

Table 5.3: Percentage contributions of CF,α-gated, t-gated, d-gated and p-gated fission in ^{6,7}Li+^{238}U reactions.

Beam	Energy (MeV)	CF (%)	α-gated (%)	t-gated (%)	d-gated (%)	p-gated (%)
^{6}Li	30	30.6 ± 17.2	63.7 ± 11.4	-	4.3 ± 3.4	1.4 ± 0.8
	34	66.2 ± 12.4	27.6 ± 3.6	0.7 ± 0.4	4.2 ± 1.5	1.3 ± 0.4
	40	71.2 ± 6.7	16.2 ± 2.0	1.8 ± 0.9	6.9 ± 1.5	3.9 ± 0.9
^{7}Li	31.4	51.7 ± 8.0	45.9± 4.4	1.7 ± 1.1	0.4 ± 0.3	0.3 ± 0.3
	41.4	80.7 ± 6.9	14.1 ± 1.5	3.5 ± 0.5	0.7± 0.4	1.0±0.4

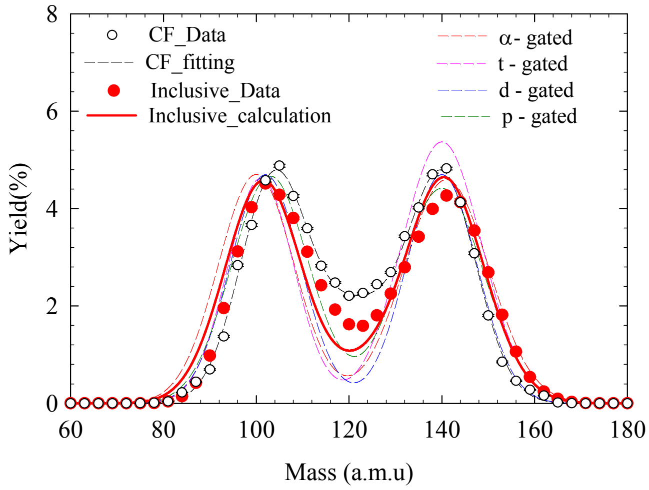

Figure 5.14: Mass-distributions for CF-fission and α,t,d and p gated fission have been shown by black ,red, pink, blue and green dashed lines respectively for 31.4 MeV ^{7}Li beam. The overlapping mass-distributions obtained from equation (5.5) have been shown by solid red line.

The overlapping mass-distribution thus obtained for total fission has been shown as the red solid line in Fig. 5.14. It is clearly observed that P:V ratio of the overlapping mass-distribution is larger than the one for CF-fission. Similar exercise has been carried out at remaining energies for ^{6}Li+^{238}U as well as ^{7}Li+^{238}U systems and the results for the P:V ratios obtained from the simulated mass distributions for the inclusive-fission have been compared with the ones obtained from the measurements [16, 93] in Table 5.4. The calculated P:V ratios of the simulated mass-distributions for inclusive fission are found to be consistent with the experimental values within experimental uncertainty.

Table 5.4: Calculated and experimental P:V ratios for ^{6,7}Li+^{238}U systems.

Beam	Energy (MeV)	$(P/V)_{calculated}$	$(P/V)_{experimental}$
^{6}Li	30	3.9 ± 2.0	2.80 ± 0.10
	34	2.3 ± 0.9	2.00 ± 0.05
	40	1.9 ± 0.5	1.56 ± 0.01
^{7}Li	31.4	3.2 ± 1.8	2.39 ± 0.10
	41.4	1.66 ± 0.3	1.56 ± 0.01

5.5 Summary

In summary, the FF folding angle distributions have been measured in coincidence with projectile breakup fragments to find out the influence of transfer- or ICF-fission on inclusive fission. The peaks of the folding angle distributions corresponding to the dominant transfer- or ICF-fission channels were found to be at same positions where additional kinks were observed in inclusive fission at below-barrier energies. This confirms that the presence of the kinks and the enhancement of the width of FF folding angle distributions at sub-barrier energies is again due to the transfer- or ICF-fission channels.

The mass distributions of fission fragments emitted from several nuclei namely, ^{241,242,243,244}Pu and ^{240,241}Np, populated in multi-nucleon transfer or ICF channels in the ^{6,7}Li+^{238}U reactions, have been measured for several projectile energies around the Coulomb barrier. The P:V ratios of mass distributions for the fission fragments in coincidence with PLFs like α, t, d and p are much larger than the ones for inclusive fission fragments at any particular projectile energy. It provides a direct confirmation that the contamination of transfer- or ICF-fission with CF-fission is the prime factor behind the enhancement in P:V ratio observed for inclusive fission compared to CF-fission.

The P:V ratio of FF mass distributions for the fission of ^{241,242,243,244}Pu and ^{240,241}Np have been found to be in good agreement with the available literature data. It may be emphasized that the mass-distributions of ^{244}Pu nuclei, formed by capture of ^{6}He by ^{238}U target have been studied in the excitation energy range complementary to that of Ref [30]. The results of GEF calculations with modified value of shell correction for symmetric fission was required to reproduce the energy dependence of the P:V ratio. This observation will initiate more work in both experimental and theoretical studies involving actinide compound nuclei where shell correction for symmetric fragments plays an important role in FF mass distribution.

It is important to note that, the mass-distributions of the fissioning nuclei ^{244}Pu and ^{241}Np cannot be measured using the fusion reaction of any stable target and heavy ion projectile combination. These nuclei have been populated by the capture of ^{6}He and triton respectively by ^{238}U target. Hence, the multi-nucleon transfer reactions provide us a powerful tool to explore fission studies of the nuclei which can not be populated by stable projectiles.

The cross sections for individual transfer-induced fission or incomplete-fusion fission channels in ^{6,7}Li+^{238}U reactions have been measured using the 'fission-fragments and light-charged-particle coincidence' technique. In this triple coincidence measurement, the two fission fragments were detected using large area MWPC detectors and the light charge particles were detected using CsI detectors. The coincidence efficiency between two MWPC detectors, required for calculating cross sections, has been determined using a Monte-Carlo simulation.

The cross sections for incomplete fusion have also been obtained at different energies by multiplying the above ICF-fission cross sections by the respective excitation energy dependent fission probabilities calculated using GEF code (Version 2016.VI.1.2) [79].

It may be noted that the p, d, t and α-gated ICF channels correspond to the captures of ^{5}He, α, ^{3}He and d respectively in case of ^{6}Li projectile and captures of ^{6}He, ^{5}He, α and t respectively in case of ^{7}Li projectile. The cross-sections for ICF followed by d-capture and t-capture for ^{6}Li and ^{7}Li projectile respectively, have been found to be the most significant channels at all the measured energies. Total ICF cross-sections for a projectile energy have been obtained by adding individual ICF channels measured at that beam energy. The ratio of total ICF-cross-section to total (CF+ICF) fusion cross-section have been obtained and compared with the literature data. Interestingly, the ratio of ICF to TF at above barrier energies for ^{6}Li(^{7}Li)+^{238}U reaction was found to be ∼30% (20%) which is of same order as the complete fusion suppression factor commonly observed in reactions involving weakly bound projectile ^{6}Li(^{7}Li). The ratio of TF cross sections for ^{6}Li to that of ^{7}Li involving same target is also found to increase with the decrease in energy at sub-barrier energies. This result along with the previous result (ICF to TF ratio) manifests the effect of projectile breakup threshold.

The mass-distributions for TF fission, simulated by overlapping the distributions for CF-fission and different ICF-fission channels with appropriate weight factors proportional to the measured CF and ICF cross-sections, quantitatively explain the difference in the peak to valley ratios between TF- and CF-fission for the present systems within the experimental uncertainty.

Chapter 6

Fission Fragments Mass Distributions in ^{10,11}B+^{238}U reactions

In the last two chapters, we have discussed measurement of different fission observables including FFAD, FFMD for fission following breakup or transfer in reactions involving weakly bound projectiles ^{6,7}Li. We have also investigated the effect of those ICF-fission channels on total fission both qualitatively as well as quantitatively. We have also measured the cross-sections for the incomplete fusion channels via fission-light charged particle coincidence technique. The relative contribution of the combined ICF cross sections to total fusion involving ^{6,7}Li was found to be close to the CF suppression factors (30% and 20% respectively) observed for the reactions involving same weakly bound projectiles. Similar to ^{6,7}Li and ^{9}Be, two more stable projectiles, i.e., ^{10,11}B are sometimes considered to be weakly bound projectiles but with larger breakup threshold compared to that of ^{6,7}Li. From the systematics, the CF suppression factors for reactions involving ^{10}B and ^{11}B projectiles are observed to be $\sim$ 10% and 5% respectively [20, 51]. Hence, it will be very interesting to study fission fragments mass distributions in ^{10,11}B+^{238}U reactions and look for the features as observed in the previous reactions.

6.1 Experiment and data analysis

The experiment on $^{10,11}B + ^{238}U$ reactions was carried out at BARC-TIFR Pelletron Linac facility using pulsed beam having bombarding energy ranging from 53-65 MeV. The same ^{238}U target mentioned in the previous chapter has been used for the present experiment. The availability of pulsed beam excluded the need for any START detector. Thus, the experimental setup gets simplified as compared to the experiment mentioned in the last chapter. Here, the two MWPC detectors which have been developed in-house (discussed in Chapter 3) have been used for measuring the fission fragments. As shown in Fig. 3.9, two MWPC detectors (MWPC1 and MWPC2) have been placed at folding angles at a distance of 41.4 cm and 39.4 cm respectively. Like earlier, the position signals were calibrated using the known dimensions of the active areas of the MWPC detectors and the overall 2D plots of X and Y positions. The timing signals were calibrated using a "Dual pulsar". Additionally, three telescopes made of Si-strip detectors, covering angular ranges of $\sim 120\,°$- $170\,°$, leaving a gap of $4°$ between two adjacent detectors, were used for measuring PLF.

6.2 FF mass distributions in $^{11}B + ^{238}U$ reaction

Following the same procedure as discussed in the previous chapter, the position spectra are first calibrated using the known dimensions of the detectors. Then position information (θ, ϕ) of the fission fragments in polar coordinates are determined from the position spectra. A typical $\theta_{fold} = (\theta_1 + \theta_2)$ vs. $\phi = (\phi_1 + \phi_2)$ plot has been shown for 61 MeV projectile energy in Fig. 6.1 (a), where the peak of the folding angle distributions (θ_{fold}) is observed at $\sim 165\,°$, consistent with the kinematics. The events corresponding to CF-fission are selected by choosing the intense part of the above plot. Here, the time of flight is measured with respect to the pulsed beam. Since the elastic

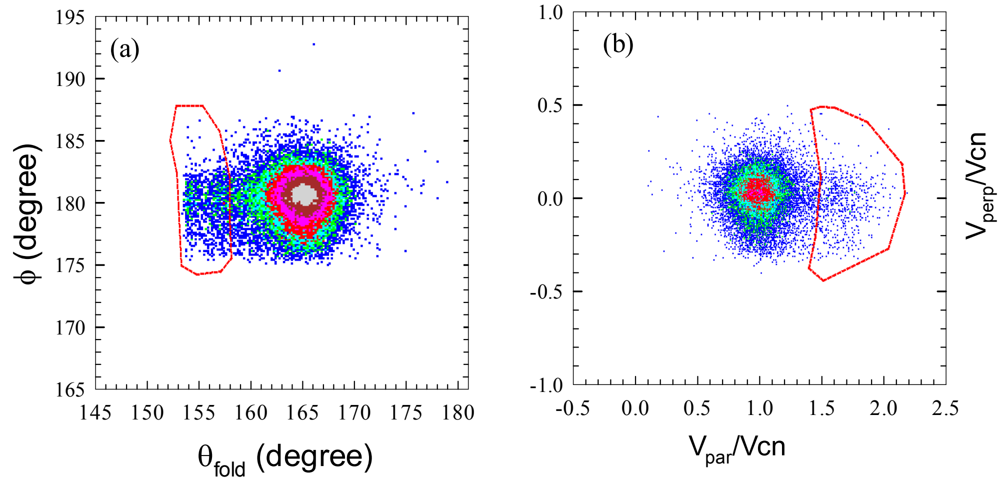

Figure 6.1: Typical (a)folding angle (θ_{fold}) vs. $\phi = (\phi_1 + \phi_2)$ plot and (b) $v_{\parallel}/v_{cn}$ vs. $v_{\perp}/v_{cn}$ plot obtained for 61 MeV projectile energy in ^{11}B + ^{238}U reaction . The events within the red contour correspond to transfer induced fission.

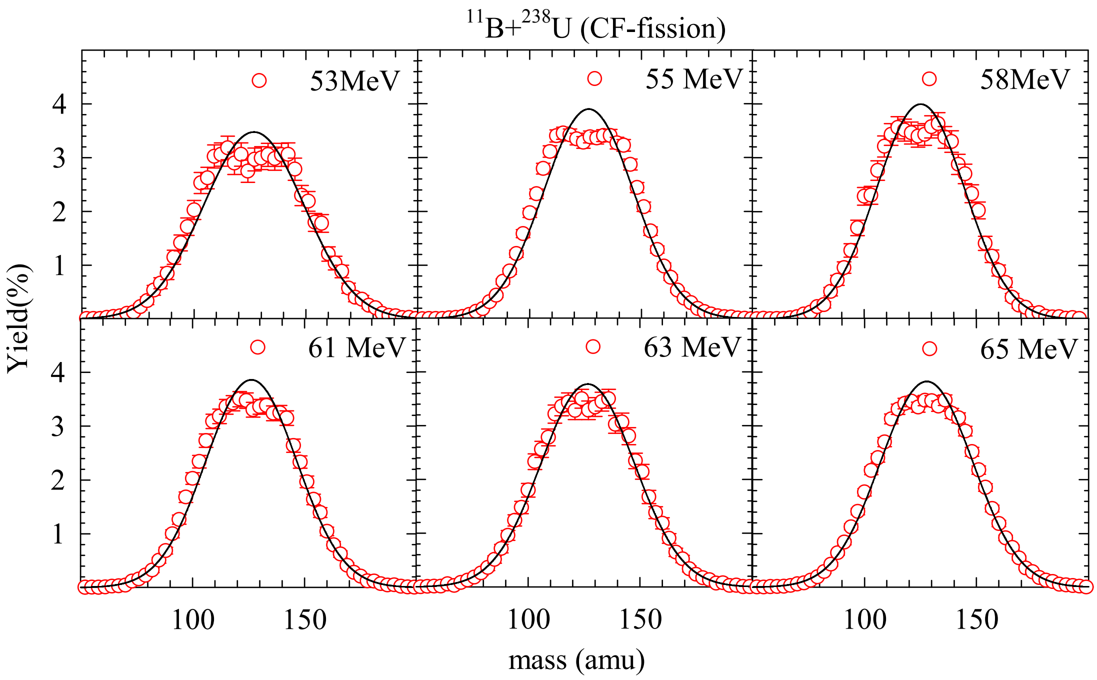

Figure 6.2: FF mass distributions obtained for CF fission in ^{11}B + ^{238}U reaction for beam energies in the range of 53-65 MeV. The fit to the data using single Gaussian function has been shown by black line.

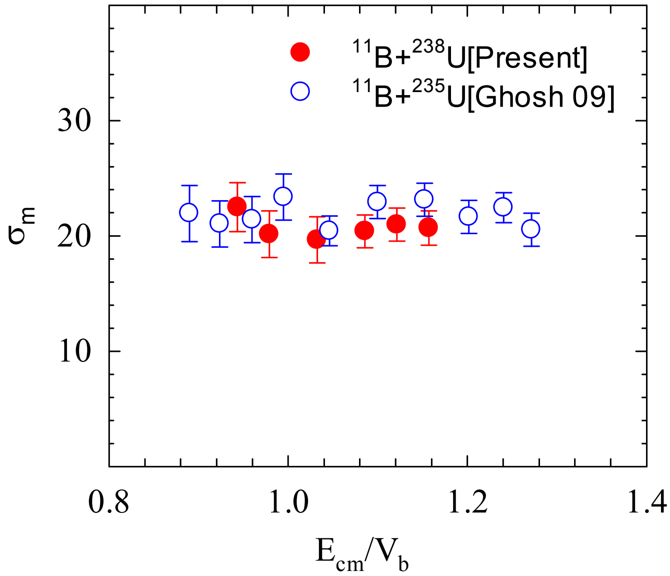

Figure 6.3: Width of the mass distributions for ^{11}B + ^{238}U (filled circle) and ^{11}B + ^{235}U (hollow circle, [95]) systems .

peak could not be clearly observed in the 'T1 vs. T2' plot, absolute timing of the fragments could not be directly obtained. Hence the timing difference method as discussed in Ref. [94] has been applied to derive mass distributions. Mass distributions for CF-fission thus obtained for the beam energies in the range of 53-65 MeV have been shown in Fig. 6.2. First each of the distributions is attempted to fit with a single Gaussian function. The width of the distributions is now compared with the ones for ^{11}B + ^{235}U system measured by Ghosh *et al.* as shown in Fig. 6.3.

To obtain a better fit specially at lower excitation energies, we attempt to fit the distributions using two Gaussian functions as done by Williams *et al.* [9] for ^{12}C + ^{232}Th system. The fit using two Gaussian functions have been shown by solid black line in Fig. 6.4, whereas blue dashed lines represent the two Gaussian functions separately. It is observed that, fit using two Gaussian functions describe the data better for all measured excitation energies. Presence of two Gaussian functions even for the highest measured energy (excitation energy $\sim$ 45 MeV) suggests the possible

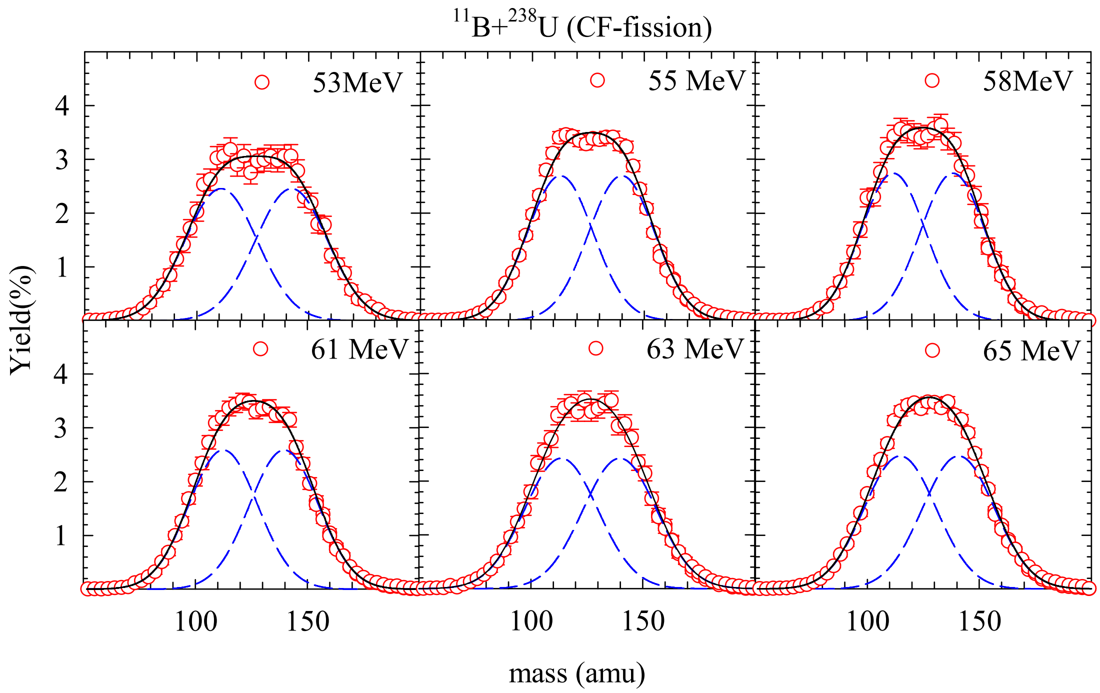

Figure 6.4: The fit to the above FF mass distribution data in Fig. 6.2 using double Gaussian function has been shown by black line, whereas two Gaussian functions are shown by dotted blue line.

presence of shell effect upto the highest measured excitation energy. Interestingly, contrasting observations regarding the persistence of shell effect have been reported earlier in literature. For example, Chaudhuri *et al.* [96] concluded the vanishing of shell effect at excitation energy $\sim$ 43 MeV, whereas Beck *et al.*[97] observed shell effect in the excitation energy range 45-50 MeV. So our observation is consistent with the ones by Beck *et al.*

The experimental distribution is now compared with the ones obtained from GEF code. As shown in Fig. 6.5, a reasonable agreement is observed between the experimental and theoretical distributions at the highest (65 MeV) measured energy. However at the lowest measured energy *i.e.* 53 MeV, the height of the GEF predicted distribution is slightly higher than the measured data, though the shapes of the peaks are similar..

All the mass distributions discussed above have been obtained using timing dif-

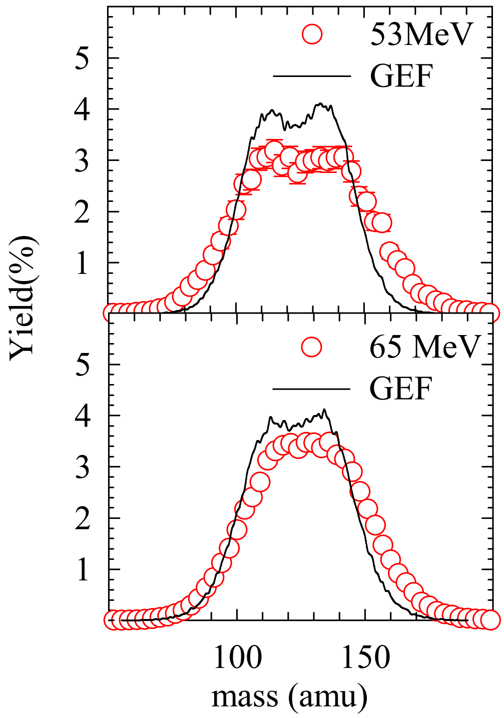

Figure 6.5: FF mass distributions obtained in $^{11}B + ^{238}U$ reaction have been compared with the ones obtained from GEF calculation for beam energies of 53 MeV (top panel) and 65 MeV (bottom panel).

ference method due to the difficulty in obtaining the absolute timing. However, as discussed in Ref. [94], the determination of the time zero for the time-of-flight spectrum for each energy is possible by imposing two conditions:(a) Setting the average $v_{\parallel}$ = v_{cn} and (b) ensuring that the mass ratio distribution is reflection symmetric about 0.5. Here from the first condition, the energy dependent time shift between RF signal and actual start of time of flight is determined whereas the second condition determines the constant (energy independent) electronic time delay between the two detectors. As shown in Fig. 6.1 (b) $v_{\parallel}/v_{cn}$ vs. $v_{\perp}/v_{cn}$ plot is indeed peaking at (1,0) coordinate, thereby confirming the accuracy of velocity calibration. Now one can apply the momentum conservation equations as discussed in the last chapter and obtain the mass distributions. It is observed that the mass distributions obtained from the two different methods are very close to each other (not shown here).

6.2.1 FF mass distributions for transfer induced fission

One of our objectives of the present study was to obtain the mass distributions for transfer induced fission. The signatures of transfer induced fission are already observed in Fig. 6.1 (marked by red contours). The events away from the intense band of (θ_{fold} vs. ϕ) plot or ($v_{\parallel}/v_{cn}$ vs. $v_{\perp}/v_{cn}$) plot actually correspond to the events originated from transfer induced fission. Now applying the momentum conservation equations one can obtain mass distributions in coincidence with PLF detected in the strip telescopes (see the set up in Fig. 3.9). The cross-sections for transfer induced fission in ^{11}B + ^{238}U reaction being low, the statistics for transfer fission is low. However, the FF mass distribution in coincidence with α (dominant channel) has been extracted as shown in Fig. 6.6.

The above mass distribution has been fitted using 2 gaussian functions (shown by dashed blue lines) and the resultant distribution has been shown by solid black line in

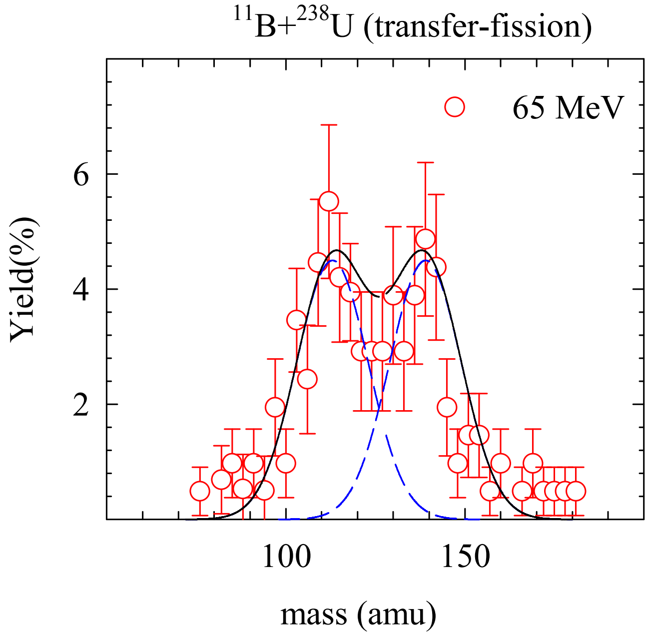

Figure 6.6: Mass distributions obtained in coincidence with α in ^{11}B + ^{238}U reaction for 65 MeV bombarding energy.

Fig. 6.6.

6.3 FF mass distributions in ^{10}B + ^{238}U reaction

Now FF mass distributions in ^{10}B + ^{238}U reaction has also been obtained only for CF-fission at single bombarding energy of 65 MeV and shown in Fig. 6.7. Following the similar approach as described earlier, the distributions have been fitted using single Gaussian (solid black line in Fig. 6.7(a)) as well as two Gaussian functions (solid black and blue dashed lines in Fig. 6.7(b)). Here, the width of the single Gaussian distribution is nearly equal to the width of the width at 65 MeV for ^{11}B + ^{238}U reaction. The statistics in inclusive fission itself being low, there was no scope to obtain mass distributions in coincidence with PLF.

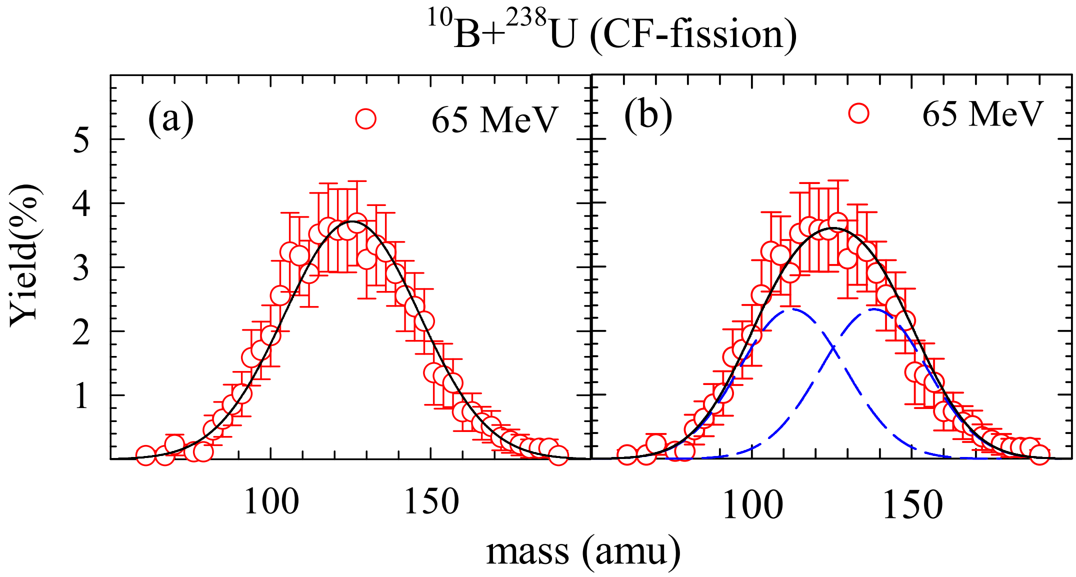

Figure 6.7: Mass distribution (hollow circle) for CF-fission obtained in $^{10}B + {}^{238}U$ reaction for 65 MeV beam energy. The (a) single Gaussian fit has been shown by black solid line and (b) sum of double gaussian functions (blue dashed lines) has been shown by black solid line.

6.4 Summary

FF Mass distributions in $^{10,11}B + {}^{238}U$ reactions have been obtained using two MWPC detectors developed in-house. The width of the mass distributions in $^{11}B + {}^{238}U$ reaction matches closely with the ones for $^{11}B + {}^{235}U$ system [95] . The mass distributions are also consistent with the ones obtained from GEF code. It is interesting to note that a single Gaussian could not fit properly the mass distributions for $^{11}B + {}^{238}U$ reaction at all the measured energies. The fits using two Gaussians provide much better fit even at the highest beam energy (with equivalent CN excitation energy of ∼45 MeV). This implies that shell effect does not wash away even at excitation energy of 45 MeV. The GEF predictions corroborate with the experimental results. The mass distribution in coincidence with α in $^{11}B + {}^{238}U$ reaction has been obtained at one energy, but with limited statistics. More statistics are required to explore more number of transfer induced fission channels in these two reactions.

Chapter 7

Determination of neutron induced fission cross-sections

The study of neutron induced reactions on various targets not only provides a thorough understanding of the reaction mechanism of the formation and decay of compound nuclei but also has a tremendous potential in the applications in many areas of nuclear physics [33, 47, 98, 99, 100, 101, 102, 103]. One of the important applications of neutron induced cross-sections is its use in nuclear waste management programs. Fast neutron reactions have been proposed for the incineration of actinide materials, notably minor actinide isotopes which are produced in Th-U or U-Pu fuel cycles [33, 47, 98, 100, 101]. The spent fuel produced in the above cycles will be burnt in a dedicated reactor, where neutron reactions such as (n, f) or (n,2n) can be used to reduce the content of radio-toxic isotopes. The neutron induced reactions play an extremely important role in astrophysical nucleo-synthesis [99, 103].

Direct (n, f) cross-section measurements are sometimes very difficult due to non-availability of mono energetic neutron beam and/or short half-lives of the target nuclei. Under these circumstances, surrogate method first employed by Britt and Cramer in 1970 [41, 42] is a well celebrated method to measure the (n, f) cross sections indirectly. Later on, the 'Surrogate Ratio (SR)' method has been proposed by Plettner *et al.* [43]

for the same purpose. Recently, the SR method has been benchmarked and applied to determine several neutron induced fission cross-sections [33, 44, 45, 46, 47, 48, 49, 50]. Another method named 'Hybrid Surrogate Ratio (HSR)' method is also being used to determine the (n, f) cross-sections as done in Ref. [33] by Nayak *et al.*.

For ^{236}Np(n, f) reaction, there is no experimental data on fission cross-section beyond 4.32 MeV available in the literature. So, we propose to measure two surrogate reactions and determine the above cross sections following the HSR method. To obtain ^{236}Np(n, f) cross-section in the ratio approach one needs to have ^{238}Pu(n, f) cross-section as a reference. Hence the cross sections for ^{238}Pu(n, f) reaction have also been determined by measuring another set of surrogate reactions. However, in the second case the SR (instead of HSR) method was applied. For the ^{238}Pu(n, f) reaction, there exist some data by Resseler *et al.* [98] which were also obtained via the surrogate ratio approach. The present measurement aims to verify the literature data as well as extend the energy range for the (n, f) cross sections and finally use these cross sections as reference to determine the ^{236}Np(n, f) cross sections.

7.1 Surrogate methods

The 'Surrogate' methods can be classified into three categories: (i) absolute surrogate method (ii) surrogate ratio method and (iii) hybrid surrogate ratio method. According to Bohr's theory, the decay of the compound nucleus (CN) is independent of the details of its entrance channel. If α is the entrance channel and β is the exit channel of a desired compound nuclear reaction

$$\underbrace{a + A}_{\alpha} \longrightarrow C^* \longrightarrow \underbrace{b + B}_{\beta}$$

then the cross-section for this reaction can be written as

$$\sigma_{\alpha\beta}(E_x) = \sum_{J\pi} \sigma_\alpha^C(E_x, J, \pi) G_\beta^C(E_x, J, \pi) \tag{7.1}$$

where $\sigma_\alpha^C(E_x, J, \pi)$ is the formation cross-section of the compound nucleus 'C' at excitation energy E_x, spin J and parity π and $G_\beta^C(E_x, J, \pi)$ is the branching ratio for the decay of this compound nucleus 'C' into the desired exit channel β. The formation cross-section can be calculated by using optical model potential with reasonable accuracy, but decay probability calculation is quite uncertain.

If the above experimental measurement is not possible due to the target instability or any difficulty in the generation of the beam, then according to surrogate strategy, one chooses an alternate reaction with stable target and stable beam that are easily available and produce the desired compound nucleus with the same excitation energy. It is then followed by the measurements of the required decay channels. So the objective of the surrogate method is to determine these decay probabilities via an indirect measurement. The independence hypothesis of the compound nucleus decay allows us to replace $\sigma_\alpha^C(E_x, J, \pi)$ in Eq. (7.1) by a factor representing any other reaction route that we expect to form an equilibrated compound nucleus. In a surrogate experiment the desired compound nucleus C is produced via a surrogate direct reaction

$$\underbrace{d + D}_{\delta} \longrightarrow c + C^* \longrightarrow c + \underbrace{b + B}_{\beta}$$

and the decay of C is observed in coincidence with outgoing particle c. The formation probability of the desired compound nucleus 'C' in this reaction is $F_\delta^C(E_x, J, \pi)$. The decay probability of the desired compound nucleus into β channel is given by

$$P_{\delta\beta}(E_x) = \sum_{J\pi} F_\delta^C(E_x, J, \pi) G_\beta^C(E_x, J, \pi) \tag{7.2}$$

Experimentally it can be obtained from the following equation.

$$P_{\delta\beta}^{exp}(E_x) = \frac{N_{\delta\beta}}{N_\delta \epsilon_\delta} \tag{7.3}$$

where $N_{\delta\beta}$ is the number of coincidences between the direct reaction particles c and one of the decay products b or B. N_δ represents the total number of surrogate events. ϵ_δ is the efficiency in detecting the decay products of C.

The surrogate method works under the Weisskopf-Ewing limit of the Hauser-Feschback theory [31, 104] which says that the decay branching ratios are independent of J and π of the compound nucleus. So, in Eq. (7.1) and (7.2) we can replace $G_\beta^C(E_x, J, \pi)$ by $G_\beta^C(E_x)$. Now, from Eq. (7.2) we get $P_{\delta\beta}(E_x)$=$G_\beta^C(E_x)$ since $\sum_{J\pi} F_\delta^C(E_x, J, \pi)$=1. Consequently, combining Equations (7.1) and (7.3) we can write the expression for desired $\sigma_{\alpha\beta}(E_x)$ measured via surrogate reaction (δ channel) as

$$\sigma_{\alpha\beta}^{(\delta)}(E_x) = \sigma_\alpha^{CN}(E_x)\frac{N_{\delta\beta}}{N_\delta\epsilon_\delta} \tag{7.4}$$

This method is known as the absolute surrogate method. However, this method may sometimes introduce large errors to the (n, f) cross sections due to the systematic uncertainties in the decay yield measurements as well as model-calculated formation cross section for a single surrogate reaction. On the other hand, the surrogate ratio (SR) method is found to have an advantage over the absolute method. In SR method, the ratio of cross-sections of two reactions with different target-projectile combinations are considered where the cross-sections for one of the reactions are known and used as reference. While taking the ratio of the decay probabilities of the composite nuclei formed by two different reactions many systematic uncertainties with respect to theory as well as experiment are removed. In the SR method, the dependence on J and π is shown to disappear at CN excitation energies higher than 8 MeV [43]. It is also shown that the ratio is insensitive to the pre-equilibrium effects for (n, f) reactions. There are several instances where SR method has been found to be valid at excitation energy even below 8 MeV. Applying the above surrogate technique Lyles *et al.* [45] have obtained the cross section for $^{236}U(n, f)$ reaction which is comparable to the evaluated

ENDF/B-VII data in the neutron energy range E_n=3.5-20 MeV. The cross section below this energy i.e., $E_n \leq 3.5 MeV$ has the dependence on J^π of the compound nucleus. Similarly, Burke *et al.* [44] have obtained the cross sections for ^{237}U(n, f) reaction by measuring the surrogate reactions ^{238}U(α,α'f) and ^{236}U(α,α'f) in the neutron energy range E_n=0-20 MeV and the results are comparable (within the experimental uncertainty of 10%) to the previously measured data especially at low energy region (E_n=1-10 MeV). Using the same SR method, Goldblum *et al.* [47] have determined the cross sections for ^{230,231}Th(n, f) reactions at energies E_n=0.22-25.0 MeV and 0.36-10.0 MeV respectively. The results agree with the directly measured data very well for the respective (n, f) reactions.

In the present study, we propose to obtain the cross section for ^{238}Pu(n,f) reaction using the above SR method by measuring two surrogate reactions, namely, ^{235}U(^{6}Li,d)^{239}Pu and ^{232}Th(^{6}Li,d)^{236}U at beam energies of 44.4 MeV. In both these reactions the exit channels are same, i.e., deuterons are emitted. The number of outgoing deuterons along with the fission fragments of the residual composite nuclei (formed by the capture of α particles by the target) provides the probability of transfer induced fission decay channel. The excitation energies of the residual composite nuclei ^{239}Pu and ^{236}U formed in the above reactions are in the range of 18.6-27.6 MeV which is much higher than 8 MeV. So, the decay branching ratios are expected to be independent of J and π of the compound nucleus validating the Weisskopf-Ewing limit of the Hauser-Feschback theory. The reference reaction is taken to be ^{235}U(n, f) reaction whose cross sections are available in the literature from the direct measurement by M. Cance *et al.* [105, 106]. Now, the cross-section for ^{238}Pu(n, f) reaction can be deduced from the following relation.

$$\frac{\sigma^{^{238}Pu(n,f)}(E_x)}{\sigma^{^{235}U(n,f)}(E_x)} = \frac{\sigma^{^{239}Pu}(E_x)}{\sigma^{^{236}U}(E_x)} \frac{N_{d-f}}{N_d} \frac{N_d'}{N_{d-f}'} \tag{7.5}$$

Here, N_{d-f} and N'_{d-f} are the number of fission events occurring from the residual composite nuclei ^{239}Pu and ^{236}U respectively measured in coincidence with the deuterons (produced in the direct reactions). The corresponding inclusive deuteron yields are denoted by N_d and N'_d respectively. The compound nuclear formation cross-sections in n+^{235}U→^{236}U and n+^{238}Pu→^{239}Pu reactions at excitation energy E_x are denoted by $\sigma^{^{236}U}(E_x)$ and $\sigma^{^{239}Pu}(E_x)$ respectively whose values are obtained from the EMPIRE calculations.

In the third method, i.e., the hybrid surrogate ratio (HSR) method, two reactions are chosen from the same target-projectile combination. Two different reaction channels considered here, e.g., (^{6}Li,αf) and (^{6}Li,df) when ^{6}Li is a projectile. The choice of target-projectile combination is made in such a way that the above transfer reactions populate two nearby residual composite nuclei at same excitation energies. However, the distribution of the angular momenta of the respective composite nuclei populated by the capture of deuteron in the first reaction and α in the second reaction may be different. In general, the assumption of the independence of J and π in the calculation of the decay probability '$G^C_\beta(E_x, J, \pi)$' may not be true and in that case the HSR method cannot be applied. Therefore, one has to verify the validity of the above assumption for the concerned composite nuclei at the excitation energies formed by two surrogate reactions before this method can be applied to determine the corresponding (n, f) cross section.

In the second set of present measurements, we propose to determine ^{236}Np(n, f) cross-section using HSR method by measuring two surrogate reactions ^{235}U(^{6}Li,α)^{237}Np and ^{235}U(^{6}Li,d)^{239}Pu. Two residual composite nuclei (^{237}Np and ^{239}Pu) formed in the above two transfer reactions are the same as the compound nuclei formed in the n+^{236}Np and n+^{238}Pu reactions respectively. The ground state Q values (Q_{gg}) for these two surrogate reactions are 7.70 MeV and -6.72 MeV respectively. From the excitation energy calculation of a transfer reaction (E_x =Q_{gg}-Q_{opt}; Q$_{opt}$ = $E_{cm}(\frac{z_{1f}z_{2f}}{z_{1i}z_{2i}}$-1)) it can be noticed that the residual composite nuclei ^{237}Np and ^{239}Pu can be populated at overlapping excitation energies for two transfer channels when ^{6}Li is incident on ^{235}U with bombarding energy of $\sim$ 44.4 MeV. The spin distribution of the two composite nuclei, formed by ^{235}U(^{6}Li,α) and ^{235}U(^{6}Li,d) reactions respectively, are different though. The overlapping excitation energy of two composite nuclei is in the range of $\sim$ 16-28 MeV. At such excitation energies, the level density of the residual composite nuclei is very high and the fission decay probability will be independent of the angular momentum acquired by capturing the breakup/transferred fragment. But, the effect of J on fission decay probability can be significant for the higher chance fissions, e.g., $(n, 2nf)$ or$(n, 3nf)$ decays where the excitation energy available at the fission saddle point is very low. Assuming breakup of the projectile or transfer reaction to be due to peripheral collisions and the energy of deuteron (alpha) equal to one-third (two-third) of the beam energy, the angular momentum involved in ^{235}U(^{6}Li,α)^{237}Np and ^{235}U(^{6}Li,d)^{239}Pu reactions are calculated to be $J \sim 11\hbar$ and $23\hbar$ respectively. To investigate the dependence of J on fission decay probability in ^{236}Np(n, f) and ^{238}Pu(n, f) reactions detailed calculations using EMPIRE code[107] version-3.1 have been performed at neutron energy in the range of E_n=1-23 MeV. The results of the above calculations for J=5$\hbar$, 15$\hbar$ and 25$\hbar$ are shown as dashed, dash-dot-dot and solid line respectively in Fig. 7.1. As the neutron energy E_n increases beyond 10 MeV (the region of our interest), it can be observed that the difference in the fission probabilities corresponding to a $\Delta J \sim 10\hbar$ narrows down to $\leq$5%. Thus, the decay probabilities of the present composite nuclei have little dependence on the initial distribution of J. Hence one can use the HSR method to obtain the (n, f) cross-section from the above surrogate reactions within a small uncertainty contributed by the spin mismatch of the composite nuclei.

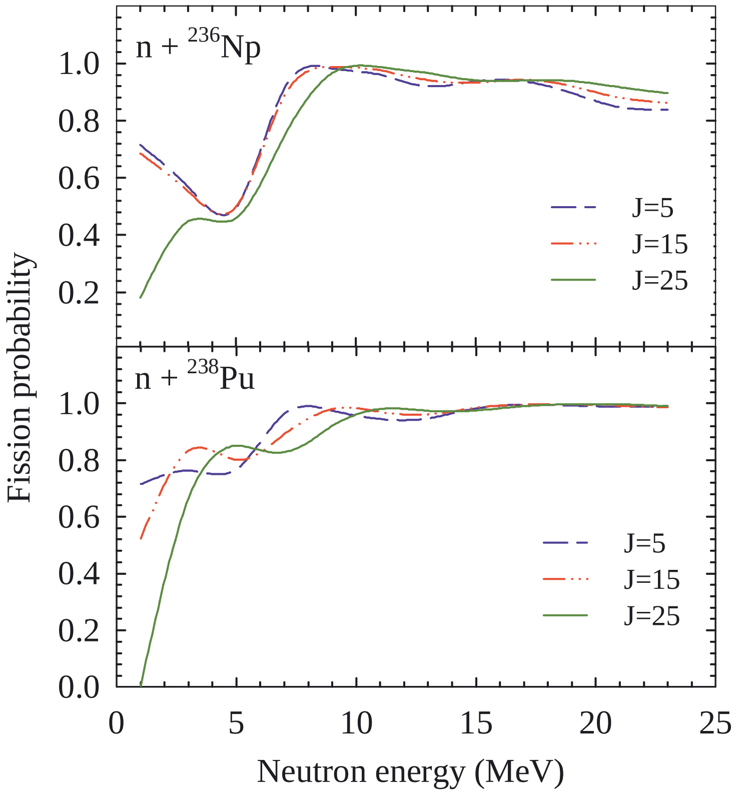

Figure 7.1: Fission decay probability in ^{236}Np(n, f) (upper panel) and ^{238}Pu(n, f) (lower panel) reactions calculated using EMPIRE code as a function of neutron energy with different compound-nucleus J values.

So, we can now use Eq. (7.4) and write the expression for ^{236}Np(n,f) reaction cross-section as:

$$\frac{\sigma^{^{236}Np(n,f)}(E_x)}{\sigma^{^{238}Pu(n,f)}(E_x)} = \frac{\sigma^{^{237}Np}(E_x)}{\sigma^{^{239}Pu}(E_x)} \frac{N_{\alpha-f}}{N_\alpha} \frac{N_d}{N_{d-f}} \tag{7.6}$$

Here, $N_{\alpha-f}$ and N_{d-f} correspond to the number of fission events measured in coincidence with outgoing direct reaction products α and d particles respectively. The inclusive α and d counts are denoted by N_α and N_d respectively. The compound nuclear formation cross-sections $\sigma^{^{237}Np}(E_x)$ and $\sigma^{^{239}Pu}(E_x)$ at excitation energy E_x, in the reaction n+^{236}Np→^{237}Np and n+^{238}Pu→^{239}Pu respectively, are obtained from the EMPIRE calculations. The cross-sections for $^{238}Pu(n,f)$ reaction can be used as reference which can either be obtained from the present measurements described above and/or the available indirect measurement by Ressler *et al.* [98].

7.2 Experiment and data analysis

Measurements were carried out using 44.4 MeV ^{6}Li beam from BARC-TIFR Pelletron accelerator facility in Mumbai. Targets used are: (i) 1.6 mg/cm^2 thick ^{235}U electro-deposited on 4.5 mg/cm^2 thick Ni-Cu backing and (ii) 1.3 mg/cm^2 thick self-supported ^{232}Th target. One telescope (ΔE-E) made of silicon surface barrier detectors, used to detect light charged particles, was kept at 80° angle with respect to the beam direction, when ^{235}U target was used. To study the other reaction (^{6}Li+^{232}Th) the telescope was kept at 70° angle with respect to beam direction because of lower grazing angle compared to the previous one. An aluminium foil of thickness ∼6.75 mg/cm^2 was placed in front of the particle telescope to stop the fission fragments entering the ΔE detector and prevent it from radiation damage. A ^{229}Th alpha source was used to calibrate the ΔE and E silicon detectors. Distance between each telescope and target

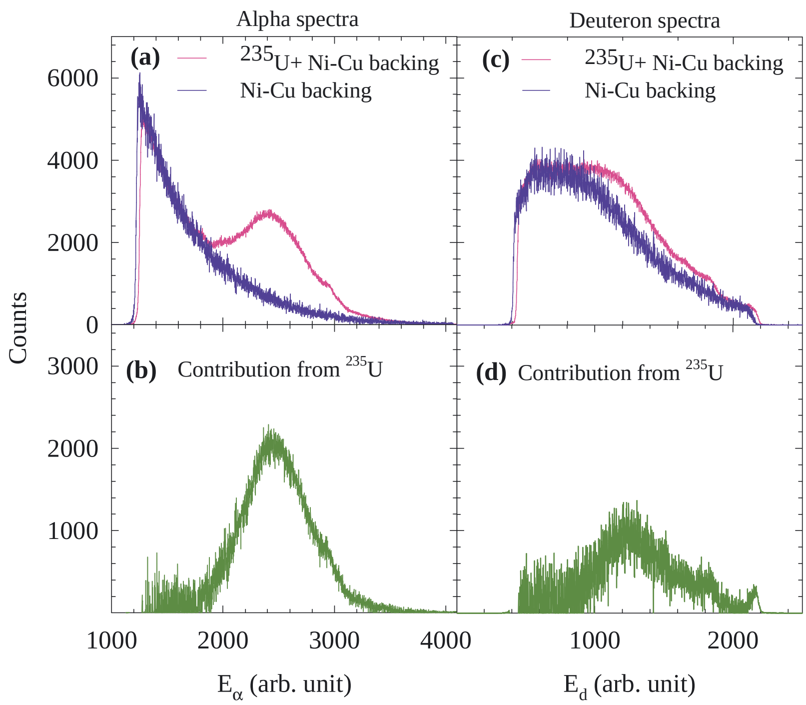

Figure 7.2: Typical alpha and deuteron spectra from ^{235}U + Ni-Cu backing (pink line) and only Ni-Cu backing (blue line) are shown in (a) and (c). Corresponding spectra only from ^{235}U target (green line) obtained from the difference of the above two contributions are shown in (b) and (d) respectively.

was 18.6 cm. A large area silicon detector (with a solid angle $\sim$ 33 msr and an angular coverage of 154°-166°) was used to detect fission fragments in the backward hemisphere. The fission detector was placed at a distance of 11 cm from the target centre. Two monitor detectors were placed at forward angles in order to monitor the stability of the beam. Particles were identified from the ΔE vs. (ΔE+E) plot. Since the particles reach the detectors after losing energy through Ni-Cu backing and aluminium foil, the respective energy losses have been calculated using SRIM programme [108] and the actual energy of the outgoing light charged particle has been reconstructed event by event.

Reactions with only Ni-Cu backing have been separately studied and light charged particle contributions from Ni-Cu backing have been estimated. As shown in Fig. 7.2 alpha and deuteron contributions (blue line) in the telescope from Ni-Cu backing have

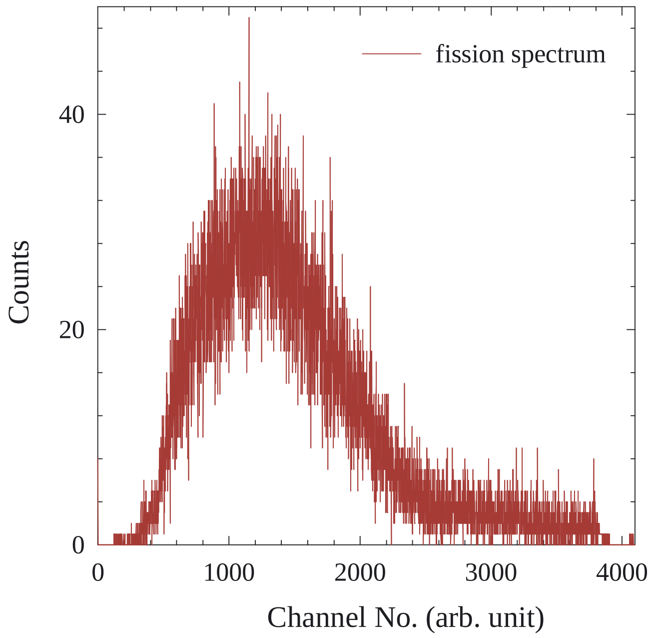

Figure 7.3: Typical fission spectrum obtained in coincidence with light charged particles in ^{6}Li+^{235}U reaction.

been subtracted out from the total (pink line) contribution (^{235}U + Ni-Cu backing) resulting in the pure alpha and deuteron contribution from ^{235}U target (green line). While subtracting the contribution of the target backing, the relative shift in the energy spectra due to Uranium thickness has been taken into account.

The time correlation between light charged particles and fission fragments has been recorded through a time-to-amplitude converter (TAC). A typical fission spectrum obtained in coincidence with light charged particle in ^{6}Li+^{235}U reaction has been shown in Fig. 7.3.

7.3 Determination of ^{238}Pu(n, f) cross-section

First we determined the cross sections for ^{238}Pu(n, f) reaction using the surrogate ratio (SR) method. These results, along with the data available from the literature, were later used as the reference reaction cross sections for determining the cross section of ^{236}Np(n, f) reaction using HSR method. The experimental data from the present mea-

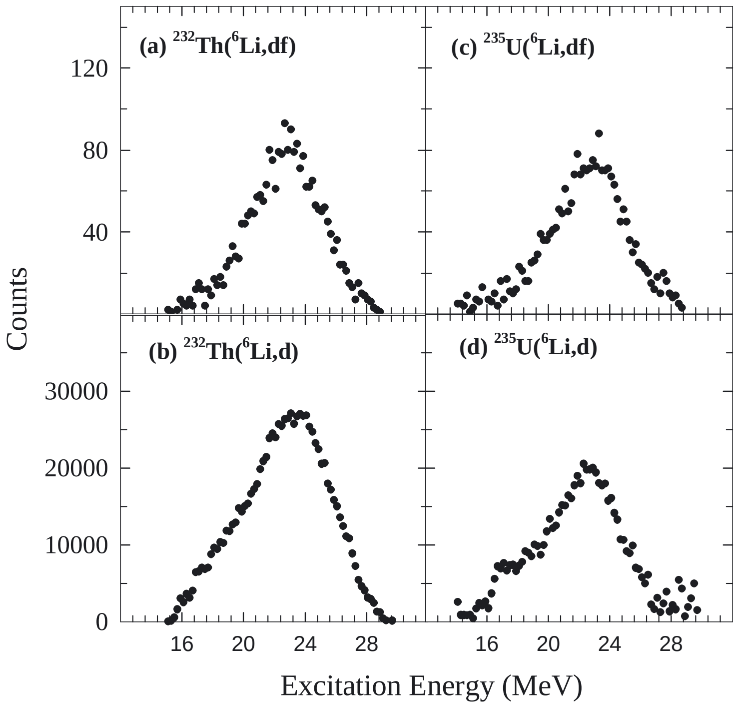

Figure 7.4: Deuteron spectra for (a,b) ^{232}Th(^{6}Li,d)^{236}U and (c,d) ^{235}U(^{6}Li,d)^{239}Pu transfer reactions respectively. Deuterons measured in coincidence with fission fragments for the respective reactions are shown in (a) and (c) and those in singles are shown in (b) and (d). Background from Ni-Cu backing is subtracted.

surements for ^{235}U(^{6}Li,df) and ^{232}Th(^{6}Li,df) transfer induced fission reactions which proceed through the excited fissioning nuclei ^{239}Pu and ^{236}U respectively were analyzed. The excitation energy of the desired composite nucleus formed in transfer reaction is calculated using the relation E_x=$(E_{\rm beam} - E_{\rm out} - E_{\rm recoil}) + Q$, where $E_{\rm out}$ is the energy of the outgoing particle, $E_{\rm recoil}$ is the recoil energy of the compound nucleus calculated from the recoil momentum and Q is the Q-value of the reaction.

If S_n is the neutron separation energy from a compound nucleus with mass number A and excitation energy E_x, the equivalent neutron energy can be written as $E_n = \frac{A}{A-1}(E_x - S_n)$. Neutron separation energies for the compound nuclei ^{236}U and ^{239}Pu are 6.54 MeV and 5.65 MeV respectively, using which the equivalent neutron energies are calculated.

Figure 7.4 shows the deuteron spectra obtained from ^{232}Th(^{6}Li,d)^{236}U and

^{235}U(^{6}Li,d)^{239}Pu reactions. The deuterons measured in coincidence with the fission fragments for the above two reactions correspond to the spectra of Fig. 7.4(a) and (c) respectively, whereas the deuterons measured in singles correspond to Fig. 7.4(b) and (d) respectively. In the spectra shown for ^{235}U(^{6}Li,d)^{239}Pu reaction, the background from the Ni-Cu backing has already been subtracted.

Following the expression given in Eq. (7.5), which was obtained from the SR method, the cross-sections for ^{238}Pu(n, f) reaction have been determined in the equivalent neutron energy range of 13.0 - 22.0 MeV. The results are shown in Fig. 7.5 as filled circles. The data measured by Ressler *et al* [98] are also shown in the figure as hollow circles. The data from the present measurements are found to be in good agreement with the ones by Ressler *et al.* in the overlapping energy region. Hence, one can now use the present ^{238}Pu(n, f) cross-sections along with the literature data as the reference to determine the ^{236}Np(n, f) cross-sections by HSR method.

The results of ENDF/B-VII.1 evaluations for ^{238}Pu(n, f) cross-sections have also been shown in Fig. 7.5 as a dashed line. It can be observed that the evaluated cross sections reproduce the low energy data very well but slightly underestimate the high energy data.

The EMPIRE calculations have been carried out to quantitatively understand the ^{238}Pu(n, f) cross section over the neutron energy range 1.0-25.0 MeV. The decay probabilities of the compound nuclei up to 4th chance fission i.e., the decay of ^{239,238,237,236}Pu nuclei have been included. The inner (V_a) and outer (V_b) fission barrier parameters of a double humped fission barrier for the ^{239,238,237}Pu isotopes have been taken from the Reference Input Parameter Library (RIPL-3) [109] which is a standard library of fission barrier parameters for actinides. The required fission barrier heights for the ^{236}Pu isotope is not available in RIPL-3. Hence it has been calculated from the barrier formula

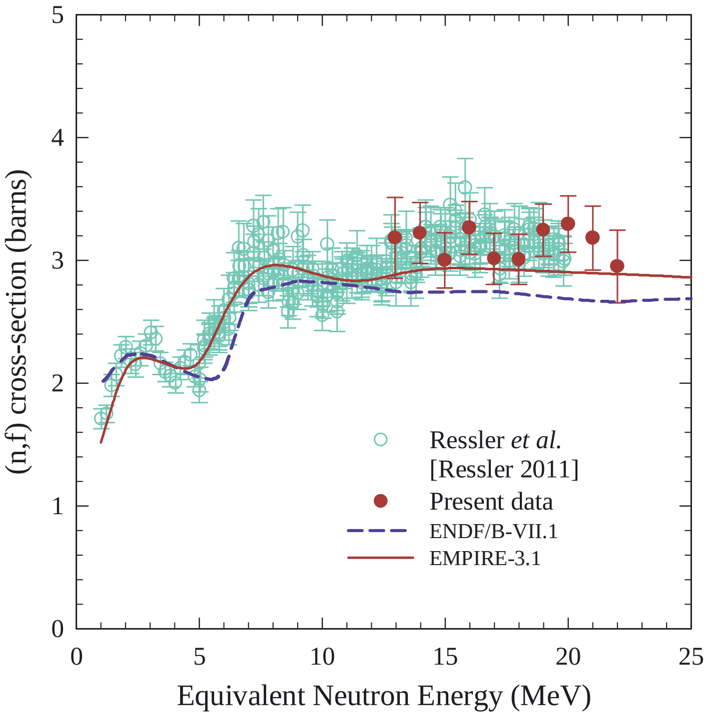

Figure 7.5: Determined ^{238}Pu(n, f) cross-sections (filled circle) along with the data (hollow circle) measured by Ressler *et al.* (Ressler 2011:[98]). Solid and dashed lines correspond to the results of EMPIRE calculations and ENDF/B-VII.1 evaluations respectively.

Table 7.1: Barrier heights used for Pu isotopes in EMPIRE-3.1 calculations.

Isotopes	Standard		Modified	
	V_a	V_b	V_a	V_b
^{239}Pu	6.20	5.70	6.40	5.80
^{238}Pu	5.60	5.10	5.60	5.10
^{237}Pu	5.10	5.15	4.50	4.15
^{236}Pu	5.71	4.91	4.70	4.90

(BF) as given in Ref. [50]. The final calculations have been made after slight modifications of the barrier parameters to explain the measured (n, f) cross sections. The initial and final barrier parameters are given in Table 7.1. The results of the EMPIRE calculations with modified barrier parameters are shown as a solid line in Fig. 7.5.

7.4 Determination of ^{236}Np(n, f) cross-section

Here, we analyze the raw data for ^{235}U(^{6}Li,αf) and ^{235}U(^{6}Li,df) transfer induced fission reactions which proceed through excited fissioning nuclei ^{237}Np and ^{239}Pu respectively. The excitation energies of the desired compound nuclei have been obtained following the same procedure mentioned earlier. Overlapping excitation energies of ^{237}Np and ^{239}Pu desired compound nuclei have been found to be in the range of 16.6 - 28.6 MeV. The inclusive as well as exclusive (in coincidence with fission) spectra for alpha and deuteron yields obtained from the above two reactions are shown in Fig. 7.6. Neutron separation energies for the compound nuclei ^{237}Np and ^{239}Pu are 6.57 MeV and 5.65 MeV respectively, using which the equivalent neutron energies are calculated. The excitation energy of the residual composite nuclei and the equivalent neutron energy have been calculated using the expression mentioned in the previous section for every 1 MeV bin of the spectra. Now using the formula mentioned in Eq. (7.6) the desired reaction cross-sections have been determined for equivalent neutron energy in the range of 9.9 - 22.0 MeV (Fig. 7.7).

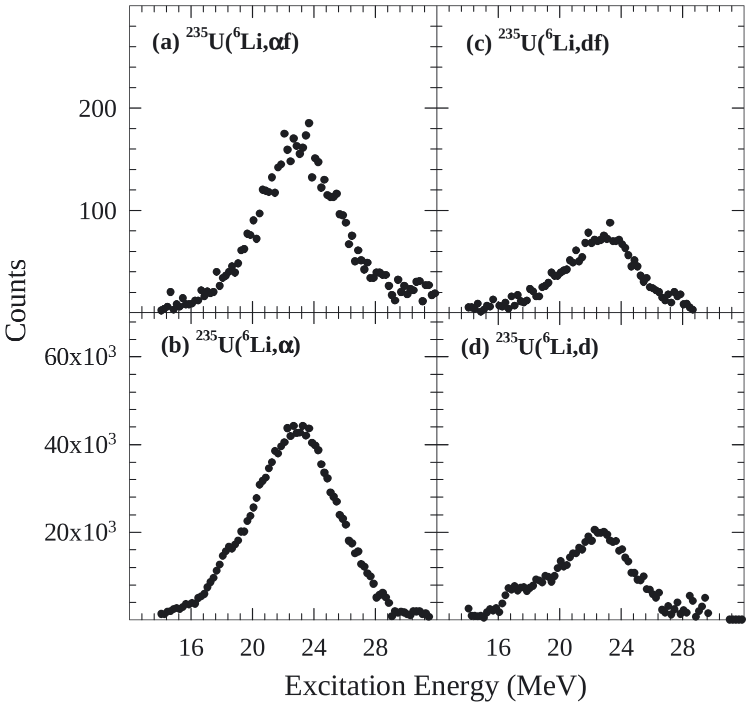

Figure 7.6: Coincident and inclusive spectra for (a,b) alpha and (c,d) deuteron respectively in ^{6}Li+^{235}U reaction.

The EMPIRE calculations for ^{236}Np(n, f) cross section have been carried out at the neutron energy in the range of E_n=1.0-24.0 MeV. Similar to the ^{238}Pu(n, f) reaction, the calculations for the present system also consider the decay of the compound nuclei up to 4th chance fission i.e., the decay of ^{237,236,235,234}Np nuclei. The initial barrier parameters for ^{237}Np and ^{236}Np isotopes have been taken from RIPL-3 and those for the ^{235}Np and ^{234}Np isotopes have been calculated from the barrier formula (BF)[50]. Modified barrier parameters have been used to get a best fit to the experimental data. The Initial and final fission barrier parameters used in these calculations are given in Table 7.2. The EMPIRE calculations with the initial as well as the modified barrier parameters (dotted and solid lines) reproduce the present data for ^{236}Np(n, f) very well within the experimental uncertainty. However, a reduced value of 'Kdis' parameter [from 6.0 (default) to 2.5] of discrete transitional state of ^{236}Np nucleus has been used in the EMPIRE calculations in order to reproduce both the low energy data of Ref. [41]

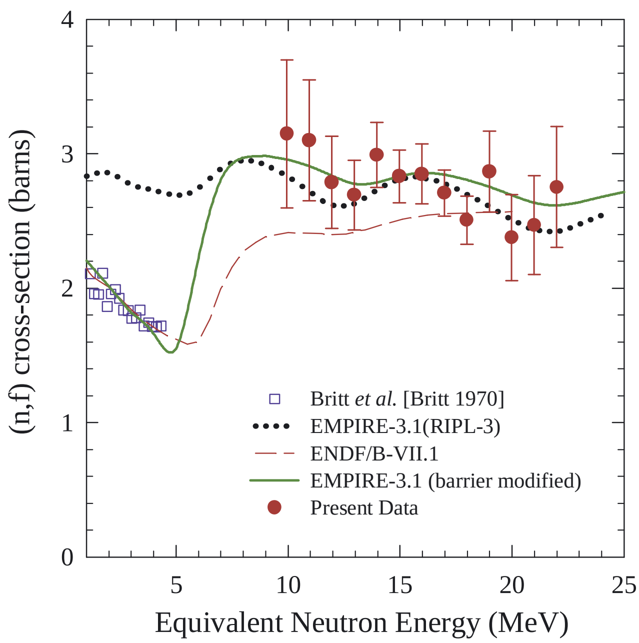

Figure 7.7: ^{236}Np(n, f) cross-section as a function of equivalent neutron energy. Open squares are the existing data measured by H.C. Britt *et al.*(Britt 1970:[41]). Dotted and solid lines represent the EMPIRE-3.1 calculations.

Table 7.2: Barrier heights used for Np isotopes in EMPIRE-3.1 calculation.

Isotopes	Standard		Modified	
	V_a	V_b	V_a	V_b
^{237}Np	6.00	5.40	6.45	5.40
^{236}Np	5.90	5.40	5.90	5.40
^{235}Np	5.88	5.51	6.30	5.70
^{234}Np	6.20	5.68	6.40	5.70

as well as the present data (solid line). The ^{236}Np(n, f) cross-sections have also been evaluated using ENDF/B-VII.1 (dashed line) which are found to be in good agreement with the low energy data measured by H.C. Britt *et al.* [41], but they are slightly under-predicted compared to the present data (Fig. 7.7) at intermediate energies.

To explain the measured data on (n, f) cross sections, the EMPIRE calculations so far have been made by adjusting only the fission barrier parameters of the residual composite nuclei. In order to look for the sensitivity of (n, f) cross section to other parameters e.g., level density of the composite nuclei, the EMPIRE calculations have been carried out using several combinations of input parameters on fission barriers

Table 7.3: Different sets of parameters on fission barriers and level density of the residual composite nuclei used in EMPIRE calculations to see the sensitivity of these parameters.

Set	Fission Barriers	Level density	Line type
A	default	default	short-dashed
B	modified (same as Table 7.2)	default	long-dashed
C	default	increased by 5%	dash-dotted
D	modified	decreased by 5%	solid

as well as level density that provide reasonable reproduction of the measured cross sections. Fig. 7.8 shows the results of the above calculations for ^{236}Np(n, f) cross section with four sets of parameters (set 'A' -'D') as described in the Table 7.3. Comparing the EMPIRE results with parameter set 'A' (default values) to those for set 'B' (modified barriers) and 'C' (modified level density) one can find that the (n, f) cross sections are more sensitive to the fission barrier parameters than the level density, particularly at neutron energies $E_n \leq 5$ MeV. Best results, as represented by a long dashed line and a solid line in Fig. 7.8, have been obtained respectively with parameter set 'B' with modified barriers and set 'D' with modified level density as well as fission barriers. In set 'D', the level density has been reduced by 5% and accordingly the fission barriers have been readjusted (slightly different from Table 7.1) to get the best fit to the present data at high energy as well as the literature data at low energy.

7.5 Summary

The fission fragments emitted at backward angles are measured in coincidence with the light charged particles emitted around the grazing angles for ^{6}Li+^{235}U,^{232}Th reactions at a bombarding energy of 44.4 MeV. Surrogate methods have been used to obtain the neutron induced fission cross sections for ^{238}Pu and ^{236}Np target nuclei at neutron energies in the range of ~9.9-22.0 MeV. The cross sections for ^{238}Pu(n, f) reaction have

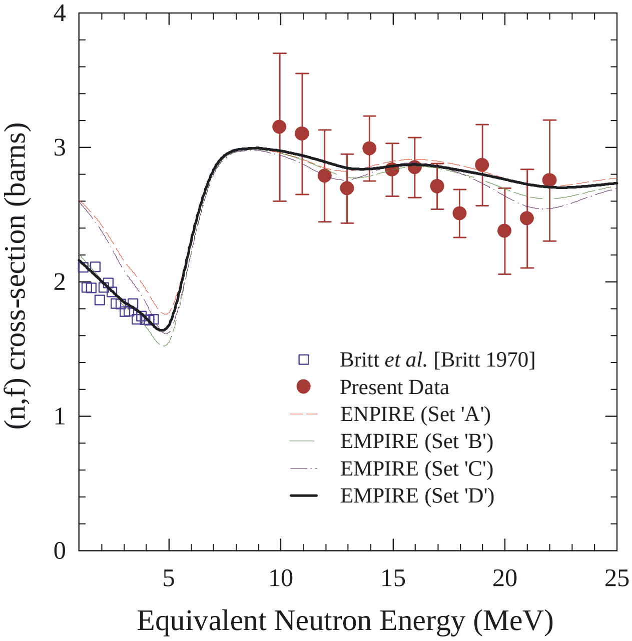

Figure 7.8: EMPIRE predictions for ^{236}Np(n,f) cross-section as a function of neutron energy using four different sets of parameters of nuclear level density and fission barriers. Open squares are the existing data measured by H.C. Britt *et al.*(Britt 1970:[41]). Dotted and solid lines represent the EMPIRE-3.1 calculations.

been determined for equivalent neutron energy of 13.0 - 22.0 MeV employing 'Surrogate Ratio' method in which the ratio of the exclusive (coincidence) to inclusive (singles) yields of the light charged particles measured in two reaction channels i.e., ^{235}U(^{6}Li,df) and ^{232}Th(^{6}Li,df) is used. The ^{235}U(n,f) reaction, for which the cross-section data is available in the literature, has been used as a reference reaction. The cross sections thus obtained for ^{238}Pu(n,f) reaction are found to be in good agreement with the data available in the literature at the overlapping energy region.

Similarly, the cross sections for ^{236}Np(n,f) reaction have been determined for equivalent neutron energy of 9.9 - 22.0 MeV employing 'Hybrid Surrogate Ratio' method where the yields from two other reaction channels i.e.,^{235}U(^{6}Li,αf) and ^{235}U(^{6}Li,df) reactions have been used. The reference reaction for the above method has been chosen to be ^{238}Pu(n,f) reaction for which the cross-sections from the literature along with the ones obtained from the present measurements are utilized.

The EMPIRE calculations with default as well as modified parameters are found to reproduce the present data for ^{236}Np(n, f) cross sections very well. However, the calculations with default parameters do not reproduce the literature data at low energy. A reduced value of 'Kdis' parameter of discrete transitional state of ^{236}Np nucleus, from 6.0 (default) to 2.5, is found to provide a good description of both low as well as high energy data. The calculations also show that the (n, f) cross sections are more sensitive to fission barrier parameters than to the level density parameters of the compound nuclei. The ENDF/B-VII.1 evaluated cross-sections for both ^{238}Pu(n, f) and ^{236}Np(n, f) reactions are found to be in good agreement with the data at low energies but they are on an average slightly lower compared to the present cross sections in the measured energy range. An improvement in the ENDF evaluations may be required for a consistent description of the above (n, f) cross sections for the entire energy range of the experimental data.

Chapter 8

Summary and Conclusions

The present thesis work includes the development of two MWPC detectors and several exclusive measurements that include the coincidence between projectile like fragments (PLFs) and fission fragments (FF) in reactions involving weakly bound projectiles and actinide targets to investigate the effect of transfer or projectile breakup on fission dynamics, particularly on fission observables like FF angular distributions, FF mass distributions and FF folding angle distributions. As an application of projectile breakup fragment induced fission reaction and using the principle of a surrogate reaction, a few neutron induced cross-sections have also been measured. The results of these studies are summarized below.

8.1 Summary

1. Two multiwire proportional counter (MWPC) detectors, similar to the one developed by Breskin [53, 54], have been developed in-house and tested successfully with ^{229}Th α source and ^{252}Cf fission source. The detectors are also used to derive FF mass distribution in ^{10,11}B + ^{238}U reactions.

2. Inclusive and exclusive FF angular distributions have been measured at three near barrier projectile energies for ^{6}Li+^{232}Th system. The measured anisotropies

for inclusive fission are found to be larger than the ones from SSPM predictions. FF anisotropies for transfer or breakup induced fission channels have been exclusively measured to investigate the role of breakup or transfer induced fission behind the enhancement of inclusive FF angular anisotropy, if any. It is found that the anisotropies of the FF in coincidence with different PLF, with respect to the composite nuclei recoil directions, are of the same order or slightly more than the inclusive anisotropy at the measured energies. However, the overall anisotropy, estimated by considering the PLF emission in all possible angles, is found to be either less or equal to the inclusive anisotropy. Therefore we concluded that breakup or transfer induced fission may not be playing any role for the enhancement. Further, to resolve the above discrepancy between the measurement and SSPM model, the role of entrance channel K-state distribution was investigated and finally the inclusive anisotropy could be successfully explained by ECD (entrance channel dependent) K state model.

3. The FF folding angle distributions and FF mass distributions in coincidence with PLF have been carried out on ^{6,7}Li+^{238}U systems at near barrier energies to investigate the role of breakup or transfer induced fission behind the (i) enhancement of the width of folding angle distributions and (ii) enhancement of the ratio of asymmetric to symmetric components of the mass distributions as previously conjectured for the same reactions [16]. It is observed that the peaks of the folding angle distributions corresponding to the dominant transfer- or ICF-fission channels are at same positions where additional kinks were observed in inclusive fission at below-barrier energies. This confirms that the presence of the kinks and the enhancement of the width of FF folding angle distributions at sub-barrier energies is due to the transfer- or ICF-fission channels. Again, the

peak to valley ratios of the mass distributions for the fission fragments in coincidence with PLFs like α, t, d and p are much larger than the ones for inclusive fission fragments at any particular projectile energy. It provides a direct confirmation that the contamination of transfer- or ICF-fission with CF-fission is the prime factor behind the enhancement in P:V ratio observed for inclusive fission compared to CF-fission.

The peak to valley ratios of FF mass distributions for ^{241,242,243,244}Pu and ^{240,241}Np nuclei, populated in these multi-nucleon transfer or ICF channels in the ^{6,7}Li+^{238}U reactions, have been compared with the existing literature data and calculations using GEF code. It is found that modified value of shell correction parameter for symmetric fragments describe the data better over the wide range of excitation energies, implying that shell correction parameter for symmetric fragments play an important role in fission dynamics.

From the same measurements, the cross sections for individual transfer-induced fission or incomplete-fusion fission channels in ^{6,7}Li+^{238}U reactions have been measured using the "fission-fragments and light-charged-particle coincidence" technique. The cross-sections for ICF followed by d-capture and t-capture for ^{6}Li and ^{7}Li projectile respectively, have been found to be the most significant channels at all the measured energies. Now, the ratio of ICF to TF at above barrier energies for ^{6}Li(^{7}Li)+^{238}U reaction was found to be $\sim$30% (20%) which is of same order as the complete fusion suppression factor commonly observed in reactions involving weakly bound projectile ^{6}Li(^{7}Li). A systematic comparison shows that the energy dependence of the ratio of ICF to TF for the present systems are consistent with the trend of several other systems available in the literature. The ratio of TF cross sections for ^{6}Li to that of ^{7}Li involving same target is also found to increase with the decrease in energy at sub-barrier energies. This result along with the previous result (ICF to TF ratio) manifests the effect of projectile breakup threshold. The mass-distributions for TF fission, simulated by overlapping the distributions for CF-fission and different ICF-fission channels with appropriate weight factors proportional to the measured CF and ICF cross-sections, quantitatively explain the difference in the peak to valley ratios between TF- and CF-fission for the present systems.

4. The FF Mass distributions in ^{10,11}B + ^{238}U reactions have been obtained using two MWPC detectors developed in-house. The excitation energy dependent width of the mass distributions in ^{11}B + ^{238}U reaction matches closely with the ones for ^{11}B + ^{235}U system [95] . The mass distributions are also consistent with the ones obtained from GEF code. It is interesting to note that a single Gaussian could not fit properly the mass distributions for ^{11}B + ^{238}U reaction at all the measured energies. The fits using two Gaussians provide much better fit even at the highest beam energy (with equivalent CN excitation energy of $\sim$45 MeV). This implies that the shell effect does not wash away even at the excitation energy of 45 MeV. The GEF predictions corroborate with the experimental results. The mass distribution in coincidence with α in ^{11}B + ^{238}U reaction has been obtained at one energy, but with limited statistics. Further measurements in these two reactions with much larger incident flux are necessary to explore other transfer induced fission channels with relatively lower probabilities.

5. The fission fragments are measured in coincidence with the light charged particles for ^{6}Li+^{235}U,^{232}Th reactions at a bombarding energy of 44.4 MeV to obtain the neutron induced fission cross sections for ^{238}Pu and ^{236}Np target nuclei. The cross sections for ^{238}Pu(n, f) reaction have been determined for equivalent neutron

energy of 13.0 - 22.0 MeV employing 'Surrogate Ratio' method in which the ratio of the exclusive (coincidence) to inclusive (singles) yields of the light charged particles measured in two reaction channels i.e., ^{235}U(^{6}Li,df) and ^{232}Th(^{6}Li,df) is used. The ^{235}U(n, f) reaction, for which the cross-section data is available in the literature, has been used as a reference reaction. The cross sections thus obtained for ^{238}Pu(n, f) reaction are found to be in good agreement with the data available in the literature at the overlapping energy region.

Similarly, the cross sections for ^{236}Np(n, f) reaction have been determined for equivalent neutron energy of 9.9 - 22.0 MeV employing 'Hybrid Surrogate Ratio' method where the yields from two other reaction channels i.e.,^{235}U(^{6}Li,αf) and ^{235}U(^{6}Li,df) reactions have been used. The reference reaction for the above method has been chosen to be ^{238}Pu(n, f) reaction for which the cross-sections from the literature along with the ones obtained from the present measurements are utilized. The measured cross-sections are compared with the results obtained from ENDF evaluation and EMPIRE calculations.

8.2 Conclusions

The effect of projectile breakup or nucleon transfer on fission dynamics in reactions involving weakly bound projectiles and actinide targets are already known in the literature and some of these effects have been explained qualitatively. However, the present thesis work focusses on finding out the quantitative explanations of these effects by carrying out exclusive measurements of the transfer/breakup fission events. The results of these studies led to several interesting conclusions.

For example, we concluded that the enhancement in fission fragments angular anisotropy compared to statistical model prediction is not due to breakup or transfer effect. The enhancement in experimental anisotropy could be explained using ECD k-state model calculation.

On the other hand, positive effect of breakup or transfer induced fission on inclusive FF mass and folding angle distributions have been concluded. Breakup or transfer induced fission is found to be responsible for increasing the peak to valley ratio of inclusive FF mass distributions at near barrier energies and also for enhancing the width of the folding angle distributions at below barrier energies.

In addition, fission dynamics of few nuclei which can not be populated using stable target and projectile, have been studied in the present thesis works. Shell effect for symmetric fission channel have been found to play a crucial role in the fission dynamics. In fact the accurate value of shell correction parameter for symmetric fission channels for few fissioning nuclei namely, ^{240,241}Np and ^{241,242,243,244}Pu have been determined.

Further, incomplete fusion cross-sections have been determined from the present coincidence measurement which may be a powerful tool to measure ICF cross-sections and may be complementary to the widely used gamma counting technique. The measured ICF cross-sections explain reasonably well the complete fusion suppression factors which is a common characteristics of the reactions involving weakly bound projectiles.

From one of the coincident measurements, fast neutron induced fission cross-sections useful for Generation IV reactor have been measured.

The present thesis works also include development of two MWPC detectors, which are primary tools to measure fission fragments and investigate fission dynamics at energies around the Coulomb barrier.

8.3 Future Outlook

In the present thesis work, we have seen the immense importance of breakup or transfer induced fission from different perspectives. The cross-section for breakup or transfer induced fission being low, we need very large detector set up to measure such kind of reactions. Sometimes, few important aspects may be missed out if the detector angular coverage is small. For example, to measure the angular anisotropy in the breakup or transfer induced fission fragment angular distribution, we detected fission fragments and outgoing PLF in the same reaction plane. However, the correlation between FF and PLF in the out-of-plane may differ from the in-plane correlation. We propose to make further investigation to bring out the out-of-plane correlation in reactions involving weakly bound projectiles and actinide targets, e.g., ^{6,7}Li+^{238}U,^{232}Th.

In the present thesis work we have learned that multinucleon transfer reaction is a powerful tool to study fission dynamics involving exotic beam. This technique can be exploited to study many new reactions simulating other unstable beams.

Employing surrogate method we plan to measure neutron induced fission cross sections for new reactions which have not been measured yet but are very important and useful for the design of the Generation IV nuclear reactors.

To fix the shell correction parameters at symmetry for predicting fission fragment mass distribution for any system a systematic study may be carried out for a large number of systems by comparing the theoretical results with the experimental data.

Appendix A

A.1 Proposition 1

Conversion from lab to centre of mass frame:

Methods: Let us assume that the velocities in centre of mass frame is equal (the case for symmetric fission), which is shown by velocity vectors V_f' in Fig. A.1. The corresponding velocity vectors in lab frame are given by V_1 and V_2. The angle between one of the velocity vector and beam axis in lab and centre-of-mass frame are given by θ_L and θ_{CM}. The recoil velocity of the fissioning nucleus in lab frame is denoted by V_{rec}.

Using the laws of triangle, one can write

$$\frac{\sin(\theta_{CM} - \theta_L)}{\sin\theta_L} = \frac{V_{rec}}{V_f'} = x \tag{A.1}$$

In case of small difference in θ_L and θ_{CM}, one can write $\sin(\theta_{CM} - \theta_L) \equiv \theta_{CM} - \theta_L$. Therefore, the above equation (A.1) gets simplified to

$$\theta_{CM} = \theta_L + x\sin\theta_L \tag{A.2}$$

Thus one can convert the lab angle to centre-of-mass angle, once the velocity of the recoiling nucleus (V_{rec}) and velocity of one of the fragments (V_f') in centre-of-mass frame are known. Here, V_{rec} and V_f' can be obtained from 2-body kinematics and Violas' systematics respectively. Another important conversion, i.e. solid angle conversion

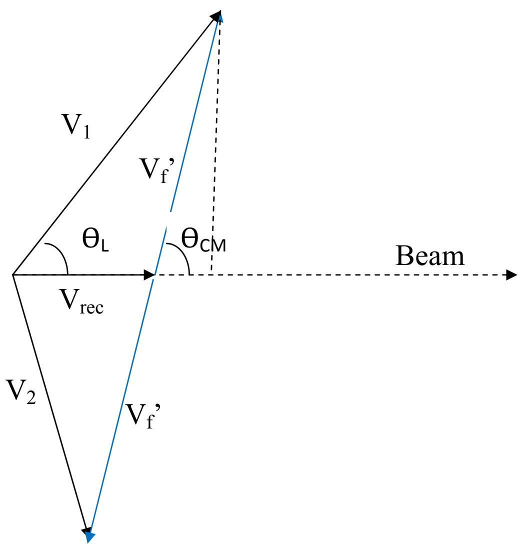

Figure A.1: Schematic velocity diagram in Lab and centre-of-mass frame

between these two frames is always required to transform cross-sections from lab to centre-of-frame. Cross-sections in lab and COM frame are related by

$$\sigma_L d\Omega_L = \sigma_{CM} d\Omega_{CM} \tag{A.3}$$

So from lab to COM conversion of cross-sections, the required factor is $\frac{d\Omega_L}{d\Omega_{CM}} = \frac{d(\cos\theta_L)}{d(\cos\theta_{CM}})$, which can be determined from the equations written as below.

$$V_1 \sin\theta_L = V_f' \sin\theta_{CM} \tag{A.4}$$

$$V_1 \cos\theta_L = V_f' \cos\theta_{CM} + V_{rec} \tag{A.5}$$

Dividing the above two equations, one can write

$$\tan\theta_L = \frac{V_f' \sin\theta_{CM}}{V_f' \cos\theta_{CM} + V_{rec}} = \frac{\sin\theta_{CM}}{x + \cos\theta_{CM}} \tag{A.6}$$

So from the equation, one can write the equations for $\cos\theta_L$ and $\frac{d(\cos\theta_L)}{d(\cos\theta_{CM}})$ as below

$$\cos\theta_L = \frac{x + \sin\theta_{CM}}{(1 + x^2 + 2x\cos\theta_{CM})^1/2} \tag{A.7}$$

$$\frac{d(\cos\theta_L)}{d(\cos\theta_{CM})} = \frac{1 + x\cos\theta_{CM}}{(1 + x^2 + 2x\cos\theta_{CM})^3/2} \tag{A.8}$$

Hence the conversion formula from lab to COM frame can be directly written as

$$\sigma_{CM} = \frac{1 + x\cos\theta_{CM}}{(1 + x^2 + 2x\cos\theta_{CM})^3/2}\sigma_L \tag{A.9}$$

A.2 Proposition 2

If anisotropy in the rest frame of a recoiling nuclei is A_2, after averaging over out-of-plane recoil directions (ϕ_{recoil}), the anisotropy with respect to beam direction is reduced by the factor $P_2(\cos\theta_{recoil})$.

Proof:

The angular distribution of fission with respect to the rest frame of recoil nuclei, as measured in the reaction plane, can be written in terms of 2nd order Legendre polynomial P_2 as

$$W(\theta') = 1 + A_2 P_2(cos\theta') \tag{A.10}$$

(This is equivalent to writing 1 + a $cos^2\theta'$, and one can relate the coefficients and the normalization of the two expressions to each other). Earlier measurements on transfer induced fission show that it is a very good approximation to let this angular distribution be valid irrespective of whether the fission fragments are emitted in the reaction plane or not. However, to estimate the contribution to fission from all transfer events, irrespective of whether the projectile-like fragment has been observed or not, one has to consider all directions of the recoiling nucleus for a particular value of recoil angle θ_{recoil} relative to the beam axis (see Fig. A.2). Thus, one must average over (i) Φ_{recoil} (the small circle making a solid angle sphere indicated by the dash-dotted blue curve in Fig. A.2) for a particular θ_{recoil} centered at the beam axis, and then over (ii) θ_{recoil} with appropriate weight factor. Now, one can apply the relation for spherical harmonics, in this case for $\ell = 2$:

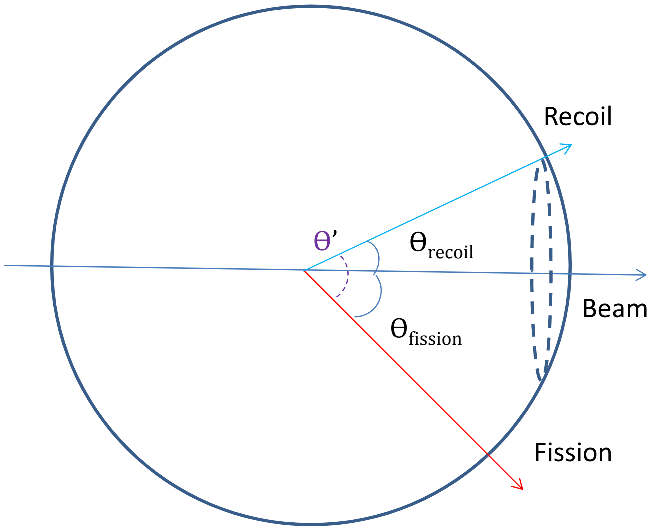

Figure A.2: Schematic diagram showing the angles of fission fragment emission 'θ_{fission}' and recoils 'θ_{recoil}'. The dotted blue line represents possible out-of-plane recoil angles and θ' is the angle between the recoil direction and one of the fission fragments.

$$P_\ell(cos\theta') = \frac{4\pi}{2\ell+1}\sum_m Y^*_{2m}(\theta_{\text{recoil}}, \Phi_{\text{recoil}}) \times Y_{2m}(\theta_{\text{fission}}, \Phi_{\text{fission}})$$

Averaging over the small circle on the figure corresponds to averaging over the angle Φ_{recoil} which selects the term m = 0 in the sum, and one ends up with the second Legendre polynomial when inserting into the angular distribution after averaging:

$$W(\theta_{\text{fission}}) = 1 + A_2 P_2(cos\theta_{\text{recoil}})P_2(cos\theta_{\text{fission}}) \tag{A.11}$$

Thus, one sees that this averaging over directions of the recoil restores the symmetry with respect to the beam axis. Thus, in the rest frame of recoil nucleus, the angular distribution coefficient with respect to the beam axis is related to the one of the in-plane distribution by just an extra factor $P_2(\cos\theta_{\text{recoil}})$.

Bibliography

[1] O. Hahn and F. Strassmann, Naturwiss. **27**, 11 (1939).

[2] L. Meitner and O. Frisch, Nature **143**, 239 (1939).

[3] N. Bohr and J. Wheeler, Phys. Rev. **56**, 426 (1939).

[4] K. Schmidt, B. Jurado, C. Amouroux, and C. Schmitt, Nucl. Data Sheets **131**, 107 (2016).

[5] V. M. Strutinsky, Nucl. Phys. A **95**, 420 (1967).

[6] V. M. Strutinsky, Nucl. Phys. A **122**, 1 (1968).

[7] C. Ngo, Prog. Part. Nucl. Phys. **16**, 139 (1986).

[8] A. C. Berriman, D. J. Hinde, M. Dasgupta, C. R. Morton, R. D. Butt, and J. O. Newton, Nature (London) **413**, 144 (2001).

[9] E. Williams, D. J. Hinde, M. Dasgupta, R. du Rietz, I. P. Carter, M. Evers, D. H. Luong, S. D. McNeil, D. C. Rafferty, K. Ramachandran, et al., Phys. Rev. C **88**, 034611 (2013).

[10] V. S. Ramamurthy and S. S. Kapoor, Phys. Rev. Lett. **54**, 178 (1985).

[11] U. L. Businaro and S. Gallone, Nuovo Cimento **5**, 315 (1957).

[12] S. Kailas, Phys. Rep. **284**, 381 (1997).

[13] A. Parihari, S. Santra, A. Pal, N. L. Singh, K. Mahata, B. K. Nayak, R. Tripathi, K. Ramachandran, P. K. Rath, R. Chakrabarti, et al., Phys. Rev. C **90**, 014603 (2014).

[14] S. Appannababu, R.G.Thomas, L.S.Danu, P.K.Rath, Y.K.Gupta, B.V.John, B.K.Nayak, D.C.Biswas, A.Saxena, S.Mukherjee, et al., Phys. Rev. C **83**, 067601 (2011).

[15] I. Itkis, A. Bogacheva, A. Chizhov, D. Gorodisskiy, M. Itkis, G. Knyazheva, N. Kondratiev, E. Kozulin, L. Krupa, S. Mulgin, et al., Phys. Letters B **640**, 23 (2006).

[16] S. Santra, A. Pal, P. K. Rath, B. K. Nayak, N. L. Singh, D. Chattopadhyay, B. R. Behera, V. Singh, A. Jhingan, P. Sugathan, et al., Phys. Rev. C **90**, 064620 (2014).

[17] P. K. Rath, S. Santra, N. L. Singh, R. Tripathi, V. V. Parkar, B. K. Nayak, K. Mahata, R. Palit, S. Kumar, and S. Mukherjee, Phys. Rev. C **79**, 051601(R) (2009).

[18] L. F. Canto, P. R. S. Gomes, R. Donangelo, J. Lubian, and M. S.Hussein, Phys. Rep. **596**, 1 (2015).

[19] C. S. Palshetkar, S. Santra, A. Chatterjee, K. Ramachandran, S. Thakur, S. K. Pandit, K. Mahata, A. Shrivastava, V. V. Parkar, and V. Nanal, Phys. Rev. C **82**, 044608 (2010).

[20] V. V. Parkar, R. Palit, S. K. Sharma, B. S. Naidu, S. Santra, P. K. Joshi, P. K. Rath, K. Mahata, K. Ramachandran, and T. Trivedi, Phys. Rev. C **82**, 054601 (2010).

[21] M. K. Pradhan, A. Mukherjee, P. Basu, A. Goswami, R. Kshetri, S. Roy, P. R. Chowdhury, M. SahaSarkar, R. Palit, and V. V. Parkar, Phys. Rev. C **83**, 064606 (2011).

[22] P. K. Rath, S. Santra, N. L. Singh, K. Mahata, R. Palit, B. K. Nayak, K. Ramachandran, V. V. Parkar, R. Tripathi, and S. K. Pandit, Nucl. Phys. A **874**, 14 (2012).

[23] P. K. Rath, S. Santra, N. L. Singh, B. K. Nayak, K. Mahata, R. Palit, K. Ramachandran, S. K. Pandit, A. Parihari, A. Pal, et al., Phys. Rev. C **88**, 044617 (2013).

[24] A.Kundu, S. Santra, A. Pal, D. Chattopadhyay, B. K. Nayak, A. Saxena, and S. Kailas, Phys. Rev. C **94**, 014603 (2016).

[25] F. Plasil, R. L. Ferguson, R. L. Hahn, F. E. Obenshain, F. Pleasonton, and G. R. Young, Phys. Rev. Lett. **45**, 333 (1980).

[26] R. Kossakowski, J. Jastrzbski, P. Rymuza, W. Skulski, A. Gizon, S. Andr, J. Genevey, J. Gizon, and V. Barci, Phys. Rev. C **32**, 1612 (1985).

[27] V. V. Parkar, S. K. Sharma, R. Palit, S. Upadhyaya, A. Shrivastava, S. K. Pandit, K. Mahata, V. Jha, S. Santra, K. Ramachandran, et al., Phys. Rev. C **97**, 014607 (2018).

[28] M. Dasgupta, P. R. S. Gomes, D. J. Hinde, S. B. Moraes, R. M. Anjos, A. C. Berriman, R. D. Butt, N. Carlin, J. Lubian, C. R. Morton, et al., Phys. Rev. C **70**, 024606 (2004).

[29] R.Raabe, C.Angulo, J.L.Charvet, C.Jouanne, L.Nalpas, P.Figuera, D.Pierroutsakou, M.Romoli, and J.L.Sida, Phys. Rev. C **74**, 044606 (2006).

[30] K. Hirose, K. Nishio, S. Tanaka, R. Leguillon, H. Makii, I. Nishinaka, R. Orlandi, K. Tsukada, J. Smallcombe, M. J. Vermeulen, et al., Phys. Rev. Lett. **119**, 222501 (2017).

[31] J. E. Escher, J. T. Burke, F. S. Dietrich, N. D. Scielzo, I. J. Thompson, and W. Younes, Rev. Mod. Phys. **84**, 353 (2012).

[32] R.Lguillon, K.Nishio, K.Hirose, H.Maki, I.Nishinaka, R.Orlandia, K.Tsukada, J.Smallcombe, S.Chiba, Y.Aritomod, et al., Phys. Lett. B **761**, 125 (2016).

[33] B. K. Nayak, A. Saxena, D. C. Biswas, E. T. Mirgule, B. V. John, S. Santra, R. P. Vind, R. K. Choudhury, and S. Ganesan, Phys. Rev. C **78**, 061602(R) (2008).

[34] J. Lestone, J. Leigh, J. Newton, and J. Wei, Nucl. Phys. A **509**, 178 (1990).

[35] S. Kailas, D. M. Nadkarni, A. Chatterjee, A. Saxena, S. S. Kapoor, D. Chattopadhyay, R. Vandenbosch, J. P. Lestone, J. F. Liang, D. J. Prindle, et al., Phys. Rev. C **59**, 2580 (1999).

[36] N. Majumdar, P. Bhattacharya, D. C. Biswas, R. K. Choudhury, D. M. Nadkarni, and A. Saxena, Phys. Rev. C **51**, 3109 (1995).

[37] D. J. Hinde, M. Dasgupta, J. R. Leigh, J. P. Lestone, J. C. Mein, C. R. Morton, J. O. Newton, and H. Timmers, Phys. Rev. Lett. **74**, 1295 (1995).

[38] E. Konecny, H. Specht, and J. Weber, Phys. Lett. B **45**, 329 (1973).

[39] K.Nishio, H.Ikezoe, Y.Nagame, S.Mitsuoka, I.Nishinaka, L.Duan, K.Satou, S.Goto, M.Asai, H.Haba, et al., Phys. Rev. C **67**, 014604 (2003).

[40] E. K. Hulet, R. W. Lougheed, J. H. Landrum, J. F. Wild, D. C. Hoffman, J. Weber, and J. B. Wilhelmy, Phys. Rev. C **21**, 966 (1980).

[41] H. C. Britt and J. D. Cramer, Phys. Rev. C. **2**, 1758 (1970).

[42] J. D. Cramer and H. C. Britt, Phys. Rev. C. **2**, 2350 (1970).

[43] C. Plettner, H. Ai, C. W. Beausang, L. A. Bernstein, L. Ahle, H. Amro, M. Babilon, J. T. Burke, J. A. Caggiano, R. F. Casten, et al., Phys. Rev. C **71**, 051602(R) (2005).

[44] J. T. Burke, L. A. Bernstein, J. Escher, L. Ahle, J. A. Church, F. S. Dietrich, K. J. Moody, E. B. Norman, L. Phair, P. Fallon, et al., Phys. Rev. C **73**, 054604 (2006).

[45] B. F. Lyles, L. A. Bernstein, J. T. Burke, F. S. Dietrich, J. Escher, I. Thompson, D. L. Bleuel, R. M. Clark, P. Fallon, J. Gibelin, et al., Phys. Rev. C **76**, 014606 (2007).

[46] S. R. Lesher, J. T. Burke, L. A. Bernstein, H. Ai, C. W. Beausang, D. L. Bleuel, R. M. Clark, F. S. Dietrich, J. E. Escher, P. Fallon, et al., Phys. Rev. C **79**, 044609 (2009).

[47] B. L. Goldblum, S. R. Stroberg, J. M. Allmond, C. Angell, L. A. Bernstein, D. L. Bleuel, J. T. Burke, J. Gibelin, L. Phair, N. D. Scielzo, et al., Phys. Rev. C **80**, 044610 (2009).

[48] R. O. Hughes, C. W. Beausang, T. J. Ross, J. T. Burke, N. D. Scielzo, M. S. Basunia, C. M. Campbell, R. J. Casperson, H. L. Crawford, J. E. Escher, et al., Phys. Rev. C **85**, 024613 (2012).

[49] A. Czeszumska, C. T. Angell, J. T. Burke, N. D. Scielzo, E. B. Norman, R. A. E. Austin, G. Boutoux, R. J. Casperson, P. Chodash, R. O. Hughes, et al., Phys. Rev. C **87**, 034613 (2013).

[50] V. V. Desai, B. K. Nayak, A. Saxena, D. C. Biswas, E. T. Mirgule, B. John, S. Santra, Y. K. Gupta, L. S. Danu, G. K. Prajapati, et al., Phys. Rev. C **87**, 034604 (2013).

[51] A.Mukherjee, S.Roy, M.K.Pradhan, M.S.Sarkar, P.Basu, B.Dasmahapatra, T.Bhattacharya, S.Bhattacharya, S.K.Basu, A.Chatterjee, et al., Phys.Lett. B **636**, 91 (2006).

[52] G. Charpak, R. Bouclier, T. Bressani, J. Favier, and C. Zupancic, Nucl. Instrum. Methods Phys. Res. **62**, 262 (1968).

[53] A. Breskin, Nucl. Instrum. Methods Phys. Res. **196**, 11 (1982).

[54] A. Breskin, R. Chechik, Z. Fraenkel, P. Jacobs, I. Tserruya, and N. Zwang, Nucl. Instrum. Methods Phys. Res. A **221**, 363 (1984).

[55] H. Freiesleben, f. G. T. Rizzo, and Z. R. Huizenga, Phys. Rev. C **12**, 42 (1975).

[56] H. ZHANG, J. XU, Z. LIU, J. LU, K. XU, and M. RUAN, Phys. Letters B **218**, 133 (1989).

[57] P. Dyer, R. J. Puigh, R. Vandenbosch, T. D. Thomas, M. S. Zisman, and L. Nunnelley, Nucl. Phys. A **322**, 205 (1979).

[58] K. L. Wolf, R. Vandenbosch, and W. D. Loveland, Phys. Rev. **170**, 1059 (1968).

[59] V. E. Viola, Phys. Rev. C **31**, 1550 (1985).

[60] J. Fernandez-Niello, C. H. Dasso, and S. Landowne, Comp. Phys. Commun. **54**, 409 (1989).

[61] B. K. Nayak, R. G. Thomas, R. K. Choudhury, A. Saxena, P. K. Sahu, S. S. Kapoor, R. Varma, and D. Umakanth, Phys. Rev. C **62**, 031601(R) (2000).

[62] A. J. Sierk, Phys. Rev. C **33**, 2039 (1986).

[63] *NRV*, http://nrv.jinr.ru/nrv/webnrv/fission/, accessed: 02.11.2016.

[64] D. Vorkapic and B. Ivanisevic, Phys. Rev. C **52**, 1980 (1995).

[65] J. P. Lestone, A. A. Sonzogni, M. P. Kelly, and R. Vandenbosch, Phys. Rev. C **56**, R2907 (1997).

[66] R. G. Thomas, B. K. Nayak, A. Saxena, D. C. Biswas, L. M. Pant, and R. K. Choudhury, Phys. Rev. C **65**, 057601 (2002).

[67] A. N. Behkami, Nucl. Data. Tables **10**, 1 (1971).

[68] M. Caamao, O. Delaune, F. Farget, X. Derkx, K.-H. Schmidt, L. Audouin, C.-O. Bacri, G. Barreau, J. Benlliure, E. Casarejos, et al., Phys. Rev. C **88**, 024605 (2013).

[69] C. Rodrguez-Tajes, F. Farget, X. Derkx, M. Caamao, O. Delaune, K.-H. Schmidt, E. Clment, A. Dijon, A. Heinz, T. Roger, et al., Phys. Rev. C **89**, 024614 (2014).

[70] D. Ramos, M. Caamao, F. Farget, C. Rodrguez-Tajes, L. Audouin, J. Benlliure, E. Casarejos, E. Clement, D. Cortina, O. Delaune, et al., Phys. Rev. C **97**, 054612 (2018).

[71] A. Jhingan, P. Sugathan, K. S. Golda, R. P. Singh, T. Varughese, H. Singh, B. R. Behera, and S. K. Mandal, Rev. Sci. Instrum. **80**, 123502 (2009).

[72] G. Knyazheva, S. Khlebnikov, E. Kozulin, T. Kuzmina, V. Lyapin, M. Mutterer, J. Perkowski, and W. Trzaska, Nuclear Instruments and Methods in Physics Research B **248**, 7 (2006).

[73] A. Jhingan, P. Sugathan, G. Kaur, K. Kapoor, N. Saneesh, T. Banerjee, H. Singh, A. Kumar, B. Behera, and B. Nayak, Nuclear Instruments and Methods in Physics Research A **786**, 51 (2015).

[74] T.Ohtsuki, Y.Nagame, K.Tsukada, N.Shinohara, S.Baba, K.Hashimoto, I.Nishinaka, K.Sueki, Y.Hatsukawa, K.Hata, et al., Phys. Rev. C **44**, 1405 (1991).

[75] R. L. Ferguson, F. Plasil, F. Pleasonton, S. C. Burnett, and H. W. Schmitt, Phys. Rev. C **7**, 2510 (1973).

[76] R. Choudhury, A. Saxena, V. Ramamurthy, D. Nadkarni, and S. Kapoor, Nucl. Phys. A **463**, 597 (1987).

[77] L. Colby, Jr., M. Shoaf, and J. Cobble, Phys. Rev. **121**, 1415 (1961).

[78] I. Winkelmann and D. C. Aumann, Phys. Rev. C **30**, 934 (1984).

[79] B. Jurado and K. H. Schmidt, http://www.khs-erzhausen.de/GEF-2016-1-2.html Computer code GEF, Version 1.2 (2016).

[80] C. Schmitt, K.-H. Schmidt, and B. Jurado, arXiv: p. 1802.04267 (2018).

[81] T. von Egidy and D. Bucurescu, Phys. Rev. C **80**, 054310 (2009).

[82] J. M. Alexander and G. N. Simonoee, Phys. Rev. **162**, 952 (1967).

[83] R. Bimbot, D. Gardes, and M. Rivet, Nucl. Phys. A **189**, 193 (1972).

[84] S. Mukherjee, A. Sharma, S. Sodaye, B. Tomar, A. Goswami, and S. Manohar, Eur. Phys. J. A **12**, 199 (2001).

[85] S.K.Pandit, A.Shrivastava, K.Mahata, V.V.Parkar, R.Palit, N.Keeley, P.C.Rout, A.Kumar, K.Ramachandran, S.Bhattacharyya, et al., Phys. Rev. C **96**, 044616 (2017).

[86] A.Shrivastava, A.Navin, A.Diaz-Torres, V.Nanal, K.Ramachandran, M.Rejmund, S.Bhattacharyya, A.Chatterjee, S.Kailas, A.Lemasson, et al., Phys. Lett. B **718**, 931 (2013).

[87] S. Santra, S. Kailas, V. V. Parkar, K. Ramachandran, V. Jha, A. Chatterjee, P. K. Rath, and A. Parihari, Phys. Rev. C **85**, 014612 (2012).

[88] V. V. Parkar, S. K. Pandit, A. Shrivastava, R. Palit, K. Mahata, V. Jha, K. Ramachandran, S. Gupta, S. Santra, , et al., Phys. Rev. C **98**, 014601 (2018).

[89] R. Broda, M. Ishihara, B. Herskind, H. Oeschler, and S. Ogaza, Nucl. Phys. A **248**, 356 (1975).

[90] A. Pakou, K. Rusek, N. Alamanos, X. Aslanoglou, M. Kokkoris, A. Lagoyannis, T. J. Mertzimekis, A. Musumarra, N. G. Nicolis, D. Pierroutsakou, et al., Eur. Phys. J A **39**, 187 (2009).

[91] M. Sinha, H. Majumdar, P. Basu, S. Roy, R. Bhattacharya, M. Biswas, M. K. Pradhan, R. Palit, I. Mazumdar, and S. Kailas, Eur. Phys. J A **44**, 403 (2010).

[92] A. D. Pietro, P. Figuera, E. Strano, M. Fisichella, O. Goryunov, M. Lattuada, C. Maiolino, C. Marchetta, M. Milin, A. Musumarra, et al., Phys. Rev. C **87**, 064614 (2013).

[93] A. Pal, S. Santra, D. Chattopadhyay, A. Kundu, A. Jhingan, P. Sugathan, N. Saneesh, M. Kumar, N.L.Singh, A. Yadav, et al., Phys. Rev. C (R) **98**, 031601 (2018).

[94] R. G. Thomas, D. J. Hinde, D. Duniec, F. Zenke, M. Dasgupta, M. L. Brown, M. Evers, L. R. Gasques, M. D. Rodriguez, and A. Diaz-Torres, Phys. Rev. C **77**, 034610 (2008).

[95] T. K. Ghosh, K. Banerjee, C. Bhattacharya, S. Bhattacharya, S. Kundu, P. Mali, J. K. Meena, G. Mukherjee, S. Mukhopadhyay, T. K. Rana, et al., Phys. Rev. C **79**, 054607 (2009).

[96] A. Chaudhuri, T. K. Ghosh, K. Banerjee, S. Bhattacharya, J. Sadhukhan, C. Bhattacharya, S. Kundu, J. K. Meena, G. Mukherjee, R. Pandey, et al., Phys. Rev. C **91**, 044620 (2015).

[97] B. B. Back, A. C. Shotter, T. J. M. Symons, A. Bice, C. K. Gelbke, T. C. Awes, and D. K. Scott, Phys. Rev. C **23**, 1105 (1981).

[98] J. J. Ressler, J. T. Burke, J. E. Escher, C. T. Angell, M. S. Basunia, C. W. Beausang, L. A. Bernstein, D. L. Bleuel, R. J. Casperson, B. L. Goldblum, et al., Phys. Rev. C. **83**, 054610 (2011).

[99] S. Goriely and M. Arnould, Astron. Astrophys. **379**, 1113 (2001).

[100] M. Petit, M. Aiche, G. Barreau, S. Boyer, N. Carjan, S. Czajkowski, D. Dassie, C. Grosjean, A. Guiral, B. Haas, et al., Nucl. Phys. A **735**, 345 (2004).

[101] S. Boyer, D. Dassie, J. N. Wilson, M. Ache, G. Barreau, S. Czajkowski, C. Grosjean, A. Guiral, B. Haas, B. Osmanov, et al., Nucl. Phys. A **775**, 175 (2006).

[102] G. Alibarti, G. Palmiotti, M. Salvatores, T. Kim, T. Taiwo, M. Anitescu, I. Kodeli, E. Sartori, J. Bosq, and J. Tommasi, Ann. Nucl. Energy. **33**, 700 (2006).

[103] G. Wasserburg, M. Busso, R. Gallino, and K. Nollett, Nucl. Phys. A **777**, 5 (2006).

[104] V. F. Weisskopf and D. H. Ewing, Phys. Rev. **57**, 472 (1940).

[105] M. Cance and G. Grenier, Nucl. Sci. and Engg. **68**, 197 (1978).

[106] M. Cance, G. Grenier, D. Gimat, and D. Parisot, http://www.nndc.bnl.gov/EXFOR/20779.002 (EXFOR database version of October 13, 2014).

[107] M. Herman, R. Capote, B. Carlson, P. Oblozinsky, M. Sin, A. Trkov, H. Wienke, and V. Zerkin, Nucl. Data Sheets **108**, 2655 (2007).

[108] J. Ziegler, http://www.srim.org/, Computer code SRIM (2013).

[109] R. Capote, M. Herman, P. Oblozinsky, P. Young, S. Goriely, T. Belgya, A. Ignatyuk, A. Koning, S. Hilaire, V. Plujko, et al., Nucl. Data Sheets **110**, 3107 (2009).